Gold Nanorod-Based Dimers with accessible Hotspots for Surface-Enhanced Raman Spectroscopy

Francis Rameshchandra Schuknecht

München, 2024

Gold Nanorod-Based Dimers with accessible Hotspots for Surface-Enhanced Raman Spectroscopy

Dissertation

an der Fakultät für Physik der

Ludwig-Maximilians-Universität München

vorgelegt von

Francis Rameshchandra Schuknecht

aus Rockville, Maryland, USA

München, den 11. September 2024

Erstgutachter:	PD Dr. Theobald Lohmüller
Zweitgutachter:	Prof. Dr. Alexander Urban
Tag der mündlichen Prüfung:	29.10.2024

Kurzfassung

Oberflächenverstärkte Raman-Streuung (SERS) ist ein Schlüssel zu markierungsfreier biomedizinischer Diagnostik. Insbesondere bezüglich der Identifikation von einzelnen Proteinen und anderer Biomoleküle aus einer Lösung. SERS-Detektion stellt allerdings aufgrund der kleinen Ramanstreuquerschnitte von molekularen Gruppen eine Herausforderung dar. Sie erfordern signifikante Raman Verstärkungsfaktoren. Diese können durch eine erhöhte elektromagnetische Feldverstärkung in Lücken zwischen plasmonisch gekoppelten metallischen Nanopartikeln erreicht werden. Idealerweise sind solche plasmonischen Antennen schnell mit offen zugänglichen Hotspots erzeugbar, sowie frei als so genannte Nanoagenten einsetzbar. In dieser Dissertation werden zwei verschiedene Gold Nanostäbchen (GNR) basierte Dimere, für SERS von Analyten aus wässeriger Lösung, vorgestellt.

Der erste Dimer Typ basiert direkt auf GNRs, die aufgrund einfacher Synthetisierbarkeit, anpassbarer Resonanz und signifikanter elektromagnetischer Feldverstärkung an ihren abgerundeten Enden ausgewählt wurden. Nanostäbchen Dimere wurden mittels eines DNA-Origami Gerüsts in Balkenform in einer Spitze an Spitze Manier assembliert. Diese Antennen besaßen Lücken mit ~8 nm Spannweite, mit Analyt-spezifischen Bindungsstellen an den plasmonischen Hotspots und waren auf Resonanz im Roten bis Nahinfraroten (NIR) ausgelegt. Sie ermöglichten Subsekunden SERS-Detektion von einzelnen aus einer Lösung gebundenen Streptavidin und Thrombin Molekülen, mittels eines 671 nm Lasers. Diese Ergebnisse werden durch Rechnungen, die ausreichende E-Feld Verstärkung indizieren und Experimente zu Detektionsspezifizität, gestützt. Abschließend wurden Nanostäbchen basierte Strategien für stärkeres SERS aus größeren Lücken untersucht. Hier wirken sowohl stumpfere GNR spitzen, Silbernanostäbchen, als auch GNR Tetramere vielversprechend, während GNR Trimere und Hotspots zwischen schärferen Spitzen dies nicht tun.

Der zweite Dimer Typ besteht aus GNRs die mittels eines fokussierten 1064 nm Lasers in zwei Sphären gespalten sind, welche dann durch den Laser paarweise auf Glass Substrate optisch gedruckt werden. Dieser neuere Zufallsfund wurde auf plasmonische Hotspots untersucht. Lücken zwischen den Nanosphären konnten mittels Transmissionselektronenmikroskopie bestätigt werden und wurden spektroskopisch für ~0.8 nm groß befunden. Sie ermöglichten signifikantes 4-Nitrothiophenol Resonanz-Raman Signal am NIR und waren für das Analyt, welches nach der Dimer Generation hinzugegeben wurde, frei zugänglich. Des Weiteren wurden mittels numerischer Modellierung optische Kraft als Einfluss auf die Angström Lücken analysiert. Hier wurde ein Zusammenspiel zwischen zwei Laser getriebenen Kraftkomponenten identifiziert. Die erste ist klassische Dipol-Dipol Attraktion. Die zweite ist separativ und stammt von einer Einzel-Dipol Komponente durch Intradimer Elektron Tunneln.

Hiermit präsentiert diese Arbeit zwei unterschiedliche Gold Nanostäbchen basierte Pfade, für frei zugängliche SERS Hotspots die im Bio-Optischen Fenster funktional sind. Sie befasst sich auch mit den Mechanismen hinter und potenziellen Verbesserungen von diesen Nanoagenten und verkürzt somit den Weg zu biodiagnostischen und anderen Detektionsapplikation mittels SERS.

Abstract

Surface-enhanced Raman scattering (SERS) spectroscopy is a key to label-free biomedical diagnostics. Particularly regarding the identification of single proteins and other biomolecules from liquid samples. SERS detection does however pose a challenge, due to the small Raman scattering cross sections of molecular groups involved. These necessitate significant Raman enhancement factors. Such amplification can be achieved by raised electromagnetic field enhancement in gaps between plasmonically coupled metallic nanoparticles. Ideally, such plasmonic multimer antennas are rapidly creatable with openly accessible hotspots, as well as freely deployable as so called nanoagents. In this PhD thesis, two different gold nanorod (GNR)-based dimer concepts are presented, for detecting analyte from aqueous solution with SERS.

The first dimer type involves GNRs directly, selected due to their ease of synthesis with a tuneable resonance and significant electromagnetic field enhancement at rounded ends. Nanorod dimers were assembled in a tip-to-tip manner using a DNA origami beam-based scaffold design. The antennas featured ~8 nm gaps, with analyte specific binding sites at the plasmonic hotspots, and were tuned for red to near infrared (NIR) resonance. These enabled subsecond SERS detection of single streptavidin and thrombin molecules captured from solution, using a 671 nm laser. The results are supported by calculations indicating sufficient E-field enhancement and experiments on detection specificity. Finally, nanorod-based strategies for stronger SERS from larger gaps were examined. Here, blunter GNR tips, silver nanorods, as well as GNR tetramers appear promising, whilst GNR trimers and hotspots between sharper tips do not.

The second dimer type consists of GNRs split into two spheres with a focused 1064 nm laser, which are then optically printed onto glass substrates pairwise by the laser. This recent chance discovery was investigated for plasmonic hotspots. Gaps between the nanospheres could be confirmed using transmission electron microscopy, and were found to be ~0.8 nm in size spectroscopically. They enabled significant 4-nitrothiophenol resonance Raman signal at the NIR and were also freely accessible for the analyte molecules added post dimer generation. Further, numerical modelling was used for analyzing optical force as an influence on the angstrom gaps. Here an interplay of two laser driven force components was identified. The first is classical dipole-dipole attraction. The second is separative, and stems from a single-dipole component mediated by intradimer electron tunnelling.

Hereby, this work presents two distinct gold nanorod-based paths, to freely accessible SERS hotspots functional in the bio-optical window. It also delves into mechanisms behind and potential improvements of these nanoagents, thus shortening the way to bio-diagnostic and other sensing applications via SERS.

Publications and Conference Contributions

Scientific Publications of Results presented in this Work

- **Single-Step Plasmonic Dimer Printing by Gold Nanorod Splitting with Light**

  F. Schuknecht[#], C.M. Maier[#], P. Vosshage, V.A. Hintermayr, M. Döblinger, T. Lohmüller*; Nano Letters, 23, 11, 4762–4769 (2023); DOI: 10.1021/acs.nanolett.2c04954

- **Accessible hotspots for single-protein SERS in DNA-origami assembled gold nanorod dimers with tip-to-tip alignment**

  F. Schuknecht[#], K. Kolataj[#], M. Steinberger, T. Liedl, T. Lohmüller*; Nature Communications, 14, 7192 (2023); DOI: 10.1038/s41467-023-42943-7

Additional Publications

- **Label-free Time-resolved Monitoring of Photolipid Bilayer Isomerization by Plasmonic Sensing**

  J. Zhang, F. Schuknecht, L. Habermann, A. Pattis, J. Heine, S. Pritzl, T. Lohmüller*; Advanced Optical Materials, 12 (2024); DOI: 10.1002/adom.202302266

- **Plasmonic Nanoagents in Biophysics and Biomedicine**

  M.A. Huergo, F. Schuknecht, J. Zhang, T. Lohmüller*; Advanced Optical Materials, 10 (2022); DOI: 10.1002/adom.202200572

- **Monitoring the surface quality of silver plasmon waveguides with nonlinear photoemission electron microscopy and in-situ ion sputtering**

  K. Pearce*, F. Schuknecht, C. Späth, B. Duschner, F. Richter, U. Kleineberg; Ultramicroscopy, 183, 55-60 (2017); DOI: 10.1016/j.ultramic.2017.05.008

[#]**:** Listed as equal Contributors; ***:** Corresponding Author

Conference and Workshop Contributions

- PhOG Chair Retreat (Talk):

  Plasmonic Nanoparticle Dimers for Single Protein SERS

  Fall-Lenggries, July 2022

- SFB1032 Workshop 2021 (Talk):

  Nanoagents for Single Protein Spectroscopy and Photoswitching with Red Light

  F. Schuknecht, S. Pritzl, T. Lohmüller; Herrsching am Ammersee, October 2021

- CeNS "Venice 2021 Workshop Replacement" (Poster):

  Detecting Single Protein Binding via SERS from DNA Origami Bi-Nanorods

  F. Schuknecht, K. Kolataj, M. Steinberger, T. Liedl, T. Lohmüller;

  Munich, September 2021

- SFB1032 Workshop 2020 (Talk):

  Single Molecule SERS with Plasmonice DNA Origami Nanoantennas

  F. Schuknecht, K. Kolataj, T. Liedl, T. Lohmüller; Virtual, November 2020

- PhOG Chair Retreat (Talk):

  Bending and Plasmon Dephasing of Gold Nanorods

  Haigerloch, March 2019

- PSRC (LMU) 2018 (Talk):

  Plasmonic Bending and Melting of Gold Nanorods

  F. Schuknecht, C. Maier, T. Lohmüller, J. Feldmann; Munich, June 2018

- DPG-Frühjahrstagungen 2018 (Talk):

  Nano-forging of Gold Rods with Light

  F. Schuknecht, C. Maier, A. Babynina, T. Lohmüller; Berlin, March 2018

Content

1 Introduction to Single Protein Raman Detection

The discovery of Raman scattering by Chandrasekhara V. Raman et al. in 1928 [1, 2], has led to a Nobel prize in 1930. Further, Raman spectroscopy, based on characteristic vibrational energies of chemical bonds, has become one of the principal methods for identifying analyte. As such, it presents an answer to a key goal in biomedical diagnostics: the detection of label-free single proteins from aqueous solution. This is also the main challenge of this work.

For (single) molecules, Raman spectroscopy features a downside, in that its sensitivity is limited by the small scattering cross sections of ~10^{-30} cm^2/sr [3-5] involved. Here, stimulated Raman spectroscopy (SRS) [6, 7], coherent anti-Stokes Raman spectroscopy (CARS) [8, 9] and coherent Stokes Raman scattering (CSRS) [8] have been employed to raise Raman signal by orders of magnitude over spontaneous emission. This has also allowed for spatially resolving protein concentration with SRS [10], chemical and biological systems with CARS [11], as well as biological samples with CSRS [12]. However, these methods require costly pulsed laser setups. Further, in the context of single-molecule detection, and similarly to conventional Raman spectroscopy, they feature significant background signal due to limited optical resolution.

These constraints can be alleviated through surface-enhanced Raman scattering (SERS). Observations from the effect, in the vicinity of rough metal surfaces, were first reported on by Fleischmann et al., in 1974 [13]. The results were attributed both to electromagnetic surface enhancement by Jeanmaire & Van Duyne in 1977 [14], as well as a chemical enhancement [15, 16]. In later work, the electromagnetic component was found to dominate [3]. It stems from collective oscillations of metal surface electrons as surface plasmons, excitable by light. This has in fact been used for single protein SERS from electrochemically deposited gold films [17], albeit determined via statistical analysis. Additionally, it has enabled time resolved SERS from metallic nanopores with optically trapped nanoparticles [18]. Further, tip-enhanced Raman spectroscopy (TERS), has been developed towards spatially resolving protein structures, by scanning them with a sharp metallic probe [19, 20]. However, for Raman detection via bottom-up assembled and freely deployable sensors – a desirable modus operandi in applications – alternatives must be explored. Here metallic nanoparticles and their strongly excitable (localized) surface plasmon resonances can be employed as plasmonic nanoagents [21].

The first documented use of such nanoparticles was by the ancient Romans for coloring glass, a famous example being the Lycurgus-Cup [22]. This was followed by centuries of gold and silver powders used for staining church windows and other coloring applications. It took until 1857 for Michael Faraday to link these optical effects to the minuscule sizes of the particles [23]. Later, in 1905, Richard Zsigmondy reported on the mechanism behind the reddish color of colloidal gold

nanoparticles [24], earning him a Nobel prize for chemistry in 1925. Gustav Mie introduced a conclusive theory for metallic nanospheres in 1908 [25], which was expanded to spheroidal particles by Richard Gans by 1912 [26]. These somewhat conceptual ellipsoids are spectroscopically similar to gold nanorods (GNRs) [27], the particles of choice in this thesis. Today, such nanorods can be synthesized readily [28-31], by growing seed crystals [32] into elongated particles in an $HAuCl_4$ (chloroauric acid) solution. This tuning of particle geometry is mediated with surfactants, allowing for specific crystal facet growth directions [33]. GNRs exceed gold nanospheres in both optical cross sections [34], as well as E-field- and radiation- [35] enhancement at their tips, which is beneficial for SERS.

Metallic nanoparticles can also be coupled plasmonically via proximity. This leads to E-field enhancement hotspots in the resulting antenna gaps, which are thus useful for increasing SERS. Here DNA origami [36, 37] has emerged as a highly effective tool for arranging plasmonic multimers. It is based on self-assembling DNA employed as scaffolding for both metallic nanoparticles as well as analyte. Most prominently, to generate freely deployable gold nanosphere (GNS) dimers. However, strong field enhancement for single-molecule (SM) SERS has required reduced ~1-2 nm nanosphere gap spans for both dye molecules [38, 39] and proteins [40]. Such hotspots limit the size of potential SERS analyte, and are less accessible, particularly when obstructed by DNA. Other DNA origami-based schemes, such as bi-gold nanostars [41] and tip-to-tip aligned gold nanotriangles (bowties) [42], featured more open gaps, but no clear SERS measurement of diffusive analyte from solution. These aspects call for alternative sensing nanoagents, combining accessible hotspots with strong field enhancement and ease of assembly.

Such plasmonic antennas are the subject of this thesis. Physical principals behind Raman scattering and its enhancement, as well as particle plasmons are described in **Chapter 2**. This is done with a focus towards E-field enhancement of plasmonic dimers for SERS, as well as optical forces and heating experienced by them. Methods used to study the nanoagents experimentally and theoretically are described in **Chapter 3**.

For the first results **Chapter 4** of this work DNA origami was used for spacing two gold nanorods in a tip-to-tip alignment along their long axes. It begins with the GNR dimer design for significant E-field enhancement from accessible hotspots, with analyte specific binding sites. This is followed by characterizing the antennas regarding SERS. Next, GNR dimers allowed for capturing and detecting of single thrombin and streptavidin molecules, from and in solution. These results are supported both by calculations, as well as further experiments on protein detection specificity. Finally, alternative nanorod-based multimer designs are discussed towards generating even more effective SERS hotspots.

Chapter 5 of this thesis deals with a new type of gold nanosphere dimer for Raman enhancement, which does not require scaffolding. Instead, the dimers are printed from optically split GNRs in a single step with a focused laser. The chapter begins with a description of the antenna assembly. It continues with experiments and calculations which show that the GNS dimers feature ~sub-nm gaps. These hotspots are then employed for measuring SERS of 4-nitrothiophenol (NTP), added post dimer synthesis. The chapter is concluded with the analysis of an optical force-based model contributing to the dimer hotspot span, and how it might be tuned.

Finally, in **Chapter 6**, I summarize the findings and conclude on a bright future for both GNR-based types of dimers as plasmonic nanoagents.

2 Fundamentals of Plasmonic Dimers for SERS

In a dielectric environment, metallic nanoparticles feature a plasmonic resonance via the particle plasmon [43], also known as the localized surface plasmon (LSP) [44]. At their peaks, these oscillations of surface conduction electrons, can cause a significant increase in both real and imaginary parts of the particle's polarizability. This is possible to the point that both scattering as well as absorption cross sections exceed those of geometry [34]. In particular at resonance, increased extinction cross sections of plasmonic nanoparticles, coupled with the small surface curvatures involved, generate strong enhancement factors (EF) of incident light's electric fields, as well as radiation enhancement factors in their vicinities [5]. This is one of the main components from which they draw their properties as Raman sensing agents. Here, SERS scales in the following manner [5, 45]:

$$Raman\ Signal \sim EF_{excitation}^{2} \cdot EF_{Raman}^{2} \sim EF^{4} \qquad \text{Eq. (2.1)}$$

As further simplified, and often used in approximations, SERS scales with the fourth power of E-field enhancement. The following delves into fundamentals behind Raman scattering and its enhancement via plasmonic dimers.

2.1 Surface-Enhanced Raman Scattering

Molecular groups, and other defined atomic arrangements such as lattices, feature distinct vibrations, partially susceptible to light in a process known as Raman scattering. This inelastic process is explained in the first section of this subchapter. The loss of energy to (or gain by) such oscillations can then be resolved spectroscopically, to identify the presence and type of analyte molecules. Such detection is the main motivation of this thesis. Here, the small nature of Raman cross sections [3-5], necessitates their enhancement, the subject of the second section of this subchapter. Whilst two main components of SERS exist, namely chemical enhancement, and electromagnetic enhancement, the dominance of the second component [3] warrants delving into it in greater detail.

2.1.1 Raman Scattering and SERS

Raman scattering occurs in conjunction with oscillations of the polarizability of atomic arrangements [5]. As such, it relies on changes in overall lengths involved. This can be explained by placing it in contrast with IR-spectroscopy [46], which relies on oscillations of actual dipolar moments [47]. An illustration of the comparison is depicted in **Figure 2.1.1 A**. Raman signal can be gained by a monochromatic light source, whilst IR-spectroscopy requires a broadband source covering a range of modes, which can absorb photon energy. In both cases, signal can be resolved spectroscopically.

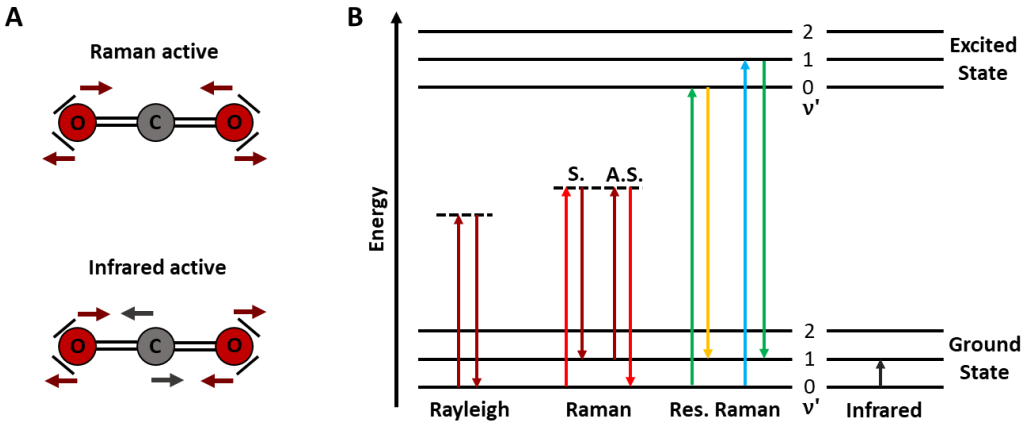

Figure 2.1.1: Illustration of Raman Scattering. A Sketch illustrating Raman, and IR active vibrations in the case of CO_2. Here, the Raman active mode involves oscillations in the molecule's length. For the IR mode, the higher electronegativity of oxygen compared carbon leads to effective charge asymmetry, and a dipole moment in the case of antisymmetric displacements. **B** Jablonski diagram of Rayleigh, Stokes/anti-Stokes (S./A.S.) Raman and resonance (Stokes) Raman scattering, as well as IR absorption. Here, dashed lines represent virtual states and ν' denotes vibrational levels.

In principle, both vibrational as well as rotational modes of the molecule can contribute to Raman signal. In practice, however, rotational modes are more relevant for lighter molecules, such as gasses [5], and thus not examined in this work. Therefore, Raman active oscillations

feature two main peaks: one Stokes, from an $\hbar\omega_v$ loss of energy to a vibrational state (with frequency ω_v), and one anti-Stokes from an $\hbar\omega_v$ energy gain from the mode, for the incident light (usually stemming from a laser) with frequency ω_L. The corresponding energy changes are illustrated in **Figure 2.1.1 B**. The resulting Raman signal photons, with a singular vibrational transition, have frequencies:

$$\omega_R = \omega_L \pm \omega_v. \tag{2.2}$$

Usually, the signal of interest stems from the lower energy Stokes component. The prerequisite for corresponding anti-Stokes scattering is vibrational occupation of the first level of the ground state. With a Boltzmann occupation distribution at temperature T, the corresponding probability is:

$$P_1 = e^{-\hbar\omega_v/k_BT}. \tag{2.3}$$

Here, occupation of higher vibrational states is significantly less probable, as vibrational energies exceed thermal energies. Consequently, probability for ground state occupation can be simplified to:

$$P_0 \simeq 1 - P_1 \simeq 1. \tag{2.4}$$

The ratio between the two states is therefore:

$$\frac{P_1}{P_0} \simeq exp\left(\frac{-\hbar\omega_v}{k_BT}\right). \tag{2.5}$$

With total power radiated by a dipole being proportional to ω^4, as is derivable from Maxwell's equations [48, 49], intensity ratios between anti-Stokes and Stokes scattering are [5]:

$$\frac{I_{AS}}{I_S} = \left(\frac{\omega_L+\omega_v}{\omega_L-\omega_v}\right)^4 exp\left(\frac{-\hbar\omega_v}{k_BT}\right). \tag{2.6}$$

Typically, vibrational energies are expressed in wavenumbers ν, where:

$$\nu = \frac{\omega_v}{2\pi c}. \tag{2.7}$$

The common unit of measure used is then: cm^{-1}.

To ensure that peaks are energetically sharp, and thus detectable, typically a laser with a high monochromaticity is used as an excitation source. For a laser with λ = 671 nm, a temperature of 293 K (room temperature), and ν = 1500 cm^{-1} (186 meV – a value in the typical range of those for carbon-based compounds examined in this thesis), the anti-Stokes probability becomes ~0.1%. Therefore, this work focuses on detecting Raman scattering stemming from a Stokes process.

A more detailed view of this scattering process for a specific vibrational mode involves its 3 × 3 Raman polarizability tensor $\hat{\alpha}_R(\omega_L, \omega_v)$. It can be used to describe a Raman induced dipole $\boldsymbol{p}_R(\omega_R)$ in a vacuum, oscillating with ω_R , via:

$$\boldsymbol{p}_R(\omega_R) = \hat{\alpha}_R(\omega_L, \omega_v)\boldsymbol{E}(\omega_L). \tag{2.8}$$

Here, $\boldsymbol{p}_R(t) = Re(\boldsymbol{p}_R(\omega_R)\exp(-i\omega_R t))$, and $\boldsymbol{E}(t) = Re(\boldsymbol{E}(\omega_L)\exp(-i\omega_L t))$ are time dependant. The Raman polarizability tensor is however not, and allows for a classical description of Raman scattering.

Within this work, SERS from aqueous molecules is discussed, leading to an important effect namely that of microscopic fields [5], related to their macroscopic counterparts via $\boldsymbol{E}_{Micro} = (L_M)^{1/4}\boldsymbol{E}_{Macro}$, with:

$$(L_M)^{1/4} = \frac{\varepsilon_M + 2}{3}. \tag{2.9}$$

In vacuum, this value is 1, which also closely describes conditions in air. For water the main medium of interest here, with a refractive index n_M of 1.33 and permittivity of 1.77, $(L_M)^{1/4}$ = 1.26 is still relatively close to 1. It does however modify the Raman polarizability tensor with:

$$\boldsymbol{p}_R(\omega_R) = (L_M)^{1/4}\hat{\alpha}_R(\omega_L, \omega_v)\boldsymbol{E}(\omega_L). \tag{2.10}$$

At the same time, the total power emitted by a dipole in a medium is proportional to n_M, and the dipole moment squared:

$$P_{rad} = \frac{\omega^4 n_M (L_M)^{1/2} |\boldsymbol{p}|^2}{12\pi\varepsilon_0 c^3}. \tag{2.11}$$

In water, this power is ~2.1 times larger than in vacuum/air, and could be increased with higher permittivity media. Whilst not major, this factor can be expected to benefit aqueous measurements in this thesis. On the other hand, longer wavelengths lessen Raman scattering.

Another aspect to be considered is the tensorial nature of $\hat{\alpha}_R$, incorporating the excitable orientation of an individual potential Raman oscillator. In principle, Raman scattering could be aided by orienting the tensor (by rotating its molecule) according to desired axes. However, here, molecules are studied where orientation is not rigidly fixed in space. For one, this might lower intensities of potentially specifically desired peaks. It does however also mean that all Raman modes can be enhanced electromagnetically, by increasing both P_{rad} of the molecular dipole as well as $\boldsymbol{E}(\omega_L)$ in a single spatial dimension. The enhancement aspect – essential to work presented here on SERS in proximity to metallic particle surfaces – will be discussed in the next section.

The second component of SERS, chemical enhancement, stems from broadening of excited states during resonance Raman (thus enhancing $\hat{\alpha}_R$), as postulated by Philpott and published in 1975 [15]. It would be limited to where analyte for resonance Raman is attached directly to the

plasmonic nanoantennas in this study. Additionally, more recent extensive analysis by Le Ru, Etchegoin et al., published in 2007 [3], calls this factors relevance into question. Further, the aforementioned enhancement requires resonance Raman conditions (**Figure 2.1.1 B**), where excitation reaches (virtual) states at or beyond molecular transition energies [50]. Whilst resonance Raman can feature greatly enhanced cross sections [5], by several orders of magnitude in the case of dyes [3] for example, it requires excitation wavelengths in specific ranges.

2.1.2 Electromagnetic Enhancement of Raman Scattering

Plasmonic nanoantennas are highly suited to enhancing Raman signal, both via amplifying the external excitation field, was well as increasing Raman radiation. The first component – the $EF^2_{excitation}$ factor in **Equation 2.1** – is most intuitive. This is underlined by the depictions of field enhancement in the following **Section 2.2.1**. As such, it is strongest in direct proximity to plasmonic particle-based antennas, as well as rough metallic surfaces, with the latter being the namesake of SERS.

The second component, based on the radiation enhancement factor, is somewhat less intuitive. Here dipoles radiation is modified with an increase in local density of states (LDOS). For one, as mentioned in the previous **Section 2.1.1**, this scales with refractive index. More importantly however, it also scales with field enhancement at the Raman scattering or (anti-)Stokes shifted wavelength. This is in accordance with the optical reciprocity theorem (ORT) [51]:

$$\boldsymbol{p}_1 \cdot \boldsymbol{E}_2 = \boldsymbol{p}_2 \cdot \boldsymbol{E}_1. \tag{2.12}$$

It states how a field $\boldsymbol{E}_2$ created at position a by dipole $\boldsymbol{p}_2$ at position b is related to the field $\boldsymbol{E}_1$ at b created by a dipole $\boldsymbol{p}_1$ at a. This allows for the derivation, that far-field emission of a dipole in a given direction is enhanced by the square of local E-field enhancement for plain wave excitation from this direction [5]. This EF^2_{Raman} constitutes the second factor in **Equation 2.1**, and is thus as directly calculatable as the first excitation enhancement term.

It is important to note that in principle, a plethora of different notations for and definitions of modified spontaneous Raman emission exist [5]. These include considerations for reabsorption of Raman photons by the optical system as well as directional emission. The first aspect is particularly relevant for plasmonic antennas. Here, single plasmon modes with the largest polarizability might dominate in terms of scattering to absorption ratios, as well as interaction cross sections. They also feature highest E-field enhancements, as discussed in the later **Section 2.2.2**. This leads directly to the aspect that previous discussions of Raman enhancement focused on parallel detection, where polarizability, laser polarization and E-field enhancement are aligned in one axis. For a back-scattering configuration, with unidirectional excitation and detection, this

is however a relatively exact approximation [5]. Effectively, it matches experimental conditions with SERS via longitudinal resonance of plasmonic dimers. It will therefore be used for comparative purposes in following chapters.

A final important aspect of electromagnetic enhancement is related to image dipole effects in proximity to metallic surfaces. When this proximity (usually less than 1 nm for the effect to become relevant) is generated via adsorption, it might be ascribed to chemical enhancement [5]. Here it acts both at the excitation, as well as the Raman wavelength, where it might introduce additional enhancement factors ~10. Additionally, image dipoles have been identified as contributors to background signal in Raman measurements, from broadening of corresponding SERS peaks by coupling to the electronic continuum of the metal [52]. Whilst the focus of this work lies on E-field enhancement factors towards SERS, image dipole effects can however still influence results.

2.2 Plasmonic Dimers

There are a number of ways in which plasmonic nanoparticles can be tuned to raise electric field strength, and thus Raman enhancement. For one, this includes less lossy metal parameters. Additionally, sharper tipped geometries will lead to concentrated E-field enhancement. Lastly, coupling two metallic nanoparticles with one another, will lead to higher field enhancement in the gap between them. Intriguingly, the gold nanorod dimer antennas at the focus of this thesis feature a combination of all three of these components. These factors are also partially exploited by optically splitting gold nanorods into nanosphere dimers, with (sub)nanometer plasmonic hotspots. Similarly, to other plasmonic particle-based nanoagents for sensing [21], optical forces and plasmonic heating can also come into play for such dimers. This subchapter serves to present the fundamentals behind these aspects.

2.2.1 Single Particle Plasmons

The idealized particle plasmon is a standing wave of electrons localized to the surface of a metallic nanoparticle. Understanding this light driven oscillation can begin with examining how matter responds to an electric field $\boldsymbol{E}(\omega)$, via a displacement field $\boldsymbol{D}(\omega)$. The two are linked both by the vacuum permittivity ε_0 and polarization $\boldsymbol{P}(\omega)$ [53], as well as by the frequency dependent dielectric function $\varepsilon(\omega)$ [54]:

$$\boldsymbol{D}(\omega) = \varepsilon_0 \boldsymbol{E}(\omega) + \boldsymbol{P}(\omega) = \varepsilon(\omega)\boldsymbol{E}(\omega). \tag{2.13}$$

The derivation of this permittivity in its most primitive form comes from the classical Drude model. In it, conduction band electrons are modelled as an ideal gas with a density of n, an effective mass m_{e*}, and a mean scattering rate or damping constant γ. This model is local, in that electrons are only influenced by fields applied to their direct location. The corresponding equation of motion is then equivalent to [53]:

$$m_{e*}\frac{\partial^2 \boldsymbol{x}}{\partial t^2} = -\gamma m_{e*}\frac{\partial \boldsymbol{x}}{\partial t} - eE(t). \tag{2.14}$$

At the same time, any electron displacement results in a polarization $\boldsymbol{P} = -en\boldsymbol{x}(\omega)$, from which the plasma frequency of the metal can be derived:

$$\omega_p = \sqrt{\frac{ne^2}{\varepsilon_0 m_{e*}}}. \tag{2.15}$$

For oscillations driven by an incident field $E(t) = E_0 e^{-i\omega t}$, the equation of motion can then be solved via:

$$\boldsymbol{x}(\omega) = \frac{eE(\omega)}{m_{e*}(\omega^2 + i\omega\gamma)}. \tag{2.16}$$

This grants access to the dielectric function:

$$\varepsilon(\omega) = \varepsilon_0 \left(1 - \frac{\omega_p^2}{\omega^2 + i\omega\gamma}\right). \tag{2.17}$$

A positive ionic background modifies **Equation 2.13** by a background polarization term where $P_\infty = \varepsilon_0(\varepsilon_\infty - 1)$, with ε_∞ as the background permittivity [53]. This leads to the dielectric function:

$$\varepsilon(\omega) = \varepsilon_\infty - \frac{\omega_p^2}{\omega^2 + i\omega\gamma}. \tag{2.18}$$

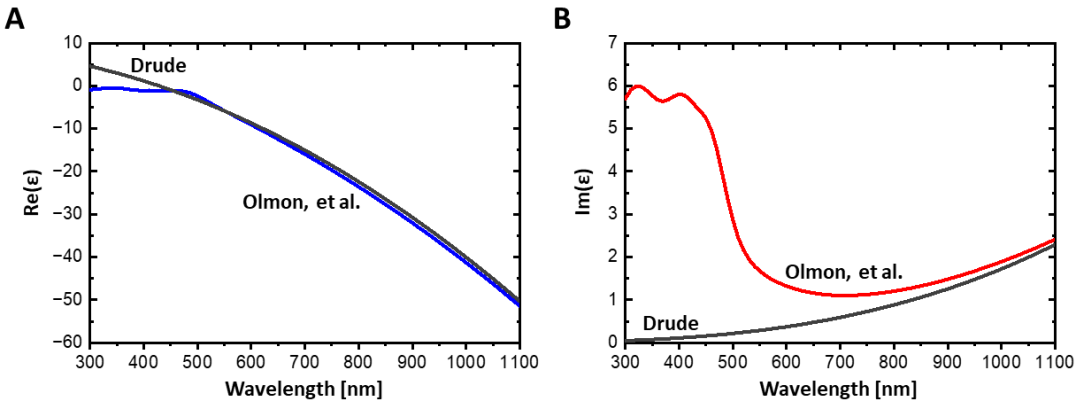

Figure 2.2.1: Comparison between Drude and experimental Permittivities of Gold. A Experimental Real part of permittivity (blue) of monocrystalline Gold [55] and corresponding fit (grey). **B** Imaginary part of permittivity (red) of Gold and corresponding fit (grey). Fitting parameters used were ε_∞= 9, ω_p = 1.32·10^{16}s^{-1} and γ = 6.62·10^{13}s^{-1}. This figure is after reference [56].

Figure 2.2.1 A and **B** reveal a relative similarity between the real part and a stark difference between the imaginary part of gold's measured permittivity [55] and their Drude-modelled counterparts. Particularly for wavelengths below 600 nm the measured imaginary permittivity is significantly higher due to interband damping. The difference continues but levels off for wavelengths above ~690 nm. This is the threshold for interband damping due to excitations from the d- into the sp-conduction band for gold [57]. With the focus of Raman measurements in this work being close to the NIR (671 nm and beyond), the most lossy parts of gold's permittivity are avoided. The discrepancy between measured and Drude permittivities are however still relevant. In principle, the analytical Drude-Lorentz model can be used to account for interband transitions, where Lorentzian oscillator terms are incorporated into the dielectric function [53]. Within the scope of this thesis however, interpolations from measured data are employed for calculations.

Whilst these parameters are derived from the interiors of bulk crystals, they are still essential to conduction band electron oscillations at the surfaces of metals. In their plainest form, they exist at the surfaces of spherical metal nanoparticles significantly smaller than the incident wavelength of light that excites them in a vacuum. This is illustrated in **Figure 2.2.2 A** and **B**. By shrinking

the particle, it can be modelled as a point-like dipole experiencing homogeneity in the exciting light field's phase. This enables a quasi-static approximation of the illumination as a plane wave with a constant field, exciting the conduction band electrons coherently. Mie Theory [25] then allows for an analytical derivation of the antenna's LSP resonance.

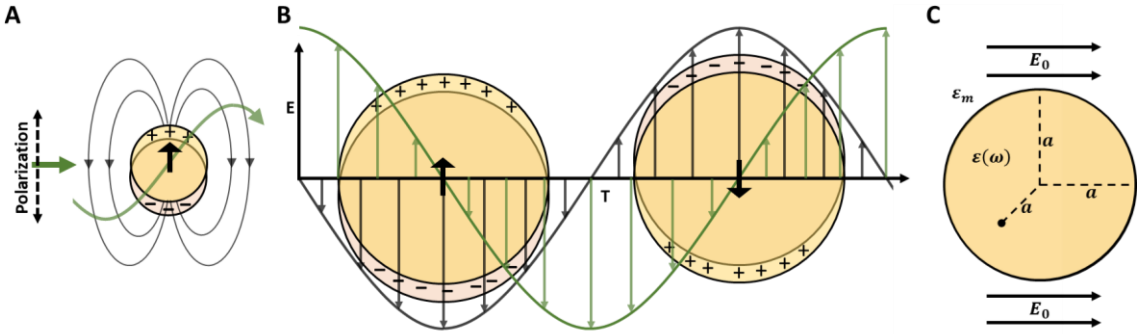

Figure 2.2.2: Particle Plasmon and Mie Theory Parametrization. A Illustration (not to scale) of particle plasmon excited by light (green), with field lines (translucent black) and dipole orientation (bold black arrow). The plasmonic oscillator is maximally displaced in terms of charge. **B** Sketch of time dependent plasmonic field (translucent black), due to oscillating excitation field (green). Dipole orientations (bold black) depicted for two points in time (with corresponding charge displacement sketches). Here, the shift between excitation and plasmonic dipole corresponds to a 90° phase lag for an oscillator in resonance. **C** Illustration of parameters relevant to Mie theory modelling.

The parameters necessary for implementing Mie theory are depicted in **Figure 2.2.2 C**. Here, a sphere with a permittivity of $\varepsilon(\omega)$, a radius of a, and a radius vector $\boldsymbol{r}(\theta)$ sits in a homogenous electric field $\boldsymbol{E_0} = E_0 \cdot \boldsymbol{e}_x$, in a medium with the homogenous permittivity ε_m. To solve the Laplace Equation $0 = \Delta\Phi$, for the given azimuthal symmetry of the potential, the Legendre Polynomial $P_n(\cos\theta)$, with corresponding constants A_n and B_n, can be used [53]:

$$0 = \Delta \sum_{n=0}^{\infty} [A_n r^n + B_n r^{-(n+1)}] P_n(\cos\theta) \tag{2.19}$$

Continuity at $r = a$, as well as non-divergence of fields, which requires $\Phi(r \to \infty) = -\boldsymbol{E}_0 \cdot \boldsymbol{r}$, are fulfilled with:

$$\Phi_{int} = -\frac{3\varepsilon_m}{\varepsilon(\omega)+2\varepsilon_m} E_0 \cdot r\cos\theta, \tag{2.20}$$

and

$$\Phi_{ext} = -E_0 \cdot r\cos\theta + \frac{\boldsymbol{P}\cdot\boldsymbol{r}}{4\pi\varepsilon_o\varepsilon_m r^3}. \tag{2.21}$$

For the internal and external case respectively. Here $\boldsymbol{P} = \varepsilon_o\varepsilon_m\alpha\boldsymbol{E}_0$ represents the sphere's dipole moment, which incorporates the sphere's complex polarizability:

$$\alpha = 4\pi a^3 \frac{\varepsilon(\omega)-\varepsilon_m}{\varepsilon(\omega)+2\varepsilon_m}. \tag{2.22}$$

It clearly indicates the resonance of the spherical particles dipole moment, when the Fröhlich condition [58] is met:

$$Re[\varepsilon(\omega)] \equiv -2\varepsilon_m. \tag{2.23}$$

The condition is most accurate for an electrically undamped metal, where:

$$\varepsilon(\omega) = 1 - \frac{\omega_p^2}{\omega^2}. \tag{2.24}$$

For spherical metal particles much smaller than the incident wavelength in vacuum, it is fulfilled when $\omega = \omega_p/\sqrt{3}$. In practice, the condition red-shifts with increasing sizes [59]. This stems from retardation effects across the particle [60]. Such delayed interaction between charges across a physical antenna is not applicable to a theoretical point dipole. Additionally, multipolar modes become relevant at larger fractional sizes of the excitation wavelength [60]. The antenna length criterion for these effects can be as small as 10% of the local wavelength [27], which is applicable to nanoparticles in this work.

In general, the LSP also red-shifts in higher permittivity media, whilst blue-shifting for metals with higher plasma frequencies, as per **Equation 2.23** and **2.24**. At this point it is also apparent that both particle polarizability as well as potential are greatly enhanced at resonance. At the same time, these are constrained by plasmon damping, accounted for by the imaginary part of the metal's permittivity. The increased polarizability of plasmonic nanoparticles results in an increase in both effective scattering and absorption cross section, the sum of which forms the interaction or extinction cross section via:

$$\sigma_{scat} + \sigma_{abs} = \sigma_{ext}. \tag{2.25}$$

The values are related to α, with the wave vector $k = 2\pi/\lambda$, in the following manners [53]:

$$\sigma_{scat} = \frac{k^4}{6\pi} \mid \alpha \mid^2, \tag{2.26}$$

$$\sigma_{ext} = k \cdot Im(\alpha). \tag{2.27}$$

In the case of Drude modelled permittivities, without interband transitions, the line-shapes of such cross sections are in fact Lorentzian (in energy) [59]. This follows from a simplified damped harmonic oscillator nature of such particle plasmons. In reality, interband damping can suppress, broaden and otherwise alter resonance significantly.

Large interaction cross sections go hand in hand with E-field enhancement in the (near field) vicinity of the particle [49] in general:

$$\boldsymbol{E}_{ext} = -\boldsymbol{\nabla}\Phi_{ext} = \frac{1}{r^3}\frac{3\boldsymbol{e}_r(\boldsymbol{e}_r\cdot\boldsymbol{p})-\boldsymbol{p}}{4\pi\varepsilon_o\varepsilon_m}. \tag{2.28}$$

And for its maximum, at the poles of the sphere's surface, here in x direction, in particular:

$$\boldsymbol{E}(\boldsymbol{r} = a\boldsymbol{e}_x) = \boldsymbol{E}_0\frac{3\varepsilon(\omega)}{\varepsilon(\omega)+2\varepsilon_m}, \tag{2.29}$$

where a significant field enhancement becomes apparent in the case of the metallic nano-spheres. Again, it is however constrained by plasmon damping.

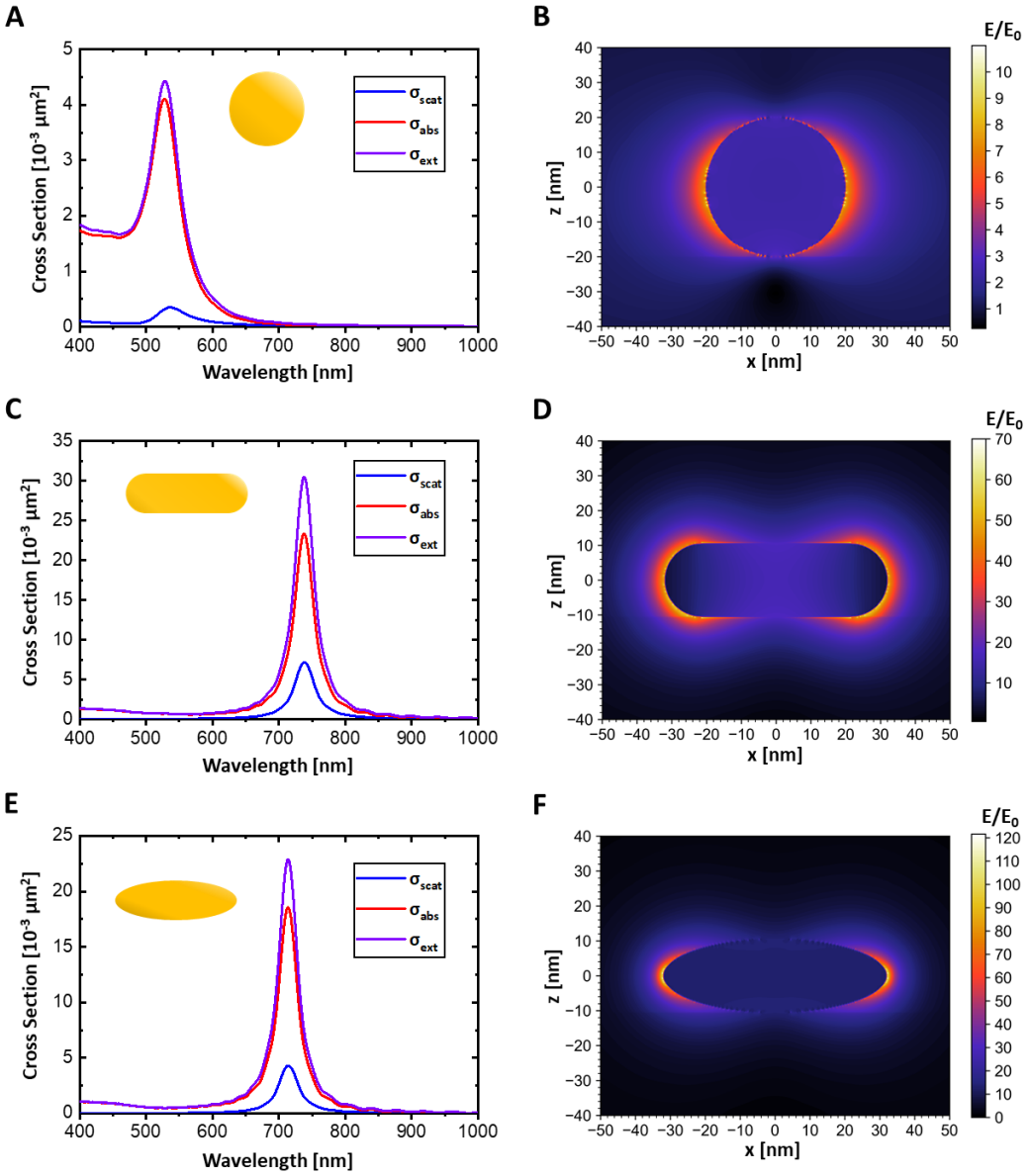

Figure 2.2.3: Plasmonic Properties of single Nanosphere, Nanorod and Nanoellipsoid. A Longitudinal (and transversal) scattering, absorption and extinction spectrum of single 40 nm (diameter) gold sphere. **B** Longitudinally excited sphere E-field enhancement (at 544 nm). **C** Interaction cross sections of single 21 × 64 nm GNR. **D** E-field enhancement GNR (at 738 nm)**. E** Interaction cross sections of single Ellipsoid (at 716 nm). **F** E-field enhancement of 21 × 64 nm Ellipsoid. Calculations were conducted with nanoparticles on glass in water, with longitudinally polarized excitation. Limited waviness in the spectra indicates that the calculations have converged reasonably well.

An exemplary numerical calculation (explained in **Section 3.2.1**) for metal nanosphere optical interaction cross sections, as well as field enhancement are displayed in **Figure 2.2.3 A** and **B** respectively. Here, the peak extinction cross section is significantly greater than the geometric one (~$1.3 \cdot 10^{-3}$ µm^2), and electric fields are enhanced by an order of magnitude in the particle vicinity. Together with resonance and damping of the plasmonic oscillator, particle shape itself

will also influence E-field enhancement significantly. A prominent example – central to this thesis − are noble metal nanorods, where the loss of geometric symmetry coincides with the emergence of a red-shifted longitudinal plasmon peak [26]. Here, an increase in aspect ratio (length divided by width) of GNRs leads to a red-shift of the plasmon mode [59].

The rods examined here are approximated as spherically endcapped cylinders, with an example of longitudinal optical cross sections and field enhancement given in **Figure 2.2.3 C** and **D**. Field enhancement is significantly higher than for the sphere (at 544 nm), which can be linked to the GNR plasmon resonance around 730 nm being red-shifted from interband transitions, leading to a significant reduction in surface plasmon damping [59]. Additionally, the GNR's ends feature greater curvatures relative to the particle size (compared to spheres), and further concentrate charge displacement and field enhancement. These ends can be thought of as sharper tips.

Whilst such aspects cannot be calculated for nanorods analytically, they can be for an ellipsoid of comparable dimensions. This might provide very similar solutions in terms of longitudinal plasmon resonance location compared with GNRs, as shown in **Figure 2.2.3 E**. More specifically, the shape features a limited blue-shift in longitudinal resonance, by 22 nm for field enhancement, compared to its more bluntly tipped aspect ratio counterpart. However, as will later be explored further, ellipsoid tip E-field enhancement, depicted in **Figure 2.2.3 F**, is significantly greater than for GNRs due to even higher effective tip sharpness. The particles are also not analyzed in a homogenous medium, but rather on substrates presenting asymmetries which are more difficult to account for analytically. The experimental conditions and importance of E-field enhancement in this work thus necessitate numerical modelling.

Beyond spheres and rods, a variety of different plasmonic nanoparticle geometries with sharper tips have been generated, with a view towards even higher E-field enhancement factors. These include gold nanostars [61, 62], gold nano triangles [63-65], and bipyramids [66, 67]. Nanostars in particular feature high (several 10^2) field enhancements [62] – beneficial for SERS, as highlighted by **Equation 2.1** and discussed in **Subchapter 2.1** − albeit localized to their tips. In contrast, the following section deals with an increase of E-field enhancement via proximity of two metallic nanoparticles to one another.

2.2.2 Plasmonic Nanoparticle Coupling

Besides sharper tips and lower imaginary permittivities, coupling plasmonic nanoparticles will also lead to an increased field enhancement (around longitudinal plasmon resonance), via a hotspot in corresponding gaps [68]. This stems from an overlap of the near fields of particles

when excited longitudinally to the dimer axis, leading to plasmonic coupling. The corresponding bonding dipolar mode (BDP) forms the basis of SERS in this thesis. It is illustrated in **Figure 2.2.4 A**, as an antisymmetric component of bisphere plasmon hybridization [69]. Here particle dipoles oscillate in parallel, slowing each other down by lowering each other's restoring forces through attractive coulomb interaction of displaced charge densities [53]. This near-field coupling leads to a red-shift in the mode when compared to a single oscillator. A symmetric counterpart, to this, namely the antibonding dark mode can also be distinguished. It is blue shifted to the single particle mode, from charge density repulsion at the gap contributing to restoring forces of the dimer halves. As alluded to by its name, and unlike bright modes, it is not excitable optically by a conventional (linearly polarized) light source [70], due to its lack of overall polarizability and dipole moment. Coupling along the transversal axis exists analogously, but is less pronounced [71]. It can also not contribute significantly to charge displacement around – and field enhancement inside – the gap, as polarization is excited perpendicularly to its span.

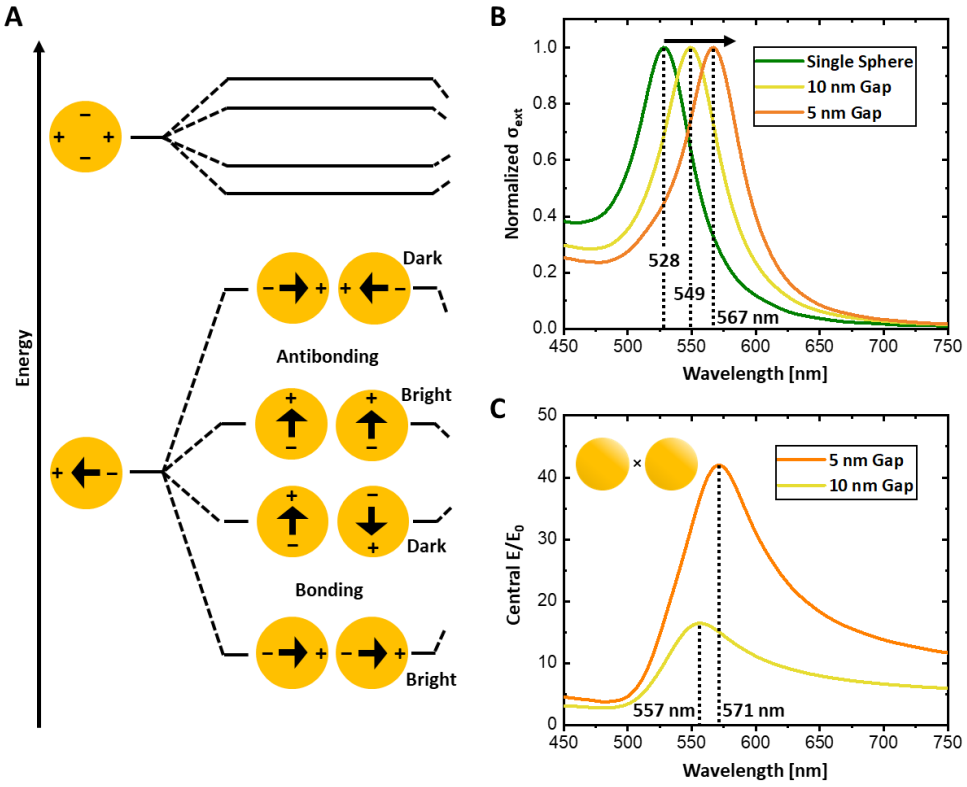

Figure 2.2.4: Coupled Plasmonic Nanoparticles. A Illustration of nanosphere dimer plasmon hybridization. **B** Longitudinal polarization extinction spectra of single and coupled gold nanospheres (40 nm on glass in water). Here the single sphere correspond to an infinite gap span. **C** E-field enhancement, for longitudinal excitation, at centres of dimer hotspots in B. A is after reference [56].

As gaps (with D as a span) shrink, coupling increases. In particular, the longitudinal bonding plasmon red-shifts [71-73], as is depicted in **Figure 2.2.4 B**, where increased attractive dipole-dipole coupling slows down (GNS dimer) plasmon oscillation. Conversely, antibonding modes blue-shift with further coupling. More specifically, according to approximations by Simpson & Peterson [74], for first order bonding dipole-dipole interaction, energy differences involved scale

with $1/D^3$. However, coupling to modes of different orders leads to even stronger plasmon resonance scaling with D and thus further increased red-shifts from smaller gaps [69].

Coupling alone increases E-field enhancement around the particles significantly, with further decrease in interparticle spacing leading to even higher values in the gap [38, 75]. The effect can also be seen in **Figure 2.2.4 C**. It illustrates one of the key trade-offs in this field and thesis, namely that of hotspot size vs. electromagnetic enhancement. An analytical analysis of the effect is difficult (at best) due to complexity of the problem, involving non-point-like dipoles. This is also why a numerical approach is used here.

In principle, numerical calculations also consider higher order modes. However, usually, the longitudinal bonding mode dominates, with the largest overall dipole moment, strongest coupling, and thus E-field enhancement. Therefore, it is also the main point of study here. As an example, for 60 nm gold nanosphere dimers with gaps in the 1.2-3.5 nm range, calculated E-field enhancement has been reported in the region of 10^2, by Tapio et al. [40], on silicon substrates in air. Here for glass, and bare 40 nm gold nanospheres with larger 5 nm gaps in water, a hotspot central enhancement factor of 42 can be seen in **Figure 2.2.4 B**. This factor falls to 16 for 10 nm gaps but is still significantly larger than at (particularly at nm distances from) a single gold nanospheres (**Figure 2.2.3 B**). Intriguingly, further decreasing D to sub-nm sizes, is calculated to generate limited maximum hotspot central field enhancements, by Esteban et al. [76]. The maximum value around ~1-2000 for gold spheres in a vacuum, was found to stem from quantum tunneling. Here electrical contact suppresses charge displacement between the dimer halves, and thus the BDP mode. Such field enhancements stem from build ups of high charge densities [77]. Here, impact on electrons of nonlocal (to the electron position) electromagnetic fields can become considerable [27]. Particularly for sub-nanometer gaps, but also small metal nanoparticle diameters (under 10 nm), as well as high curvatures. This can also affect plasmon resonance notably, where BDP modes might blue-shift due to effectively lowered charge densities at gaps reducing plasmon coupling, for example. For classical calculations in this work, with a main focus on several nanometer sized gaps, nonlocal effects are however not implemented. With these distances between plasmonic nanoparticles, the impact of such effects is decreased significantly [78, 79].

2.2.3 Optical Forces

Plasmonic antennas can be subject to significant optical forces, in a focused laser beam. The effect has been used both for trapping [80-83], as well as for printing [81, 84] single metallic nanoparticles. The first aspect stems from gradient forces pulling the antenna into the region of highest light intensity, and is illustrated in **Figure 2.2.5 A**. The second is the result of scattering

force from light [85], along its Poynting vector, and is sketched in **Figure 2.2.5 B**. Scattering forces stem from momentum transfer due to directionally absorbed photons with $p = \mathrm{h}/\lambda$, and more isotropically released energy. When gradient forces overweigh the particle is trapped. If scattering forces overweigh it can be printed.

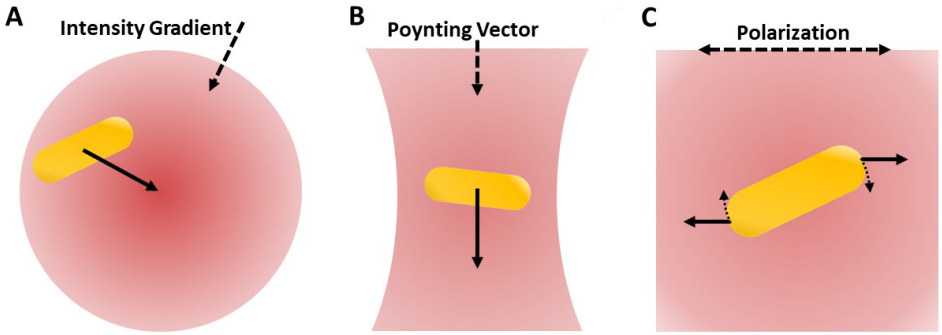

Figure 2.2.5: Illustration of Optical Forces. A Gradient force pulls the particle into maxima of the optical intensity distribution. **B** Scattering force pushes the particle along the Poynting vector of the light beam. **C** Optical torque pulls the particles axis with highest polarizability in parallel with polarization of the oscillating excitation field. The dashed arrows indicate properties of the light source, the full arrows indicate force vectors, and the dotted arrows indicate rotation.

Interestingly, optical forces do not act on single plasmonic antennas uniformly. For example, they can align particles with aeolotropic polarizabilities such as GNRs, in parallel to the light's polarization [80, 81, 86, 87]. This is depicted in **Figure 2.2.5 C**. These principles also apply to dielectric particles [88]. Additionally, they can manifest as differential forces in other axes, an example being force maxima at centres of longitudinally excited GNRs, calculated by Liaw et al. [89]. Further, excited particles can interact with one another. This can become particularly relevant between two coupled plasmonic nanoparticles forming a hybridized single resonator [90, 91], as will be discussed in later parts of this thesis. To account for these effects, volumetric force can be determined. Plasmon oscillations can be modelled as coherent charge density ρ displacements with a time dependent velocity $\boldsymbol{v}$. Here, particle volume elements V are subject to electromagnetic Lorentz forces via:

$$\boldsymbol{F} = \int_V \rho(\boldsymbol{E} + \boldsymbol{v} \times \boldsymbol{B})\, dV. \tag{2.30}$$

With the help of the Maxwell stress tensor (MST) $\boldsymbol{T}$ expressed componentwise using indices i and j [92]:

$$T_{ij} = \varepsilon_0 (E_i E_j - \tfrac{1}{2}\delta_{ij} E^2) + \tfrac{1}{\mu_0}(B_i B_j - \tfrac{1}{2}\delta_{ij} B^2), \tag{2.31}$$

and the pointing vector:

$$\boldsymbol{S} = \boldsymbol{E} \times \boldsymbol{H} = \boldsymbol{E} \times \frac{\boldsymbol{B}}{\mu_0}, \tag{2.32}$$

$\boldsymbol{F}$ can be expressed as a time-dependent force density:

$$\boldsymbol{f}(t) = \boldsymbol{\nabla} \cdot \boldsymbol{T} - \varepsilon_0 \mu_0 \frac{\partial}{\partial t} \boldsymbol{S}. \tag{2.33}$$

Time averaged, the force density is then:

$$\boldsymbol{f}(t) = \boldsymbol{\nabla} \cdot \boldsymbol{T}. \tag{2.34}$$

For volumetric elements with surfaces defined by S, with a unit normal $\hat{\boldsymbol{n}}$, this yields a total force of [92]:

$$\boldsymbol{F} = \oint_S \boldsymbol{T} \cdot \hat{\boldsymbol{n}}\, dS. \tag{2.35}$$

Such volume and surface element derivations of electrodynamically induced force are fundamental to numerical methods for calculating both dipole-dipole, as well as dipole laser interactions. These are introduced in greater detail in **Section 3.2.1** of this work.

2.2.4 Plasmonic Decay and Heating

Excited particle plasmons decay along two broad pathways, one radiative, and one nonradiative. Whilst the first can be detected directly by optical means, the second usually manifests in heat, but also other forms of localized energy dissipation. Longer plasmon lifetimes T_2 correspond to reduced linewidths Γ via $T_2 = 2\hbar/\Gamma$ of the plasmonic oscillators Lorentzian response curve [59], with an example shown in **Figure 2.2.6 A**. Reduced plasmon damping goes hand in hand with higher E-field enhancements, and vice versa [93]. Here, damping defines interaction cross sections, which correspond to excitability and thus field enhancement from a particle plasmon mode. Plasmon decay is thus an essential component of plasmonic nanoagents, particularly for SERS, from multiple perspectives. Its components are illustrated in **Figure 2.2.6 B** and described in the following part of this section.

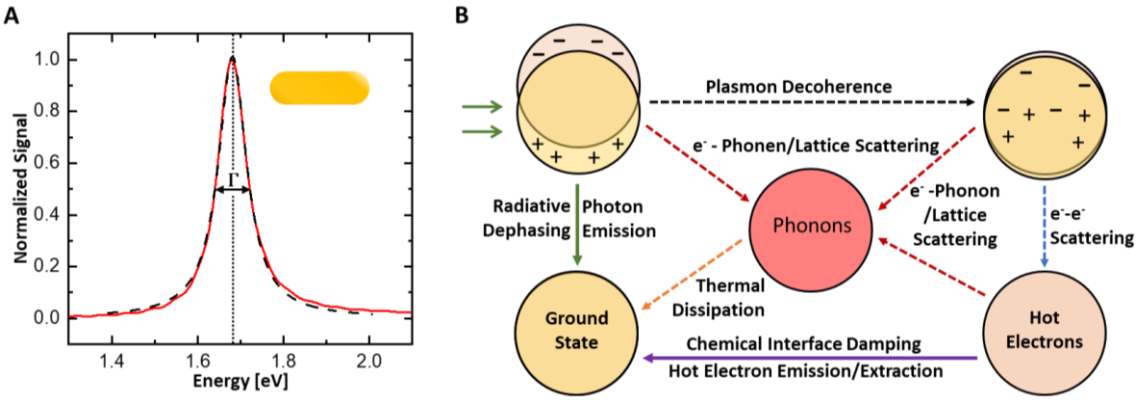

Figure 2.2.6: Plasmon Dephasing. A Normalized calculated longitudinal extinction spectrum (in energy space) of a 21 × 64 nm GNR on glass, in water (red line) and Lorentzian fit (black dashed line, with Γ = 80.7 meV = 651 cm^{-1}). Here the dotted black line indicates the energy at which the antenna displays maximum E-field enhancement in Figure 2.2.3 D (1.68 eV). **B** Sketch of different pathways of plasmon decay. Here, scattering and dissipative processes marked by dashed and emissive processes by solid lines.

Radiative decay is straight forward and takes place via photonic emission from the oscillating plasmon dipole. It is assignable with a decay rate of T_r^{-1}. Nonradiative decay with T_{nr}^{-1}, on the other hand, is more complex. It can be subdivided into its constituents: intraband damping (T_{intra}^{-1}), interband damping (T_{inter}^{-1}), pure (or elastic) dephasing (T^{*-1}), and chemical interface damping (CID, T_{CID}^{-1}). Intraband damping can take place in different ways. For one, scattering of bosonic LSP electrons with the (ground state) lattice creates phonons according to the Drude-Sommerfeld model [94], thus heating the metal. With experiments commencing at room temperature, electrons scattering with phonons will also have to be considered [55, 95]. Interband damping [96] on the other hand occurs when electrons are lifted from lower bands into the conduction band. For gold, from the d-band to the Fermi Level, this requires a photon energy around 1.8 [57] (689 nm). Interband damping is however lowered significantly below 2 eV (620 nm) [59], where plasmon resonances delt with in this thesis lie.

Another aspect is pure dephasing, where the plasmon scatters off of imperfections such as impurities, grain boundaries, as well as surface roughness [97]. Chemically synthesized gold nanorods with radii exceeding 10 nm have been found almost free of such faults [98]. Bellow this radius surface scattering can however become significant [99]. The plasmon thus decoheres and destructively interferes with itself. Thereby further electron-electron scattering can lead to hot electrons. These in turn can heat the lattice by scattering with phonons [100]. They can also be emitted from the particles interface [101-103], with the potential of driving chemical reactions [104-106]. The latter CID process has also been studied in the context of nanoparticle adsorbate coupling to glass substrates leading to virtual states close to the Fermi level [107], as well as such states matching excitation energy [97]. In some cases, it has been found negligible [59].

Dephasing times T_2 of the particle plasmon are on the order of ~1-10 fs [59, 108]. Electron-electron and electron-phonon scattering have been timed with ~1 ps and ~1-10 ps respectively [108, 109]. Finally, thermal dissipation and thus equilibration timescales for continuous wave (CW) excited particles are on the order of 100 ps [110-112]. Plasmonic heating is therefore a sub-nanosecond process here.

3 Methods to Characterize and Model GNR-Based Plasmonic Dimers

Within the scope of this work, several different techniques have been used to measure and analyze plasmonic nanoantenna systems. This starts with dark-field microscopy to characterize and spectroscopically measure nanoparticles. Such measurements were supplemented with electron microscopy for structural characterization. Further, electrodynamic properties of antenna systems and plasmonic heating were analyzed numerically. These techniques are described in the following subchapters.

3.1 Nanoagent Characterization and Use

This subchapter describes setups and methods used for optical scattering and Raman spectroscopy, as well as imaging of the plasmonic nanoantennas employed in the scope of this thesis. It spans dark-field (DF) microscopy (DFM) and spectroscopy, as well as scanning and transmission electron microscopy (SEM and TEM respectively).

3.1.1 Raman and Scattering Spectroscopy with a Dark-Field Microscope

Both Raman, as well as single-particle scattering spectroscopy require an optical microscope for locating and measuring nanoantennas. Dark-field microscopy used here, is an imaging technique for detecting scattered light in front of a dark background [59], and therefore well suited to the task. It functions similarly to bright-field microscopy, but differs in that illumination is aimed around the microscopy objective. Lighting is implemented in the form of a hollow cone, and takes place from below the substrate. The cone's inner surface requires a larger numerical aperture NA ($n \cdot \sin(\alpha)$, with refractive index n and angle of incidence α) than that of the objective. This is achieved using a white light source directed through a dark-field condenser. The corresponding setup is illustrated in **Figure 3.1.1 A** and **B**.

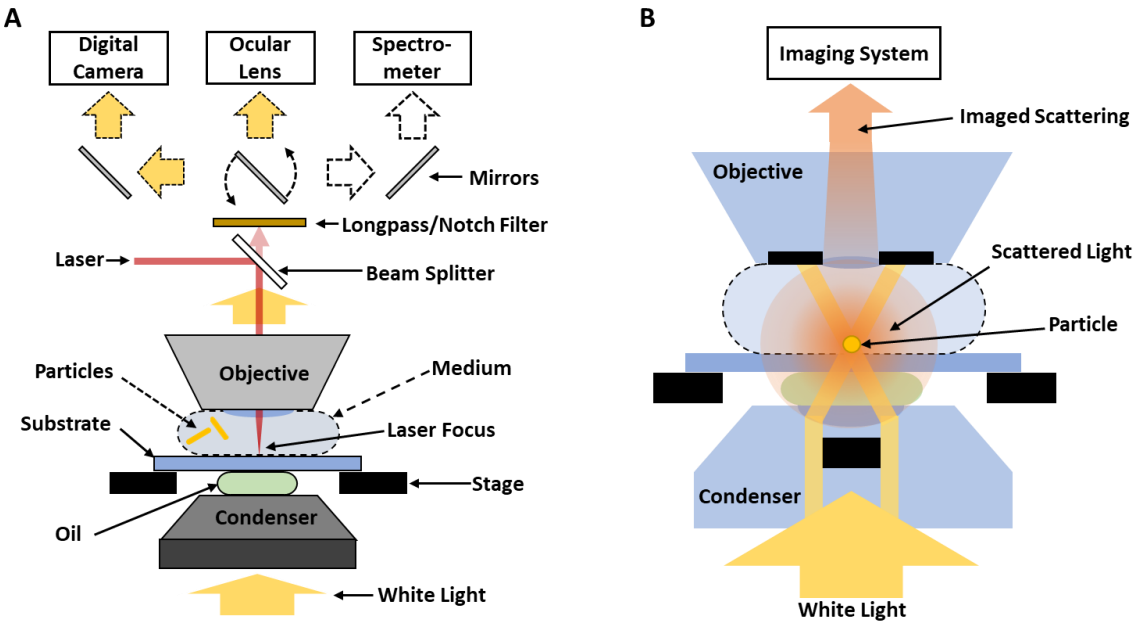

Figure 3.1.1: Dark-field, Optical Printing and Raman Scattering Microscope Setup. A Scheme of dark-field microscope setup used for experiments on glass-substrate-based samples. The setup enables switching between both optical microscopy by camera and eye, as well as spectroscopy, whilst incoupling a laser (with a system of mirrors for alignment). **B** Sketch of dark-field microscopy, where light is guided through the sample around an objectives entrance by the condenser, so that only scattered light is imaged.

This allows for analyzing the sub diffraction limit sized nanoantennas, with their small optical cross sections, which is possible in both air and water. In the latter case, fluid volumes were

around 100 µl, with further *Milli-Q* purified water added to compensate for evaporation. The light scattered by the particles, can be outcoupled to both a CMOS (complementary metal-oxide-semiconductor)-based digital camera for imaging (*Canon EOS 6D*), as well as a CCD (charge-coupled diode)-based spectrometer (*Princeton Instruments SpectraPro 2500* with a *Spec-10:2k CCD*). The spectrometer functions by diffracting light, first guided through an adjustable slit, with a one-dimensional grating. The diffracted light illuminates the CCD chip (*Princeton MicroMax*), which thereby resolves one dimension in frequency, and one dimension in real space. This allows for detecting scattering spectra. For this, two regions of interest are selected (in real space), where one contains a particle to be analyzed and another contains background. The latter spectrum is subtracted from the first, prior to normalizing with a third spectrum gained from the illumination source using a milky glass substrate. This requires a distance between the target and its surroundings. Otherwise, spectra might be distorted by non-representative background signal, potentially containing significant peaks from scattering by other antennas for example.

Additionally, the DFM setup used allows for Raman and SERS measurements, by incoupling a laser through the objective, and targeting particles of interest. Raman scattered light was selected to be resolved with the spectrometer, by introducing a longpass filter to block back-reflected and scattered laser irradiation. Incoupling and focusing of a red or NIR laser into a DFM setup also allowed for visually monitored optical printing. Here a matching notch filter could be inserted to block visually obstructive back reflection of the laser whilst printing.

The DFM used here for scattering and Raman spectroscopy was a *Zeiss Axio Scope A1*, with a sample stage including substrate holder and dark-field condenser. The stage was motorized in xy, and with z – the focal axis – requiring manual adjustment. The illumination source employed was halogen white light-based. Condensers used were a *Zeiss 465505* (NA of 0.8-0.95) for some measurements in air, and a *Zeiss 445323* (NA of 1.2-1.4) for measurements in air and water. Main objectives utilized for measuring were a *Zeiss Epiplan HD* 50x NA 0.7 objective in air, and a *Zeiss Achroplan* 100x NA 1.0 *W* in water. The CW laser used for Raman measurements was a *Novanta Gem 671* (solid state, 671 nm, 500 mW), with a lambda quarter plate inserted into the beam path for circular polarization. Power was adjustable with a variable neutral density (ND) filter. Its focus featured a full width at half maximum of 560 nm, in water. Optical printing was conducted using a similarly equipped setup, with a *Cobolt Rumba* (Nd:YAG, 1064 nm, 3 W) CW laser (linearly polarized with adjustable power). Its beam was expanded to fill out the entrance pupil of a 63x NA 1.0 *Zeiss W-Plan Apochromat*.

Additional experiments in air, for heating plasmonic antennas, were carried out using a *WITec alpha300* series dark-field microscope (Hynano Chair, LMU Munich). It was equipped with a 633 nm laser, and imaging was conducted with an NA 0.95 100x *Zeiss* Air objective.

Due to the small energy differences involved in Raman spectroscopy (1 nm of deviation in wavelength at 671 nm corresponds to 22.2 cm^{-1} in terms of wavenumber) good alignment of the setup is important. Calibration of the spectrometer was conducted with a silicon substrate. Here resolving a distinct Raman peak at 521 cm^{-1} [113], ensured correct alignment of the setup. Raman spectra can also feature a significant background signal. An approximation of this signal was subtracted from certain spectra, for improved visual clarity. The background could be approximated by fitting a polynomial function, with significantly lower curvatures than observed Raman peaks, to local minima in the spectrum.

3.1.2 Electron Microscopy for Increased Spatial Resolution

Microscopy in general – and optical microscopy in particular – is inherently diffraction limited in resolution, describable via the Abbe limit $d = 0.5\ \lambda/\mathrm{NA}$. To structurally image the significantly smaller nanoantennas studied here, scanning electron microscopy was used. Its electron matter wavelength (λ) is related to its electron impulse (p) via the de Broglie equation: $\lambda = \mathrm{h}/p$, with h as Planck's constant. For an acceleration voltage U of 3-10 kV, as used here, this results in λ = 23-12 pm, from:

$$\lambda = \frac{h}{\sqrt{2eUm_e}}, \tag{3.1}$$

with e as the electron elementary charge, and m_e as their mass. Even with the low NAs on the order of 10^{-2} used for electron microscopy, resolution is thus still considerable at up to ~1-2 nm. For larger energies resolution does however not scale as significantly anymore, due to relativistic effects.

To generate such energies, electrons are first extracted from a filament (cathode) tip via an electric field (field-emission-SEM) [114]. They are then accelerated in an electric potential of an electron gun, and then focused onto the sample surface by an electromagnetic lens system. By rastering (or scanning) the beam across the sample whilst detecting both directly backscattered and secondarily generated electrons, the surface can be mapped to form an image. Here such electrons were sensed using a combination of Inlens and conventional secondary electron SE2 detectors. The first (Inlens) consists of a ring integrated into the electron lens column. It offers a particularly high spatial resolution. The second (SE2) is mounted outside the electron lens system and includes a Faraday cage to attract and thereby accelerate lower energy electrons towards it. It allows for detection of electrons scattered close to the sample surface. This is illustrated in **Figure 3.1.2 A**. For this work, a combination of Inlens and SE2 detection, enabled by an *Ultra 55 SEM* (*Zeiss*), offered a favorable mix of high resolution and topological contrast. Here, for non-electrically conductive substrates, such as glass, charging was prevented by coating the SEM

samples with a ~1 nm gold-palladium layer. This was done using a *Leica EM SCD005* sputter coater.

The *Ultra 55 SEM* microscope could also be used in transmission mode (STEM or T-SEM) [114, 115], as sketched in **Figure 3.1.2 B**. Here, electrons which travel through the substrate directly (without being scattered by the sample and caught in the electron trap) generate measurable SE2 electrons via a conversion detector. In this case, image contrast is derived from sample transmission. In this case, imaging was conducted with an electron acceleration voltage of 30 kV.

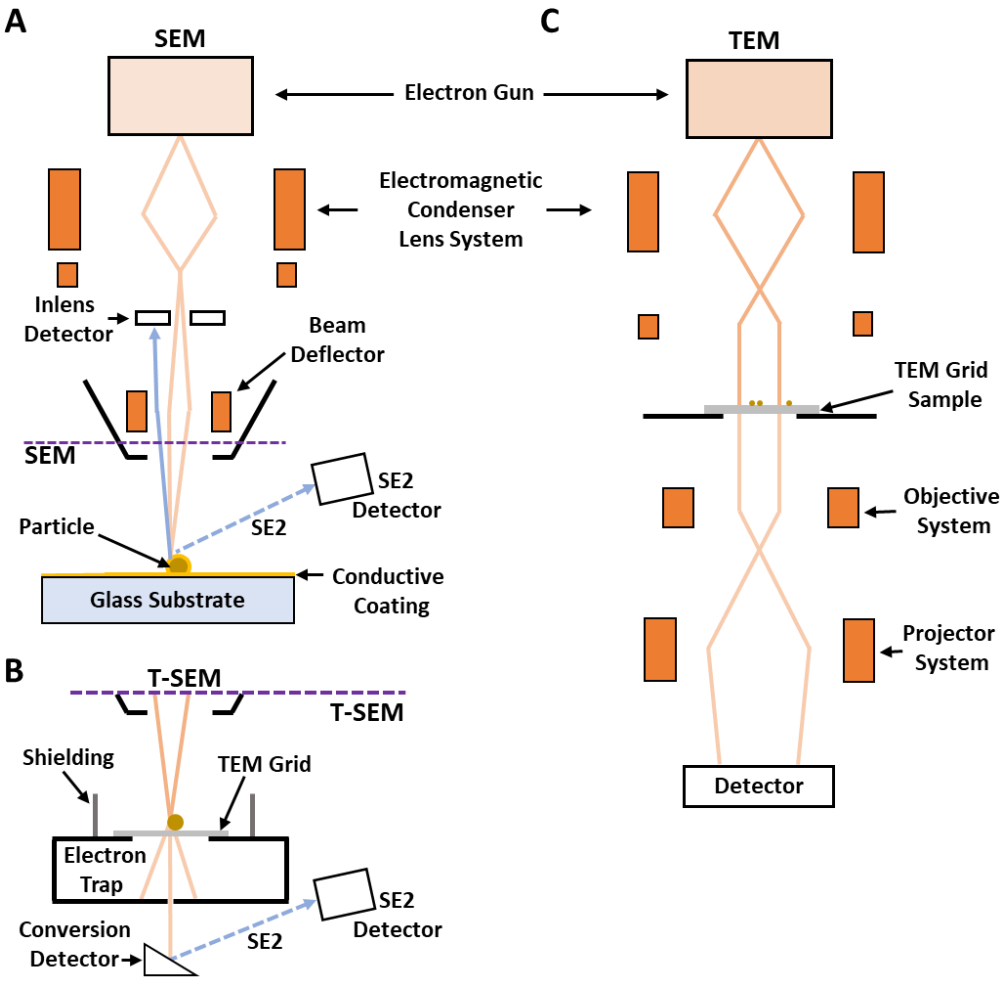

Figure 3.1.2: Illustration Electron Microscopy. A Schematic of scanning electron microscopy. Here the substrate rests on an additional stage, allowing for more range of motion, beyond that of the scanning electron beam. The dashed purple line serves to distinguish between A and B. **B** Schematic of transmission scanning electron microscopy. **C** Simplified schematic of transmission scanning electron microscopy. The schematics are not to scale.

For added resolution and material-contrast to visualize nanoscopic gaps and DNA origami scaffolds of dimers, conventional transmission electron microscopy was employed, which is illustrated in **Figure 3.1.2 C**. Again, imaging contrast is derived from sample transmission, detected with a 2D CCD sensor, which is 2 dimensional for image resolution [114]. For this, a

JEM-1101 (*JEOL*) TEM was used at an electron acceleration voltage of 80 kV (by K. Kolataj, Liedl Group, LMU Munich).

Additionally, for even higher resolution, high-angle annular dark-field scanning TEM (HAADF-STEM) [116] was employed. This enables higher material contrast, via Rutherford scattered electrons (from the atomic nucleus). Here, it was conducted with an *FEI Titan Themis* (by M. Döblinger, Department of Chemistry – Bein Group, LMU Munich), with a 300 kV electron acceleration voltage.

Transmission electron microscopy requires transmissive substrates. For the T-SEM and HAADF-STEM measurements 50 nm silicon nitride (Si_3N_4) membrane TEM grids (*Plano GmbH*) were used. For conventional TEM, *300 mesh Cu* (*Ted Pella, Inc.*) grids were employed.

3.2 Nanoantenna Numerical Modelling

Three numerical methods were used for modelling physical phenomena relevant to SERS with plasmonic dimers. Firstly, electromagnetic properties and effects were calculating using the finite-difference time-domain method (FDTD), a standard method for applications with complex particle geometries [60]. For this, the commercial software *Lumerical FDTD* (*Ansys Lumerical*) was used. Optical absorption derived by FDTD could be used in combination with finite element modelling (FEM) *COMSOL Multiphysics 5.2a* (*COMSOL Group*), to determine plasmonic heating effects. These are described in the following two sections. Additionally, a simple random walk model was implemented in *Python* for simulating protein diffusion.

3.2.1 Electrodynamic Effects from Finite-Difference Time-Domain Calculations

The finite-difference time-domain method, involves grid-based differential numerical modeling for solving Maxwell's time-dependent partial differential equations, as demonstrated by Kane S. Yee in 1966 [117]. It does so by alternating between magnetic, and electric field calculations at all grid locations, solving Maxwell's equations in a temporally and spatially discretized rhythm. To do so, the simulation volume is partitioned into so called Yee-cells; named after their inventor. Here, separate grids for magnetic and electric field strength calculation are interwoven in an equally spaced manner. This Method of meshing is illustrated in **Figure 3.2.1 A** and **B**. Modelling for both gold nanorod, as well as nanosphere dimers is illustrated with **Figure 3.2.1 C**.

The mesh-points are in turn assigned with frequency dependent n (real) and k (imaginary) coefficients of the complex refractive index according to the structures modeled in the simulation region. Mesh density is then chosen with an appropriate spatially varying (sub-nm in metallic regions) density. Here meshing was generally done with a 0.2-0.4 nm spacing, encompassing the whole plasmonic nanoantenna with an additional size margin of ~10%. For particularly small gaps between particles (≤1-5 nm), meshing resolution in the gap area was increased (by lowering grid constants down to 0.01 nm) particularly in direction of the gap span. This was done to avoid edge coarseness relative to simulated dimensions. An illumination source, with desired frequency range, intensity distribution and size, was also added. The simulation volume was defined to be several (~3-4) times the largest wavelength simulated in size. To account for limited simulation volumes, compared to light propagation lengths, model boundaries were set to consist of perfectly matched layers (PML), with low interreflectivity. These ensure that electromagnetic fields decay at the outer model surfaces. Additionally, to increase calculation speeds not involving forces, where possible, symmetric (perpendicular to excitation polarization) and antisymmetric (parallel

to excitation polarization) boundary conditions were applied. Simulations were also assigned a cutoff for remaining energy in the model region (here 10^{-5}, for convergence).

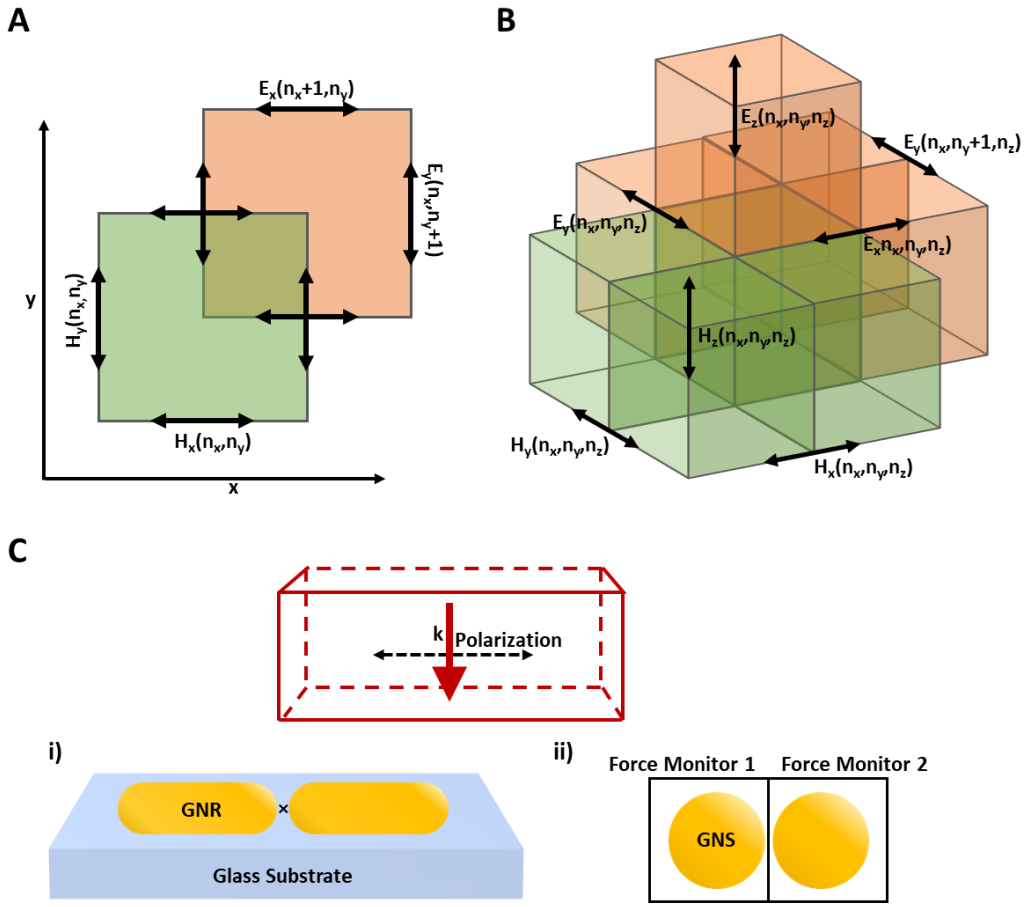

Figure 3.2.1: Finite-Difference Time-Domain Method. A Sketch illustrating Yee-cells in 2D. **B** Sketch illustrating Yee-cells in 3D. **C** Illustration of main plasmonic nanoantenna modelling. Injection occurred backwards in the z-axis, to best match excitation by laser. For studies on 40 nm spheroidal dimers from split GNRs on glass, light was injected from below the substrate. Field enhancement factors were normalized by corresponding illumination source field strengths at the hotspot centre height above the substrate. The hotspot centre is marked by × in **i**). Force monitors were applied so as to encompass individual dimer particles as depicted in **ii**).

What remains before running the simulation is adding rectangular monitors to determine different types of desired results. They are required to contain what they are to evaluate. This included scattering (σ_{scat}) and absorption (σ_{abs}) cross sections of the studied plasmonic antennas, as well as (mapped) electromagnetic fields, and volumetric forces. The first two aspects are calculated from energy absorbed within, and scattered out of cross section monitors respectively. Here, a self-subtracting light source cube (total-field scattered-field – TFSF) is implemented, so as to encompass the absorption monitor, and be encompassed by the scattering monitor. TFSF sources were also used to derive E-field maps from 2D electromagnetic field monitors, the most important result of FDTD within the scope of this thesis. Additionally, they were employed for evaluating optical forces. Where not stated otherwise, excitation was linearly polarized and aligned with the long axis of the antenna, for calculating corresponding field enhancement. To

achieve circularly polarized light, two perpendicularly polarized TFSF sources with a 90° phase difference could be employed. In such cases, symmetric and antisymmetric boundary conditions could not be implemented.

Calculated electromagnetic fields can also be used (by the software) to derive forces acting on surfaces of particles via the Maxwell stress tensor in **Equation 2.31**. This MST method functions by integrating (or effectively summing) over surface elements for **Equation 2.35**, with indices β for the different surface normals, with:

$$\boldsymbol{F} = \sum_{\beta} \oint_S \frac{1}{2} Re(\boldsymbol{T} \cdot \hat{\boldsymbol{n}}_{\beta}) dS, \tag{3.2}$$

for calculating total forces $\boldsymbol{F}$ acting on particles. It is best suited for larger particles with larger index contrasts, such as ~10+ nm gold nanoantennas, as examined here, and is based on field data at the surface. The volumetric technique on the other hand is based more directly on Lorentz forces and thereby **Equation 2.30**, via:

$$\boldsymbol{F}_v = \varepsilon_b (\boldsymbol{\nabla} \cdot \boldsymbol{E}) \boldsymbol{E} - i\omega(\varepsilon_r - \varepsilon_b) \boldsymbol{E} \times \boldsymbol{B}. \tag{3.3}$$

Here, ε_b is the background permittivity of the medium and ε_r is the background permittivity of the volume element. Whilst this method is more accurate for smaller particles with low contrasts of refractive index to the environment, it requires more memory, as it necessitates collecting fields throughout the volume. Its use is therefore limited to appropriate cases (here, approximated optical forces acting on proteins in **Section 4.2.2**).

Additionally, simulating of plasmonic heating power can be accomplished both for a whole particle, as well as spatially resolved, in dependence of illumination intensity. A simple approximation of heating power Q, with homogenous illumination intensity I is achieved by:

$$Q = \sigma_{abs} \cdot I. \tag{3.4}$$

From this an average heating power density q for volume of interest V can be calculated:

$$q = \frac{Q}{V}. \tag{3.5}$$

Heating with a Gaussian focus was modelled by implementing a (cross section) monitor for net power flow P_1 around a Gaussian source, and a second such monitor (analyzed for P_2) around source and antenna. Proportion of source power absorbed is then:

$$P_{prop.} = (P_1 - P_2)/P_1. \tag{3.6}$$

In principle, a more detailed volumetric heating analysis of $q(\boldsymbol{r})$ can be achieved by considering local fields together with local absorptivity. Here, $n^2 = \varepsilon \cdot \mu \simeq \varepsilon$ for non-magnetic materials (where $\mu \simeq 1$), and thus $Re(\varepsilon_\omega) = n^2 - k^2$ and $Im(\varepsilon_\omega) = 2n \cdot k$:

$$q(\boldsymbol{r}) = \frac{\omega}{2} Im(\varepsilon(\omega)) \left| E(\boldsymbol{r}) \right|^2. \quad (3.7)$$

This will also lead to significant anisotropies in heating (of gold nanoparticles) according to Baffou et al. [118]. Due to gold's significantly higher thermal conductivity (~318 $Wm^{-1}K^{-1}$) than that of water (~0.6 $Wm^{-1}K^{-1}$), temperatures are however relatively isotropic within the particles, particularly compared to their environment. In this work, nanoparticle heating is therefore approximated to be homogenous.

Calculations for spatially variable laser intensities were conducted for a Gaussian beam. In cylindrical coordinates, with propagation in the z axis and radial deviation r, intensity distributions are thus:

$$I(r,z) = I_0 \left(\frac{w_0}{w(z)}\right)^2 exp\left(\frac{-2r^2}{w(z)^2}\right). \quad (3.8)$$

For P_0 as the beams power, its intensity at its focal point is:

$$I_0 = \frac{2P_0}{\pi \cdot {w_0}^2}. \quad (3.9)$$

With beam waist radius at focus:

$$w_0 = \frac{\lambda}{\pi \cdot NA}, \quad (3.10)$$

beam waist radius for distance from focal plane z:

$$w(z) = w_0 \sqrt{1 + \left(\frac{z}{z_R}\right)^2}, \quad (3.11)$$

and the Rayleigh-Length:

$$z_R = \frac{\pi \cdot {w_0}^2 n}{\lambda}. \quad (3.12)$$

An additional important value in the scope of this thesis is the electric fields relationship with intensity, where c_0 is the speed of light in a vacuum:

$$I = \frac{c_0 \varepsilon_0 n}{2} E^2. \quad (3.13)$$

Combining **Equations 3.9** and **3.13**, electric field amplitude at the focal centre is:

$$E_0 = \frac{2}{w_0} \sqrt{\frac{P_0}{\pi n c_0 \varepsilon_0}}. \quad (3.14)$$

The main refractive indices used for modelling with FDTD in this thesis are based on work by Olmon et al. for monocrystalline gold [55], and Palik for glass and water [119]. Others were used as stated. Spheroidal particles were modelled as perfect spheres, and GNRs were modelled as cylindrical rods with hemispherical (if not stated otherwise) endcaps. Dimensions corresponded to manufacturing specifications and TEM imaging results of the samples studied in this work.

Where not stated otherwise, results were calculated and are depicted with 1 nm in spectral resolution.

3.2.2 Thermal Effects from Finite Element Analysis

Here, the Finite Element Method was used to calculate plasmonic heating effects. The versatile numerical technique [120], is based on boundary conditions surrounding a mesh. Mesh points are interlinked by differential equations representing relevant physical phenomena, with early implementations by Turner et al. [121], in 1956, in the context of aerofoil deflection. Parameters of these equations defined by structures and materials used for modelling, as well as boundary conditions. Triangular meshing of space into finite elements with contour equations C_{ij} [122] is illustrated in **Figure 3.2.2 A**.

Within the scope of this work temperatures T are examined, where the main differential relationship involved is represented by the heat equation:

$$q = \rho c_p \frac{\partial T}{\partial t} - \nabla \cdot (\kappa \nabla T). \tag{3.15}$$

Here ρ is the mediums density, c_p is its specific heat capacity and κ is the thermal conductivity. The latter parameter is most central to this work, where CW excitation is approximated to cause steady state heating, due to sub-nanosecond equilibration timescales (**Section 2.2.4**). Relevant parameters were implemented directly from the *COMSOL* materials database for gold, (quartz) glass, water and air.

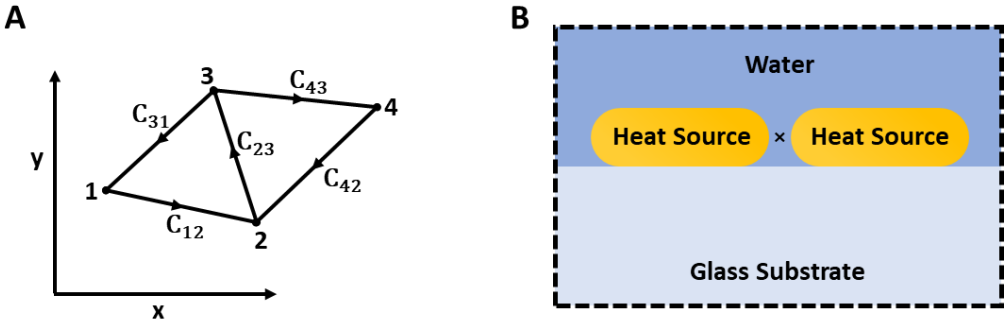

Figure 3.2.2: Finite Element Method. A 2D-Sketch illustrating meshing of boundary elements C_{ij}, between (numbered) points in space. **B** 2D-sketch (not to scale) illustrating modelling, including room temperature (20 °C) boundary conditions (dashed black outline). Gap temperatures are given for point ×. A is after reference [122].

The simulation volume was set to be 1 × 1 × 1 µm in size. Half of it consisting of water, and the other half of glass, as illustrated in **Figure 3.2.2 B**. Meshing was set to be extra fine and physics controlled in the software. The second aspect results in finer meshing around the interface between heat sources and surrounding media. Homogenous heating, with volumetric powers could then be applied to the GNR, and the simulation was run until a steady state equilibrium was

reached. Temperatures could then be read out from specific points, as well as exported in the form of 2D heatmaps.

4 Gold-Nanorod Dimers for Single-Molecule SERS from Solution

In recent years, several experimental approaches have been developed towards detecting single label free aqueous proteins. These have included interferometric scattering (iSCAT) microscopy [123], as well as localized surface plasmon interaction [124, 125], which both rely on a refractive index contrast between proteins and their environment. Ionic conductance measurements through nanopores [126], can also not resolve actual analyte chemical structure. These techniques therefore feature potential identification ambiguity. In contrast, Raman and infrared (IR) spectroscopy do deliver such information as they are based on molecular oscillations and lattice phonons. Whilst functional for the study of proteins [127], IR spectroscopy is however limited for biological samples due to absorption by water molecules at relevant wavelengths.

SERS therefore presents a tenable way for achieving this goal. It is however challenging if the nanoagent hotspots are to be readily accessible for diffusive analyte to bind in and be functional in the bio-optical window. Here this is aimed at via GNR dimers aligned in a tip-to-tip manner, using DNA origami.

This work builds on a notable series of previous studies, using DNA origami to structure plasmonic dimer Raman sensors. It starts with 40 nm gold nanospheres, coated with dye, and DNA strands [128] by Thacker et al., as well as quantified amounts of SYBR Gold dye molecules [129] by Kühler et al. reported on in 2014. This has continued to evolve into the detection of single Cyanine 3.5 (Cy3.5) dye molecules [38] by Simoncelli et al. (2016). Whilst the first example, provided an open albeit untested SERS hotspot in the DNA origami platform, the second and third featured a proven but sealed hotspot in a DNA origami sandwiching structure. Later studies by Tapio et al. focused on smaller single proteins such as horseradish peroxidase (HRP, 40 kDa) prefixed between two 60 nm plasmonic spheres, spaced by DNA nanoforks [40] (2021).

More accessible SERS hotspots present a key for practical measurements on diffusive analyte. Here, Zhan et al. employed gold bowties to generate open 5 nm large hotspots [42]. These were used for Cy3 and Cy5 molecules preattached to a DNA strand reaching into the plasmonic hot spot. Whilst appearing promising, their use for protein SERS from solution was not demonstrated. With respect to this goal, Tanwar & Sen et al.'s work on coupled plasmonic nanostars [130-132] culminated in the measurement of several dyes, as well as the protein thrombin [41] in 2021. The latter publication displayed a scheme for capturing thrombin from solution with an aptamer, between two Ag coated Au nanostars. However, whilst highlighting the importance of detecting

freely diffusive bio molecules, the demonstration of SM-SERS from hotspots was not conclusive. Further, these detection schemes were tested in air, disparate to potential in vivo applications. Additionally, the ≤ 633 nm laser wavelengths used are absorbed by tissue.

E-field enhancement of coupled GNR tips has been exploited successfully in previous studies. In particular, it has enabled fluorescence detection of diffusive [133] as well as preattached dyes [134], using sheet- and pillar-based DNA Origami scaffolds respectively. Additionally, chains of coupled GNRs have yielded protein SERS, albeit of larger amounts of p-ATP preattached and confined to intertip hotspots during antenna assembly [135].

In contrast, here, gold nanorod dimers are used for detecting single diffusive proteins. This chapter is based on: [136] (Schuknecht, Kolataj et al.). It begins with an outline of the GNR dimer design criteria, synthesis, and characterization in **Subchapter 4.1**. This is continued with demonstration and discussion of single-protein SERS, with analyte captured from solution in **Subchapter 4.2**. Finally, means of improving upon the GNR dimer system are discussed in **Subchapter 4.3**.

4.1 Gold-Nanorod Dimer Design and Properties

Beyond a principal of two gold nanorods aligned in a tip-to-tip fashion, other parameters need to be accounted for to achieve the goal of single protein SERS, with practical applicability. These begin with a sizable hotspot balanced against E-field enhancement. Regarding hotspot size, gaps should be wider than analyte molecules. Here, this is defined by the ~5 nm diameter of proteins streptavidin [137] (~60 kDa) and thrombin (~36 kDa), chosen for measurement due to their proximity to the mean weight of proteins in eukaryotic cells (49±48 kDA) [138]. Additionally, plasmonic coupling is strongest at smaller distances between metal nanoparticles. From a geometric perspective, GNR radii should therefore be significantly larger than the desired analyte, for it to experience significant field enhancement. Further, they should both be excited and emit Raman in the bio-optical window. For excitation with a 671 nm laser (as used here), in an aqueous environment, resonance should thus be around 1500 cm^{-1} lower in energy (located around 746 nm), to maximally enhance Raman cross sections of biomolecules [139]. Less maximized excitation enhancement can then be compensated for by higher laser powers. The design, implementation, and characterization of GNR dimers is discussed in the following sections.

4.1.1 Plasmonic Dimer Antenna Design

A first step for evaluating antenna designs for SERS, is assessing their electromagnetic enhancement. Here, this is done theoretically, using FDTD, to approximate experimental conditions. Calculations were conducted for bare 21 × 64 nm GNRs (aspect ratio of 3.05), in water, on glass. **Figure 4.1.1 A** indicates significant E-field enhancement factors of ~10^2 throughout GNR dimer hotspots for gaps of 10 nm. Additionally, these are achieved at a desirable wavelength range of the bio-optical window, for a range of gaps as shown in **Figure 4.1.1 B**.

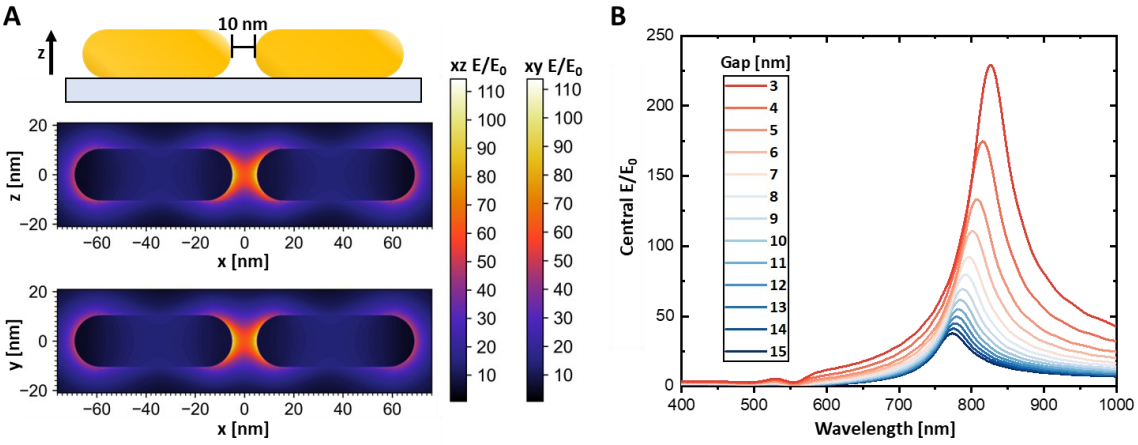

Figure 4.1.1: Wavelength dependent E-Field Enhancement. A E-field enhancement of GNR dimer with a 10 nm gap in water on glass, in both the xz- and xy-plane. Field enhancement scales are similar (~1% deviation). The calculation was done at 785 nm for maximum central E/E_0. **B** Wavelength dependent E-field enhancement at the hotspot centres of GNR dimers for different gap lengths.

Further, red-shifting of E-field enhancement for smaller distances between the GNRs and resulting increasing plasmon coupling [44], is limited to ~53 nm or ~830 cm^{-1}, for gaps from 3-15 nm. At the same time, line widths span ~80 nm or ~1300 cm^{-1}. This indicates Raman enhancement at suitable wavelengths over a broad range of gaps, with tolerances for differently sized analyte and variances in synthesis. A nanorod geometry with an aspect ratio of ~3 therefore appears suitable. It was aimed for in experimental synthesis, described in the following.

4.1.2 GNR Dimer Assembly with DNA Origami

To generate GNR dimer antennas for SERS, DNA origami is used here. In recent years, nanolithography has been augmented by DNA origami as a versatile method for bottom-up nanostructuring. It is based on deoxyribonucleic acid and its nucleobases adenine, thymine, guanine and cytosine (A, T, G and C respectively). These interlink covalently between sugar and phosphate groups, forming single strands with a sugar phosphate backbone. Additionally, A and T, as well as G and C form bonds between each other, joining the single strands into a double helix. This has been exploited with tailored DNA, where scaffold strands fold into complex three-dimensional shapes held in place by specific DNA staple strands [36, 37].

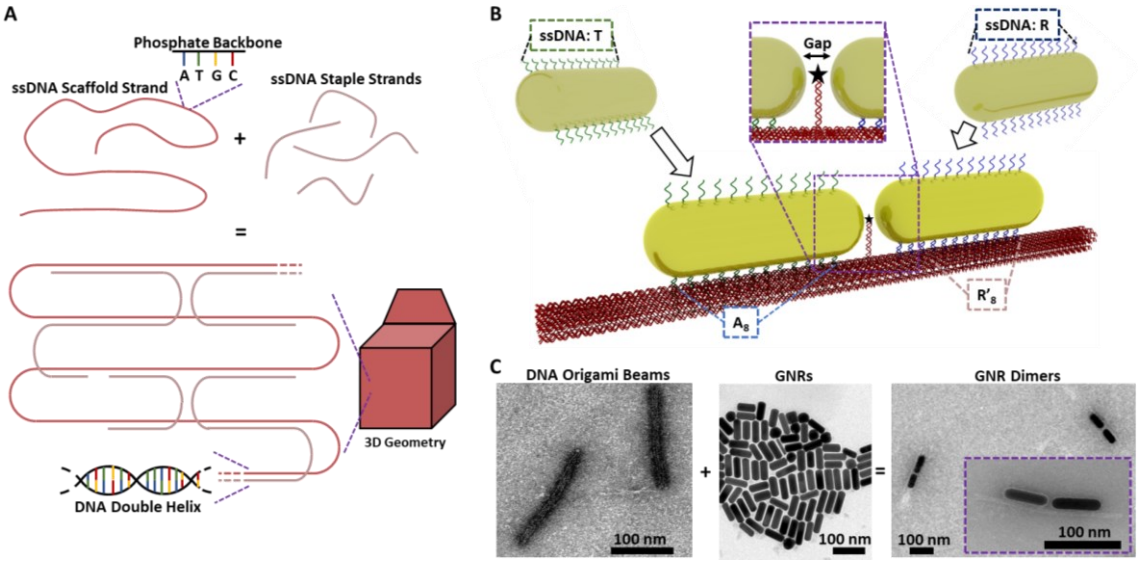

Figure 4.1.2: DNA Origami for GNR Dimers. A Illustration of DNA origami assembly. Here ssDNA scaffold strands with a fixed sequence are held in place with specifically matched ssDNA staple strands. **B** Illustration of GNR dimer assembly. DNA origami is folded into beams and used as scaffolding of GNRs, via A_8 and R'_8 binding sites. GNRs are functionalized with corresponding T or R sequence ssDNA, to bind to the scaffolding beam pairwise and longitudinally aligned, forming a gap at the centres of their tips. The beam is designed with a central docking site for SERS analyte (black star) at the intertip hotspot centre. **C** Exemplary TEM images of DNA origami beams, GNRs, and thereby assembled GNR dimers (with closeup insert). B and C have been adapted from: [136] (Schuknecht et al.).

The DNA Origami method is illustrated in **Figure 4.1.2 A**. Coupled with the ability to fit such structures with binding sites at defined locations, DNA origami can be used as scaffolding for

metallic nanoparticles coated with matching single-stranded DNA (ssDNA) linker strands via thiolate bonds [140, 141]. This has allowed for generating plasmonic hotspots for SERS in numerous works, not limited to the following: [38-42, 128-130, 142-147].

Here, for assembling GNRs in a tip-to-tip manner, with a SERS hotspot and analyte binding site between the two, a beam-based scaffolding was chosen. The corresponding design by K. Kolataj was implemented using *caDNAno* [148, 149]. It is based on DNA strands, as illustrated in **Figure 4.1.2 B**. The 14 strands were designed to assemble in a honeycomb lattice, resulting in a 215 × 12.5 nm superstructure. Each half of this structure was designed with 14 binding strands, with 4 nm separation, running along a single axis on the beams surface. The sites differed in the 8 nucleotide long binding strands employed, with one type being poly-A (AAAAAAAA), and the other being Random' (ATGTAGGT). These are meant to bind correspondingly functionalized GNRs whilst preventing single nanorods bridging across the beam centre. This is crucial as the space is designated for the inter-tip plasmonic hotspot.

To locate analyte and analyte binding sites in the SERS hotspot, two core strands at the centre of the beam, in line with the GNR binding sites, were elongated by 3 and 5 nucleotides. Dye molecules with 20 - and biotin as well as HD 22 aptamer with 5 – basis pairs were then able to dock to these sites, resulting in them being elevated by a double helix pillar. The pillar is devised to protrude from the GNR scaffolding beam in a perpendicular manner. This is facilitated by steric and electrostatic repulsion of the aqueous DNA phosphate backbone.

GNRs were synthesized by K. Kolataj according to protocols established by Ming et al. [29]. They were functionalized batchwise with thiolated ssDNA corresponding to the binding sites. At this point, the question arises to what extent DNA origami functionalization of synthesized GNRs might influence their plasmon response, by altering effective external permittivities. Raising these will result in red-shifts of the plasmon resonance (and vice-versa), analogously to the Fröhlich condition for metallic spheres (**Equation 2.23**). In-air studies on DNA origami based dimers by Thacker et al. [128], indicate that an ssDNA layer features a refractive index of 1.7±0.1, Submerging nanoparticles in (aqueous) buffer, led to limited red-shifts by 5±1 nm. Other, more explicit ellipsometry studies [128] have found refractive indices of ~1.46 for ss-, and ~1.53 for ds(double-stranded)DNA (dried, and at 700 nm wavelengths). Here, for an exemplary batch of GNRs in aqueous solution, functionalizing of the nanorods with thiolated ssDNA strands lead to limited resonance red-shifts from 680 to 682 nm (~2 nm). This indicates a limited influence of DNA on effective refractive index of the sample. It thus supports the simplified modelling of bare GNR dimers in water.

The GNRs were then added to a solution of DNA beams, to form GNR dimers. Finally, gel electrophoresis was employed for sorting out single nanorods and clusters, thereby purifying the

GNR dimer synthesis. An example for such antennas and their components is depicted in **Figure 4.1.2 C**. It confirms GNR dimer construction, with the goal of locating single analyte molecules in a hotspot and detecting them with SERS; the main subject of this chapter. Further details on the design and synthesis can be found in the supporting information and methods section of: [136] (Schuknecht, Kolataj et al.).

4.1.3 GNR Dimer Characterization

GNR dimers were synthesized in two different batches, R1 and R2, based on two sperate nanoparticle batches. They were then dropcast onto TEM grids and glass substrates for measurements. The nanoantennas were analyzed by TEM to confirm both dimer formation, as well as to examine their structural properties. **Figure 4.1.3 A** and **B** show further exemplary TEM images of synthesis results for the batches.

To verify that antennas featured correct specifications, GNRs constituting dimers were measured, with results depicted in **Figure 4.1.3 C**-**F**. These show that dimer GNRs fulfilled design criteria of aspect ratios ~3, with widths ~20 nm. Here, batch R1 matched the 64 × 21 nm dimers simulated best, with 2-3 nm deviations in average dimensions for batch 2. Further, analysis on the gap span is depicted in **Figure 4.1.3 G** and **H**. Gaps were ~8±3 nm in width, thus (usually) exceeding the size of streptavidin and thrombin. Besides spacing, another important degree of freedom exists in the sample generation outcome, namely the alignment of their GNRs towards one another. As can be seen in **Figure 4.1.3 I** and **J**, properly formed dimers (with maximum misalignment of 60°), featured a limited average angular deviation of 13°. Overall, a ~55% synthesis yield of tip-to-tip GNR dimers was achieved.

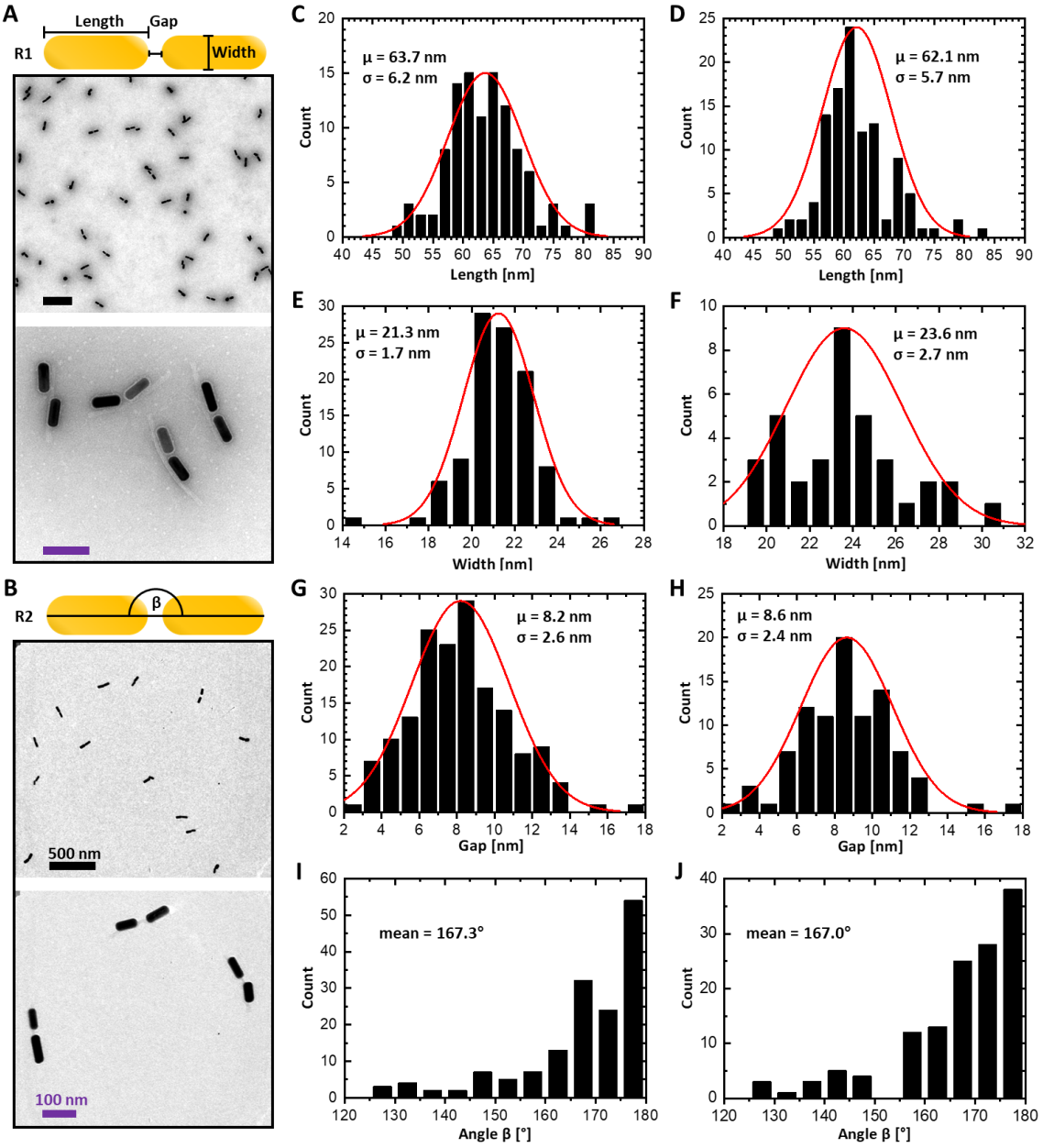

Figure 4.1.3: GNR dimer Geometry Characterization by TEM. A and **B** TEM images of R1 and R2 GNR dimers. Sketches illustrate length, width, gap and angle β of dimer Characterization. **C** Length distribution of batch R1 GNRs assembled into corresponding dimers by DNA origami. **D** Length distribution of R2 GNRs from corresponding dimers. **E** Width distribution of R1 GNRs. **F** Width distribution of R2 GNRs. **G** Gap size distribution of R1 GNR dimers. **H** Gap size distribution of R2 GNR dimers. **I** Inter-GNR angle distribution of R1 dimers. **J** Angle distribution of R2 dimers. Here 180° corresponds to an ideally (straightly) aligned dimer, and angles below 120° were not considered. Black scale bars denote 500 nm, and purple scale bars 100 nm. Red curves are Gaussian fits, with μ as a mean, and σ as a standard deviation. This figure has been adapted from: [136].

For further optical characterization experiments on dimers, these were dropcast onto glass substrates, and analysis commenced with DF-microscopy. Imaging results of this are depicted in **Figure 4.1.4 A**. Here, potential GNR dimers were identified by their reddish color. Dark-field illumination was then used for single antenna scattering spectroscopy with exemplary spectra depicted in **Figure 4.1.4 B**. Further analysis of dimer scattering spectra revealed a mean plasmon resonance of 753±26 nm. Here, GNR dimer shapes were determined using SEM, with examples

shown in **Figure 4.1.4 C**. It was found that out of 30 reddish spots examined spectroscopically, 16 stemmed from GNR dimers. Other antennas were malformed dimers, single GNRs or aggregates. This corresponds to an identification and targeting rate by DFM of 53%.

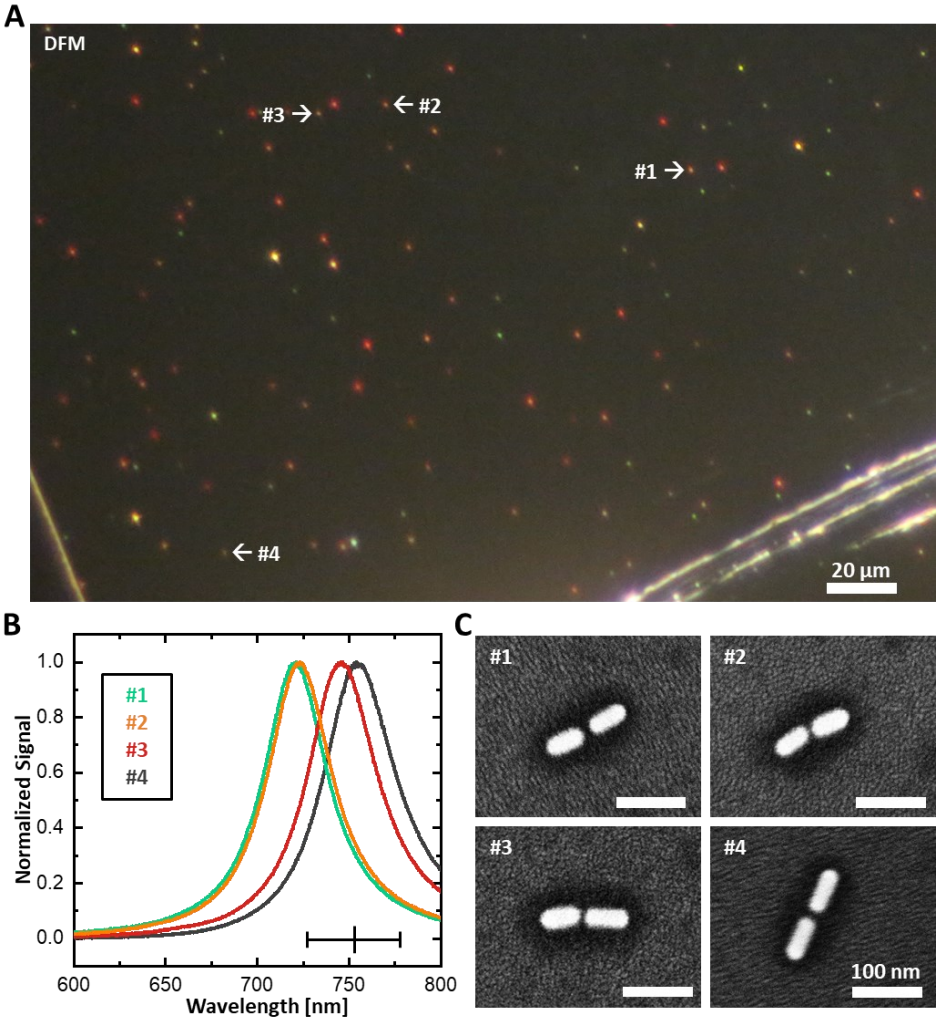

Figure 4.1.4: GNR Dimer optical and structural Confirmation. A DFM image of GNR dimers (reddish spots) on glass substrate in air. **B** Exemplary scattering spectra of GNR dimers in A. Here, for 16 dimers, a mean scattering peak position of 753±26 nm (indicated by black marker with error bars). **C** SEM images of GNR dimers in A and B. Overall 16/30 reddish spots from A examined were determined to be dimers. This figure has been adapted from: [136].

These spectral measurements were conducted in air, as blow-drying of samples after water immersion experiments appeared to remove a large proportion of GNR dimers from their sample substrates. Whilst higher effective external permittivities (in water) might cause plasmon red-shifts, spectroscopic results are nevertheless relevant for measurements in water. Here, Thacker et al. [128] found a lack of plasmon resonance shifts for single ssDNA coated gold nanospheres on flat DNA origami sheets. For corresponding dimers blue shifts were observed, due to increased spacing between nanospheres. This was linked to ssDNA hydration expanding dimer gaps. In this work on DNA-beam-based dimers however, ssDNA length is not directly responsible for the tip-to-tip spacing of GNRs. DFM experiments throughout this study indicated limited shifts in

antenna color from sample submersion in water. An example for a ~7 nm red-shifted spectrum is given in **Figure 4.1.5 A**. Conversely, the antenna spectrum in **Figure 4.1.5 B** features a ~11 nm blue-shift from aqueous submersion. Here, the antennas were not identified as dimers via SEM. However, the antenna in B (unlike that in A) was useful for Raman and is discussed later in this subchapter.

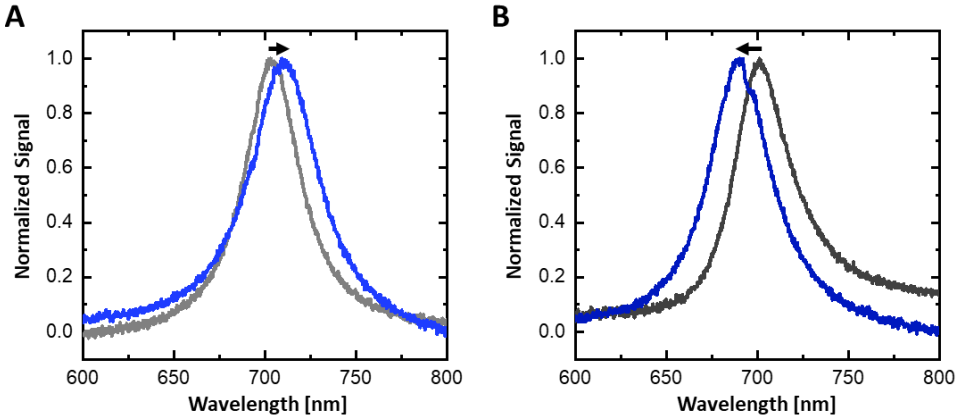

Figure 4.1.5: Examples of Environmental Effects on Nanoantenna Plasmon Resonance. A Scattering spectrum of nanoantenna in air (grey) and water (blue). The spectral peak red-shifted from ~703 to ~710 nm. **B** Scattering spectrum of a second nanoantenna in air (dark grey) and water (dark blue). The spectral peak blue-shifted from ~701 nm to ~690 nm. Spectra were first acquired in air, and then in aqueous solution. Black arrows indicating shifts are not to scale. The aqueous antenna scattering spectrum in B has been adapted from: [136].

At this point, it should also be noted that, whilst the resonance ~750 nm (in air) appears favorable for Raman measurements with a 671 nm laser, a selection bias for dimers with bluer resonances cannot be exclude. It can be expected to stem from particles with resonance wavelengths beyond ~800 nm being significantly more difficult to identify via the CMOS camera. (equipped with a conventional photography IR filter). More specifically, particles with resonances further in the NIR lack brightness. This might lead to selection for dimers featuring larger gaps, or consisting of GNRs with smaller aspect ratios, compared to the synthesis mean. In general however, synthesized GNR dimers identified for measuring fulfilled initially specified criteria, with resonances in the bio-optical window.

4.1.4 Impact of Laser Irradiation on GNR Dimers

Another significant factor to be considered, is modification of the dimer system itself, by laser irradiation. The most prominent factor here is plasmonic heating. Past reports of it have usually focused on plasmonic particles and their thermal reshaping. This has included surface diffusion, from tips of GNRs to their centres, by Link et al. [150], with a femto-second pulsed laser. Temperatures for such deformation of gold nanogeometries were found to be several 100 K under the bulk melting point of gold (~1337 K) both theoretically [151], as well as in experiments [152].

Whilst such temperatures (several 100 °C) are clearly to be avoided, significantly less extreme heating to 150 °C, has been found to shrink DNA origami sheets by ~50% [153]. Thus, in the context of DNA origami assembled plasmonic dimers, Simoncelli et al. [38] found that shrinking of a funnel like scaffold lead to reduced gaps between dimer spheres. This also led to increased SERS signal, from higher field enhancement, in air.

For this work, with a focus on aqueous SERS measurements, a heatsink effect of the environment can be assumed. This was approximated via numerical calculations, with results described in the following. Here temperatures, of and around the GNR dimers are significantly lower in water (**Figure 4.1.6 A**), than in air (**Figure 4.1.6 B**). This also translates to the GNRs themselves and hotspot centres, as displayed in **Figure 4.1.7 C** and **D** respectively, over a range of excitation powers.

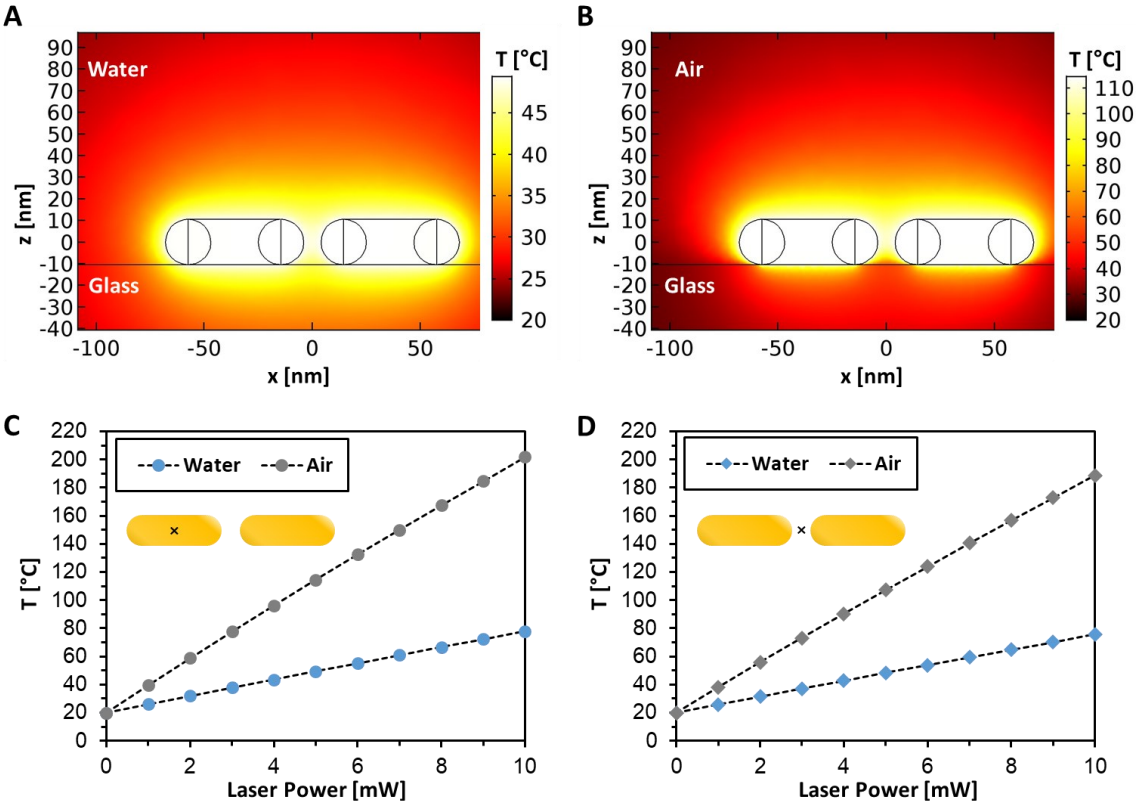

Figure 4.1.6: Heating Calculations for GNR Dimers in Air and Water. A Calculated temperature distribution around bare GNR dimers with 8 nm gaps in water. Heating was modelled assuming a power of 5 mW, for the 671 nm laser. **B** Temperature distribution around bare GNR dimers with 8 nm gaps in air, for heating power in A. **C** Temperatures of GNRs for different laser powers in water and air. **D** Temperatures at hotspot centres for different laser powers in water and air. Locations are indicated with: ×. The FEM calculations are based on 0.393% of parallelly polarized focused laser light absorption (derived via FDTD). This absorption quotient is halved to approximate circularly polarized excitation. A and C have been adapted from: [136].

These approximations predict that heating in water with several mW laser power should not impact DNA origami scaffolding significantly. It should however be remembered that differences in resonance from GNR dimension and gap sizes will impact absorption, thermal dissipation, and

thus temperatures depicted. Thus, lower laser powers appear desirable, and their potential effects might still be considerable.

To gain an understanding of the qualitive effects of heating, further experiments were performed. These were carried out in air, again, as sample submersion and subsequent blow-drying in aqueous solution was found to remove a significant proportion of dimers from the substrates. This would have both lowered sample size, as well as potentially introduced a selection bias for or against dimers altered by the laser. Exemplary results are depicted in **Figure 4.1.7 A**.

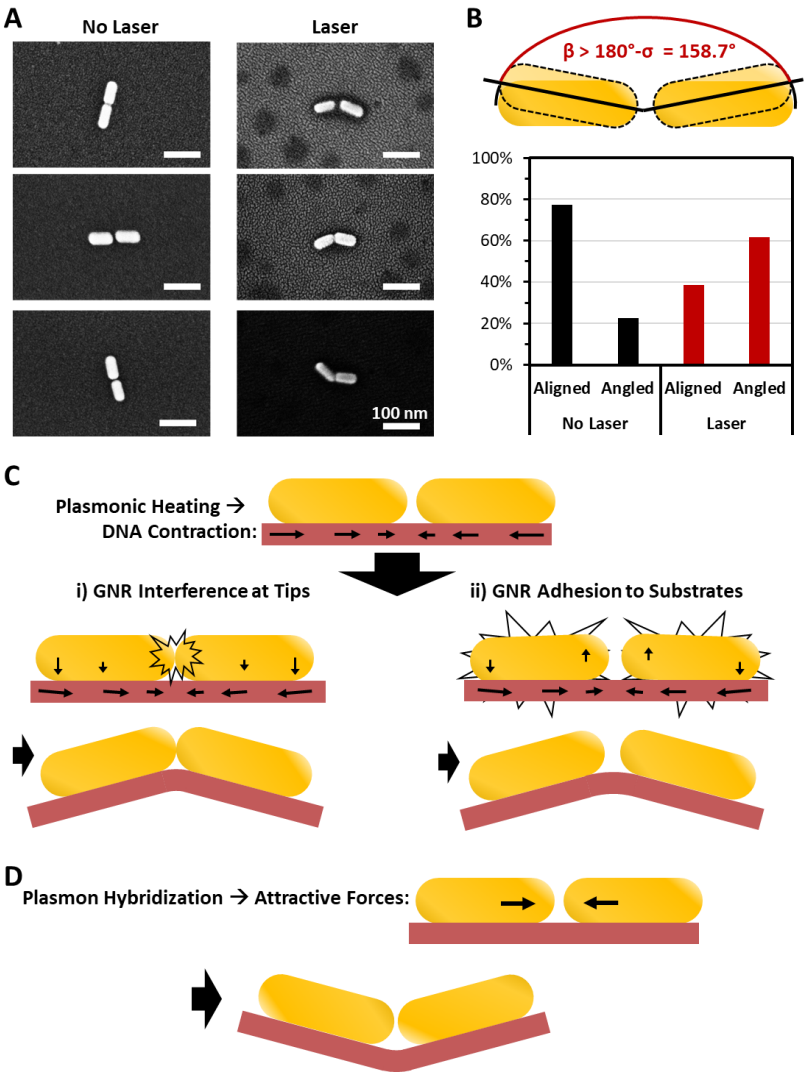

Figure 4.1.7: Angling of GNR Dimers under Laser Excitation. A SEM images of GNR dimers before and after laser irradiation and plasmonic heating. **B** Analysis of intradimer GNR (golden) angling from plasmonic heating. Here the non-heated GNRs were found to have a 21.3° standard deviation of angular misalignment, which functions as the threshold for being angled here. **C** Sketch of possible GNR dimer angling mechanisms, due to DNA beam (maroon colored) contraction from heating, either via **i**): GNRs colliding at their tips (leading to smaller gaps), or **ii**): GNRs sticking to the substrate (resulting in similar gaps). Corresponding interactions are signified by a star outline. **D** Sketch of possible GNR dimer angling due to electromagnetic forces (resulting in smaller gaps). Thin black arrows indicate force vectors.

Here it should be noted that DNA origami is not visible in the SEM images. Antennas were plasmonically heated using focused lasers, with wavelengths of 633 nm and 671 nm set to ~1-

10 mW of illumination power. These were directed at dimers on glass substrates for times on the order of 10s. The clearest visual difference found, between heated and nonheated antennas, was increased angling of irradiated dimer nanorods. Further statistical analysis confirmed an increase in angling, for particles exposed to a focused laser as shown in **Figure 4.1.7 B**. The probable cause of this, in the context of (aforementioned) previous work on heat shrunken DNA origami scaffolding [38], is contraction of the central DNA beam. With rods then either colliding with their tips or sticking to the substrate, the contracting beam can impart a torque on them. The torque is applied via the single sided GNR-beam attachment. Such potential mechanisms behind angling of dimer GNRs towards one another, is illustrated in **Figure 4.1.7 C**.

Attractive forces, from the bonding dipole-dipole coupling component of plasmon hybridization [90, 91], between the antenna GNRs might also shrink gaps. Such forces can be explained classically, via two parallelly aligned (plasmonic) dipoles experiencing coulomb attraction to one another. The effect could thereby also lead to angling, as shown in **Figure 4.1.7 D**. Torque would occur when the dimer GNRs are forced towards one another, under maintenance of the length of the DNA origami beam to which they are attached. The mechanism would apply quasi inversely to tip interference angling from DNA scaffold contraction.

Apart from GNR substrate adhesion mediated angling, these effects might thus include smaller gaps. These are indicated in SEM images (**Figure 4.1.7 A**) and could provide higher Raman enhancement at the expense of hotspot size. Determining gap lengths of the GNR dimers with nm accuracy using an SEM is however difficult. This is due to resolution limitations, as well as potential variances in metal sputtering layers (required for electrical sample conductivity). Angles were however clearly derivable from lines running in parallel to the long axes of the dimer GNRs outlines, unaltered in terms of direction by sputtering.

The effects of angling between GNRs on field enhancement, are less straight forward than shrinking gaps. Other work on fluorescence enhancement from GNR-based dimers indicates that both excitation and radiation enhancement (of fluorophores) in the hotspots does drop, albeit not substantially [134]. These structures featured relatively angularly misaligned GNRs, attached by the tips to a twin pillar DNA origami scaffold, with an average angle of 134°. The results were supported by calculations on E-field enhancement factors at the hotspot centres. Here, this is also found numerically for E-field enhancement at the centre and the whole of the antenna hotspot, which is depicted in **Figure 4.1.8 A** and **B** respectively.

This coincides with limited shifts in resonance with angling, as indicated by **Figure 4.1.8 C**. Plasmon coupling thus seems relatively unaffected by misalignment. It thereby supports that both inherent angling from the synthesis shown in **Section 4.1.3** as well as from deformation is not an issue with minor angling, and even beyond 30°. However, whilst calculated E-field enhancement

(and resonance wavelength) does not appear substantially reduced, even at 90°, extreme cases of misalignment should still be avoided. For one, the analyte binding strand might otherwise be dislocated from the hotspot, and they might become less accessible. Additionally, these results are reliant on the spherical endcap approximation employed for modelling GNRs. It simplifies (geometrically) defining gap widths by their spans, and similarizes hotspot shape under GNR angling. In reality, synthesized particle ends are expected to not have perfectly spherical curvatures, due to crystalline facets of gold [29]. This might impact plasmon coupling significantly, particularly from a loss of symmetry of the gap around its span due to angling.

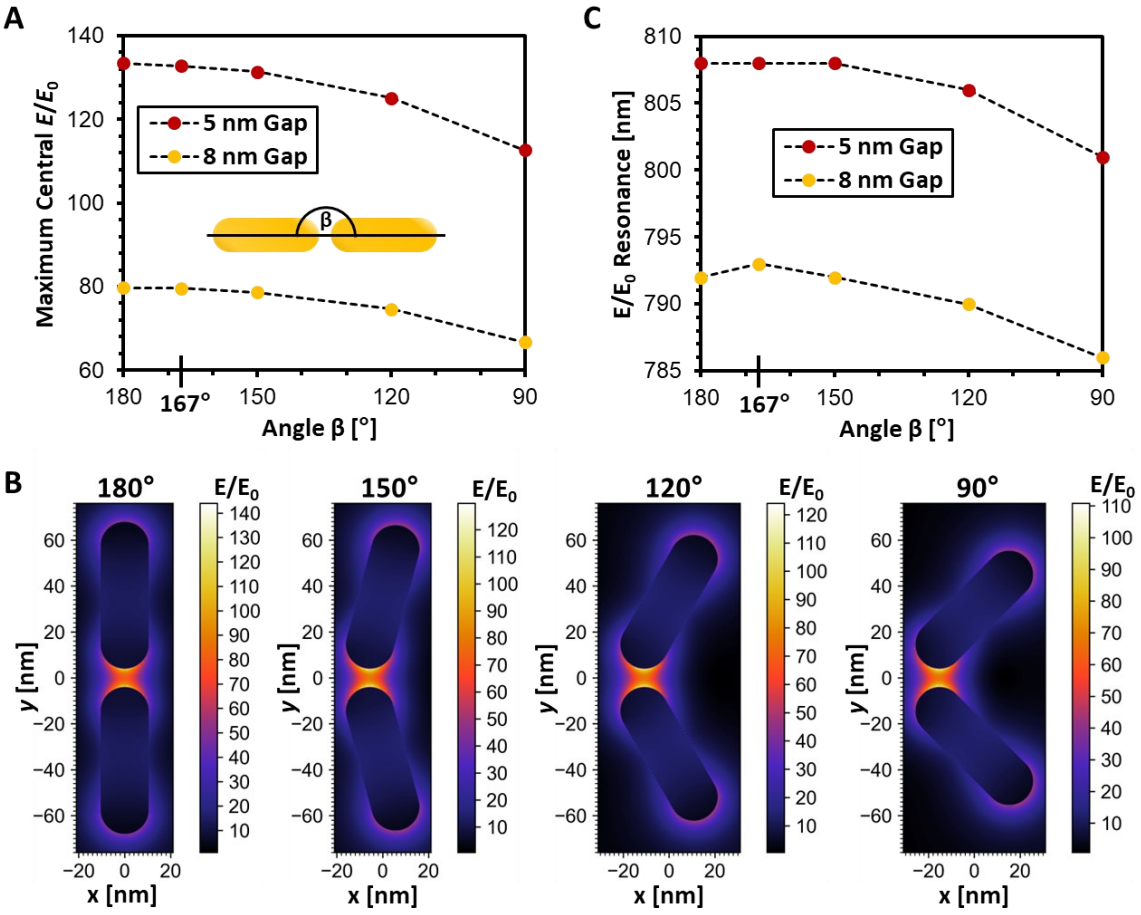

Figure 4.1.8: Angling Effects on E-Field Enhancement. A Dimer GNR angle β dependence field enhancement at the hotspot centre for 5 and 8 nm gaps. 167° represents the mean synthesis angle according to TEM. **B** E-field enhancement maps for GNR dimers with 8 nm gaps at different angles β on glass, in water. **C** Wavelengths corresponding to maximum calculated E-field enhancement in A and B. Gap lengths for angling are defined by the shortest distance between the GNRs. A and B have been adapted from: [136].

These findings indicate that SERS enhancement of GNR dimers might be relatively stable under laser excitation in aqueous solution. In particular, extreme cases, of melting GNRs appears avoidable at mW scale excitation powers. Impact on the DNA origami structure and GNR positioning should however still be considered.

4.1.5 SERS Detection of Cy3.5

To gain further insight, into GNR dimer function in practice, studies were carried out towards single dye molecule Raman detection. Dye molecules of the Cyanine family have been particularly prominent in past single-molecule SERS measurements [38-42, 147]. This has also been due to the ability of exciting dye resonance Raman, greatly increasing resulting Stokes shifted signal. Here, with Cyanine 3.5 molecules chosen as analyte the resonant enhancement is however not a strong contributor. This is due to a very limited overlap between the 671 nm laser line, and the dye's absorption spectrum, which peaks at 592 nm [154]. The molecule was instead chosen specifically to see whether and how SERS detection of small single molecules is achievable with the GNR dimers. It also serves for insight into how excitation by laser might impact the antennas during measurements.

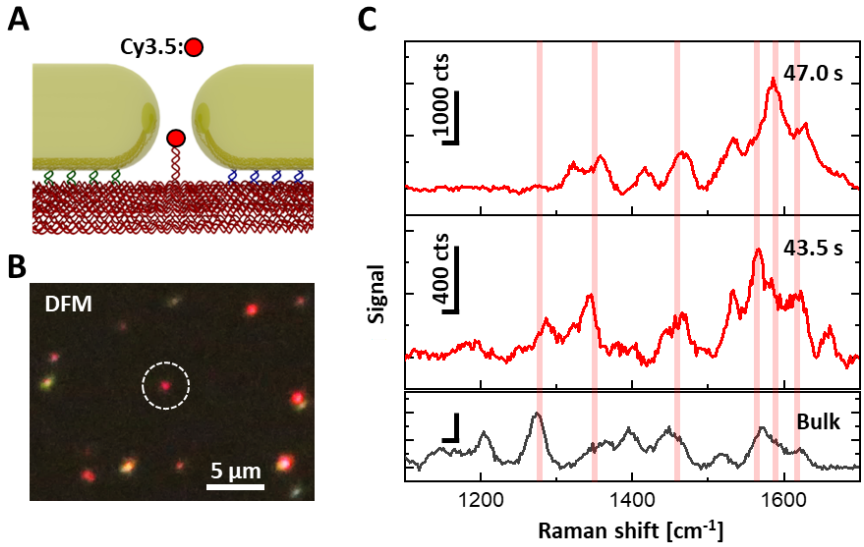

Figure 4.1.9: Single Cy3.5 Molecule SERS in Water. A Sketch of GNR dimer gap fitted with a Cy3.5 molecule. **B** DFM image of individual Cy3.5 fitted antennas on a glass substrate. **C** Single Cy3.5 SERS spectra with signal in counts (cts), from measurements at different times. The bulk spectrum (4000 cts scalebar) was acquired from Cy3.5, via a solution with 10 µM of dye concentration dried onto a gold film. The gold film was generated by sputter-coating a glass substrate. The spectra are background subtracted, for visual clarity. Raman peak assignment features in **Table 1**. This figure has been adapted from: [136].

GNR dimers for such experiments were synthesized with single Cy3.5 molecules, reaching into the inter tip hotspot via the central DNA helix pillar as illustrated in **Figure 4.1.9 A**. They were dropcast onto glass substrates. Samples could then be placed under a dark-field microscope, in water immersion conditions. Individual dimers were again identifiable, with an example (the same antenna as in **Figure 4.1.5 B**) depicted in **Figure 4.1.9 B**, to be targeted for SERS. Here a laser power of 10 mW was used to acquire Raman spectra in a sequential (time resolved) manner. Cy3.5 can in fact be identified clearly by SERS, as shown in **Figure 4.1.9 C**, for exemplary points in time of the measurement series. This is possible via distinct Raman vibrational modes, at 1270-1280 cm^{-1} (aromatic group motion) [155, 156], ~1350 cm^{-1} (central methine chain) [155-157],

~1460-70 cm^{-1} (asymmetric CH_3 deformation) [155-157], 1560 and 1590 cm^{-1} (N^+=C stretching) [155, 156, 158] and ~1610-1620 cm^{-1} (C=C stretching) [156, 158]. Signal corresponding to these peaks was also identifiable in bulk SERS measurements of the dye, confirming the single-molecule SERS capability of the design.

Table 1: Cy3.5 Raman Peak Assignment.

Cy3.5 Peak Positions [cm^{-1}]	Raman Peak Assignment
1270-1280	Aromatic group motion [155, 156]
1350	Central methine chain motion [155-157]
1460-70	CH_3 asymmetric deformation [155-157]
1560 and 1590	N^+=C stretching [155, 156, 158]
1610-1620	C=C stretching [156, 158]

The full corresponding time resolved SERS measurement of the antenna is shown in **Figure 4.1.10 A**. It reveals a significant amount of Stokes shifted signal at lower wavenumbers, with a lack of clearly identifiable molecular vibrational peaks. This shifted to fluctuating Raman signal at higher wavenumbers towards the end of the measurement. It is also where distinct Cy3.5 Raman spectra were identified. Such signal peak effects are common in single-molecule measurements [18, 159], where Raman fluctuations might stem from interactions of molecules with one another and with the SERS substrate. Here this might include ssDNA coating of the GNRs, as well as the dye analyte.

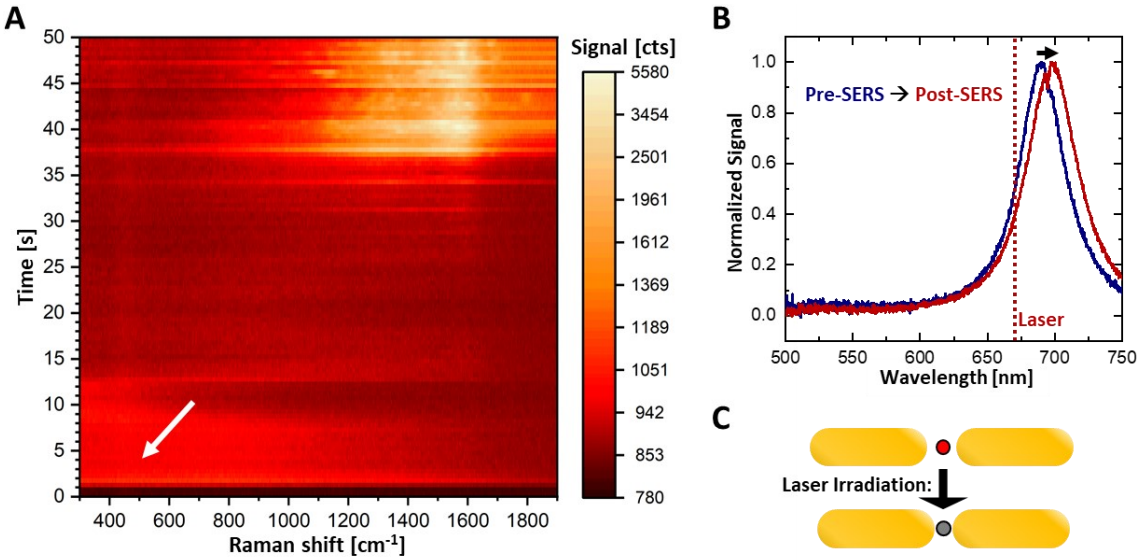

Figure 4.1.10: Effect of SERS Measurement on GNR Alignment. A Heatmap of signal from SERS measurement (serial acquisition), with 0.5s integration time per row. The laser was turned on ~1s into the acquisition, so as not to miss any signal. The scale is reciprocal, for visual clarity. The white arrow indicates an area of potential fluorescence signal. **B** Dark-field scattering spectra before (peak at ~690 nm, in blue) and after (peak at ~698 nm, in red) Raman measurement. The dotted line indicates the laser wavelength. **C** Sketch illustrating shrunken GNR dimer gaps (neglecting potential angling) with fluorescence quenching of dye molecule (red to grey). A and B have been adapted from: [136].

Besides fluctuant Raman signal, three other noteworthy findings stand out in the case of this SERS measurement. Firstly, it took several tens of seconds for significant Raman signal around 1400 cm^{-1} to appear. Secondly, the beginning of the measurement appears to be dominated by a low intensity fluorescence tail at lower wavenumbers, with signal disappearing towards later parts of the time series. Thirdly, there is a small red-shift in the dimer's scattering spectrum by ~8 nm, which is depicted in **Figure 4.1.10 B**. Combining points one and three clearly indicates that the intertip gap of the GNR dimer shrunk during the measurement, a possibility discussed in **Section 4.1.4**. It can explain the appearance of Cy3.5 Raman modes later in the measurement, via shrinking gaps coinciding with higher field enhancement in the hotspot. It also matches the spectral red-shift of the plasmon bonding mode peak from stronger coupling between the two GNRs. Notably, the second less intuitive point, a loss of fluorescence signal (at lower wavenumbers) might also be explained by a shrunken gap, instead of by simple fluorophore bleaching. This is illustrated in **Figure 4.1.10 C** and described in the following.

Whilst the laser line appears far outside of the absorption band of Cy3.5 [154], some minor fluorescence signal cannot be entirely excluded. Particularly, as plasmonic dimers, including specimens based on GNRs [160], have proven to be highly effective for raising fluorescence cross sections. Its disappearance, in conjunction with SERS of the dye molecule and indicators of a shrinking gap, therefore, points towards fluorescence quenching instead of potential fluorophore destruction.

This fluorescence quenching phenomenon from a proximity of molecules to a metallic surface has been reported by Dulkeith et al. [161], in the context of gold nanospheres. For Cy5 dye, the distance dependent effect, theorized to stem from a phase difference between the gold nanoparticle and the molecular dipole, was particularly pronounced around ~4 nm in experiments [162]. This distance corresponds to half of the average GNR dimer hotspot length. A shrinking gap can thus explain all three observed phenomena. It might also increase interaction between GNR surfaces and the dye, as well as ssDNA coating, leading to signal fluctuations. At the same time, potential angling occurring here, does not appear detrimental to SERS and thus E-field enhancement experimentally.

Whilst the detection of Cy3.5 was successful, previously described sample alterations do however represent a form of degradation. This regarding, another effect can also come into play. It is carbonization of the antenna's surroundings, which can be particularly prominent in SM-SERS measurements, as reported by Andreas Otto, in a 2002 review study [163]. Here, crosslinking of chemical groups, can lead to layers of amorphous carbon on the plasmonic surfaces. It was also found to contribute significantly to signal fluctuations. Whilst the study dealt with results at silver nanoparticles and rough silver films, chemical alterations at the metallic surfaces were found explicitly for biomolecules such as hemoglobin. Examining the effect is

therefore important in the context of this work. Carbonization has been found to stem from both heating (by several 100 K), as well as hot-electron-induced photochemical processes at plasmonic hotspots during TERS [164]. This sample degradation manifested in fluctuating signal, around 1350 cm^{-1} and 1580 cm^{-1}, leading to the emergence two broad humps dominating time averaged SERS spectra, at those locations. As an example in the context of dimers, hot electrons have also been effective at driving chemical reactions at the hotspots of silver nanotriangle bowties [106].

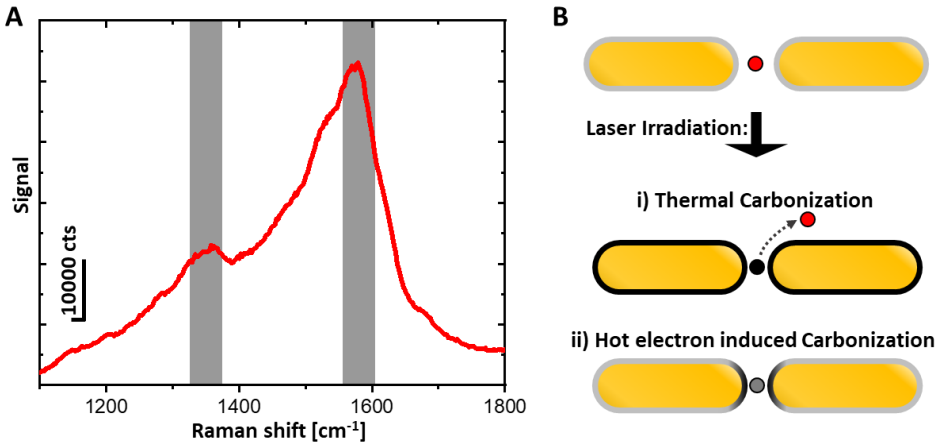

Figure 4.1.11: Cy3.5 Antenna Carbonization. A SERS spectrum of antenna with 20s integration time. The spectrum features broad peaks at 1350 and 1580 cm^{-1} (locations indicated by dark grey bars). **B** Illustration of potential mechanisms behinds behind carbonization. Here gaps shrink, and either: **i**) the whole of the antenna surroundings is thermally carbonized, including the Cy3.5 analyte unless it dissociates beforehand (dark grey dotted arrow). Or: **ii**) only ssDNA (at the hotspot) is carbonized. Here, ssDNA is light grey, carbonized media is (full) black, unquenched Cy3.5 is red and quenched Cy3.5 is colored dark grey. The sketch is not to scale, and potential angling is not depicted.

For the Cy3.5 measurement here, Raman indicative of carbonization was in fact observed, by integrating over the last 20s of the measurement, as depicted in **Figure 4.1.11 A**. It should be noted that this signal can be expected to also stem from Cy3.5. However, the two peaks appear broader and significantly more pronounced than for signal matching Cy3.5 (**Figure 4.1.9 C**). Carbonization for GNR dimers will therefore be examined in the following.

Here, hot electrons, as a cause for carbonization appear inhibited by a favorable combination of gold surface and aqueous environment. Regarding the first aspect, Heck et al. found gold to be significantly less effective for carbonization at its surface than silver [145]. For one, this was explained with a higher affinity of silver to oxygen [165] and anions [166] in aqueous solution. Additionally, it was attributed to thiol-bonding, of ssDNA coating, being stronger on gold than silver [167]. Desorbed radicals in turn can form further amorphous carbon products [164]. Regarding the second aspect, Bjerneld et al. found that for SERS measurements with silver particles, an aqueous environment suppresses carbonization [168]. Submersion in water was found completely protective for analyte shielded from direct contact with the metal nanoparticle surfaces by (thiophenol) adsorbate. The aqueous adsorbate itself was also less prone to carbonization in water than in air. The combination of gold nanoparticles in water might therefore

be expected to protect analyte completely, but not the ssDNA attached to the GNRs. Further, thermal aspects might also have played a role in carbonization. Potential mechanisms behind the measured carbonization signal are illustrated in **Figure 4.1.11 B**.

Calculations of model GNR dimers in water (**Figure 4.1.6 C**) indicate temperatures of ~76 °C here, indicating a lack of thermal carbonization. However, individual dimers might exhibit significant differences in absorption of the laser. In particular, the scattering peak of this antenna, is close (~19 nm away) to the excitation wavelength at the beginning of the SERS measurement (**Figure 4.1.10 B**). The laser induced plasmon (scattering) resonance red-shift (to a ~27 nm distance) could then have lowered plasmonic heating and temperatures. This in turn might have arrested thermal alteration, thereby preventing destruction of the antenna, as indicated by the limited plasmon resonance shift. That heating to the point of thermal carbonization was not involved matches that the single Cy3.5 DNA anchor strand did not dissociate thermally [169] prior to measuring dye SERS. Additionally, the molecule did also not appear chemically altered (in a significant way), as indicated by the clear Raman identifiability. More moderate temperature increases could however still have favored desorption and carbonization of thiolated ssDNA directly at the GNR surfaces. Detected (potential) carbonization Raman signal therefore appears to stem from hot electrons effecting ssDNA, and not analyte.

These findings highlight the importance of reduced laser powers for antenna and analyte preservation. Especially, as Raman fluctuations due to DNA carbonization might obscure analyte signal. They also indicate that some slight deformation might be favorable for electromagnetic enhancement factors, particularly for (initially) larger GNR dimer gaps. Elevated laser powers might thus also be desirable for SERS beyond a simple proportional increase in Raman excitation. Protein measurements in the following subchapter were conducted with a view towards balancing these aspects.

4.2 GNR Dimers for Single-Protein SERS

This subchapter begins with testing the GNR dimers for SERS of single proteins captured from aqueous solution, the main goal and topic of this work. Mainly, these were streptavidin (*SKU 189730* and *S4762*) from streptomyces avidinii bacteria and thrombin (*SKU 1.12374*) from bovine plasma. Additional proteins used for testing were myoglobin (*SKU M0630*) from horse skeletal muscle and IgG (anti-biotin antibody, *SKU B3640*) from goat. Proteins were purchased from *Sigma-Aldrich*. The subchapter is concluded with a discussion of the results, both in the context of E-field enhancement as well as measuring specificity.

4.2.1 SERS Detection of Proteins

Streptavidin and thrombin were not only chosen for testing GNR dimer capabilities due to their size and prominence. The ability to design effective binding sites for them at hotspots also factored into the decision.

Starting with streptavidin, the tetrameric protein has a size of 4.2 × 4.2 × 5.6 nm [137, 170], with a hydrodynamic radius of 2.82 nm [171]. It is prominent in biotechnical use and research due to its strong bond to the vitamin biotin. This takes place via one of its four avidin groups/binding sites [172]. Accordingly, GNR dimer antennas were constructed, with single biotin binding sites, so as to capture single streptavidin molecules in their gaps for SERS.

Testing of the streptavidin detection scheme commenced with identifying antennas, dropcast onto glass substrates, using DF-microscopy. This is visualized in **Figure 4.2.1 A**, together with the dimer design. Followingly, SERS measurements of individual prospective dimers were carried out in TE buffer, so as to test for the presence of biotin in hotspots. The measurements were carried out with a laser power of 5 mW. They also served to find potential background signal from DNA. Exemplary results of these SERS experiments are depicted in **Figure 4.2.1 B**. The measurement features its most prominent signal at ~1375 cm^{-1}, consistent with nucleobases of DNA (ring breathing modes of A, T, G) [139, 173]. Raman scattering corresponding to biotin was less distinct, but clearly visible. In particular in the form of signal at 1270 cm^{-1} assignable to methylene group wagging [174, 175], 1450-1470 cm^{-1} to CH_2 (ring) stretching [174, 175], and at 1565 cm^{-1} to C-N stretching [174, 176].

The next step was adding streptavidin to the TE buffer immersed sample. An illustration of the protein binding in dimer gaps is shown in **Figure 4.2.1 C**. After several minutes of waiting for the proteins to locate in hotspots and bind to biotinylated docking sites, measurements of commenced. Exemplary SERS results are shown in **Figure 4.2.1 D**. Here additional peaks were identifiable and assignable to streptavidin, with Stokes shifts at 1239 cm^{-1} (amide III/β-sheet)

[139, 174, 175, 177], 1336 cm^{-1} (tryptophan W7) [174, 175, 177], 1560-1580 cm^{-1} (tryptophan W2) [174, 177] and 1670 cm^{-1} (amide I/β-sheet) [139, 174, 177]. In the depicted measurement, most of these peaks were not present from the beginning of the acquisition. Further signal at ~1360-1370 cm^{-1} might correspond to tryptophan [174, 175, 177], as well as DNA ring breathing [139, 173]. An additional peak at ~1503 cm^{-1}, unspecific to streptavidin, can be assigned to aromatic ring vibrations of DNA [175] as well as N-H bending [139].

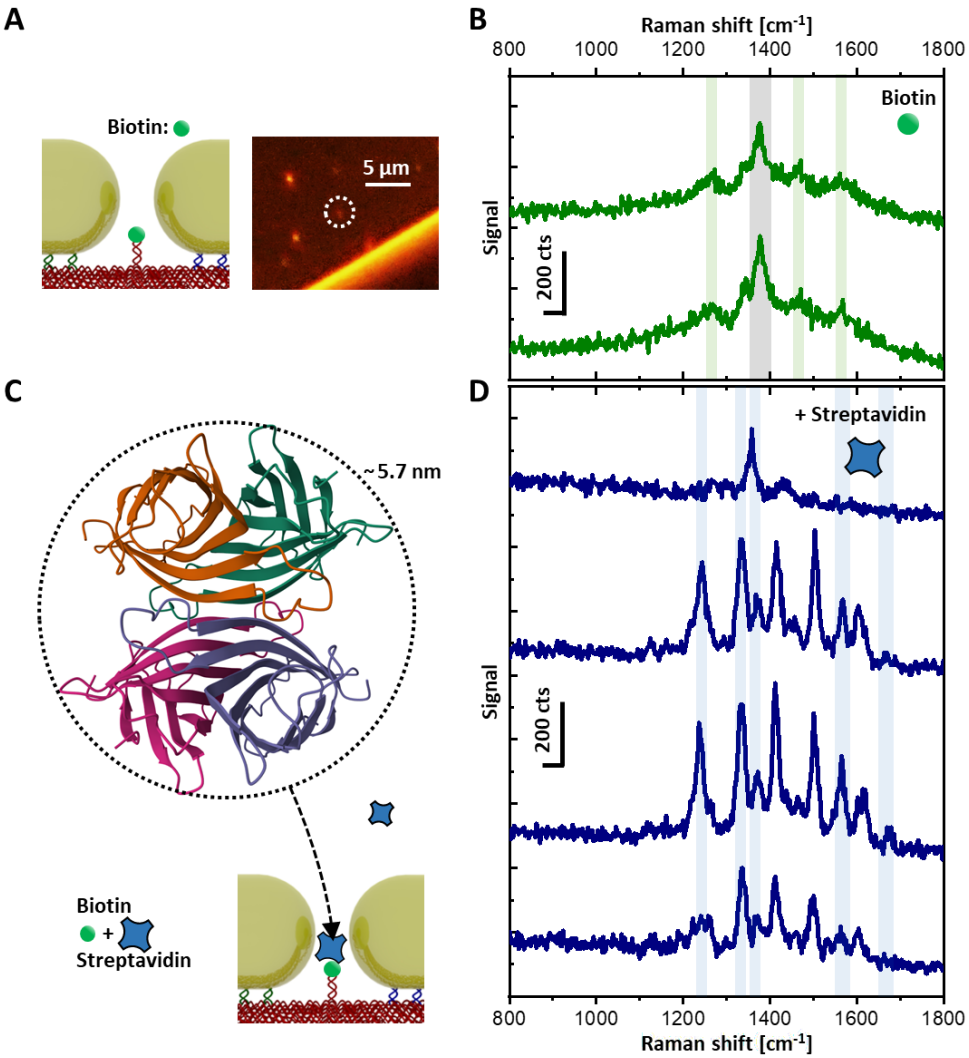

Figure 4.2.1: Streptavidin SERS in aqueous Solution. A Sketch of a GNR dimer gap with biotin binding site, and DFM image of antennas**. B** SERS spectra of biotinylated antenna circled in DFM image in A (with biotin Raman peaks highlighted in mint green, and DNA signal highlighted in light grey). **C** 3D rendering of streptavidin (circled) from data of [178], without ligand and water molecules. Image from the RCSB PDB (**RCSB.org**) of PDB ID 6J6J ([178]). The sketch illustrates streptavidin entering the antenna gap and binding to biotin. **D** SERS spectra measured after streptavidin was added to the solution. The first spectrum (from the top) does not enable the identification of streptavidin. Later spectra feature peaks assignable to the protein (highlighted in light blue). Streptavidin was concentrated at ~4.2 µM. All spectra were obtained with 0.5s integration times, with later SERS spectra at lower positions in their respective stacks, and with Raman peak assignment featured in **Table 2**. This figure has been adapted from: [136].

Here streptavidin was not detectable at the beginning of the measurement. This indicates that the protein was either not located in the hotspot, or that the hotspot was not sufficient in strength at the beginning of the time series. Particularly a shrinking gap could have furthered Raman enhancement.

Table 2: Protein Capture Raman Peak Assignment.

HD22/DNA Peaks [cm^{-1}]	**Raman Peak Assignment**
1160-1170	C and G [139, 173]
1230	Antisymmetric phosphate stretching [139, 179]
1375	T, A and G ring breathing modes [139, 173]
1510-1515	Adenine ring breathing [139, 180] and cytosine [139, 181]
1574	G and A [139, 173]
1601	Thymine [173]
Biotin Peaks [cm^{-1}]	**Raman Peak Assignment**
1270	Methylene group wagging [174, 175]
1450-1470	Stretching of ring CH_2 [174, 175]
1565	C-N stretching [174, 176]
Streptavidin Peaks [cm^{-1}]	**Raman Peak Assignment**
1239	Amide III/β-sheet [139, 174, 175, 177]
1336	Tryptophan W7 [174, 175, 177]
~1360-1370	Tryptophan [174, 175, 177], DNA ring breathing [139, 173]
1560-1580	Tryptophan W2 [174, 177]
1670	Amide I/β-sheet [139, 174, 177]
Thrombin Peaks [cm^{-1}]	**Raman Peak Assignment**
1230-1250	Amide III/β-sheet [139, 182]
1302	Amide III [139, 180] or CH_2 twisting for protein [139, 183]
1340 and 1360	Tryptophan [139, 182]
~1550-1560	Amide II or tryptophan [139, 182]
1639-1670	Amide I/β-sheet [139, 182, 184]

Additional measurements with the goal of detecting single thrombin protein SERS were carried out with similar GNR dimers in PBS buffer. The globularly shaped enzyme is well known for its role in blood coagulation. Whilst it is slightly smaller than streptavidin with a hydrodynamic radius of 2.05 nm [185], and (dry) dimensions of 4.5 × 4.5 × 5 nm [186], it serves to illustrate the antennas versatility. Here the antenna design involves central HD22 binding sites. These aptamers consist of 29 nucleotides forming a duplex/G-quadruplex mixed structure with a cage like geometry for capturing thrombin. The antenna design is visualized in **Figure 4.2.2 A**, together with a DFM image of located antennas. Due to the nature of HD22, the molecule cannot clearly be distinguished from the DNA origami scaffold by SERS measurement of corresponding antennas. An example is shown in **Figure 4.2.2 B**, measured with a laser power of 2 mW. Here, Raman modes typical for DNA were observed at ~1160-1170 cm^{-1} (C, G) [139, 173], 1375 cm^{-1} (T, A and G ring breathing) [139, 173], 1510-1515 cm^{-1} (adenine ring breathing and cytosine) [139, 180, 181] and 1574 cm^{-1} (G, A) [139, 173]. Further, signal at 1600 cm^{-1} is assignable to

thymine [173]. Finally, signal corresponding to antisymmetric phosphate stretching at 1230 cm^{-1} is assignable to DNA origami, ssDNA, as well as the aptamer [139, 179].

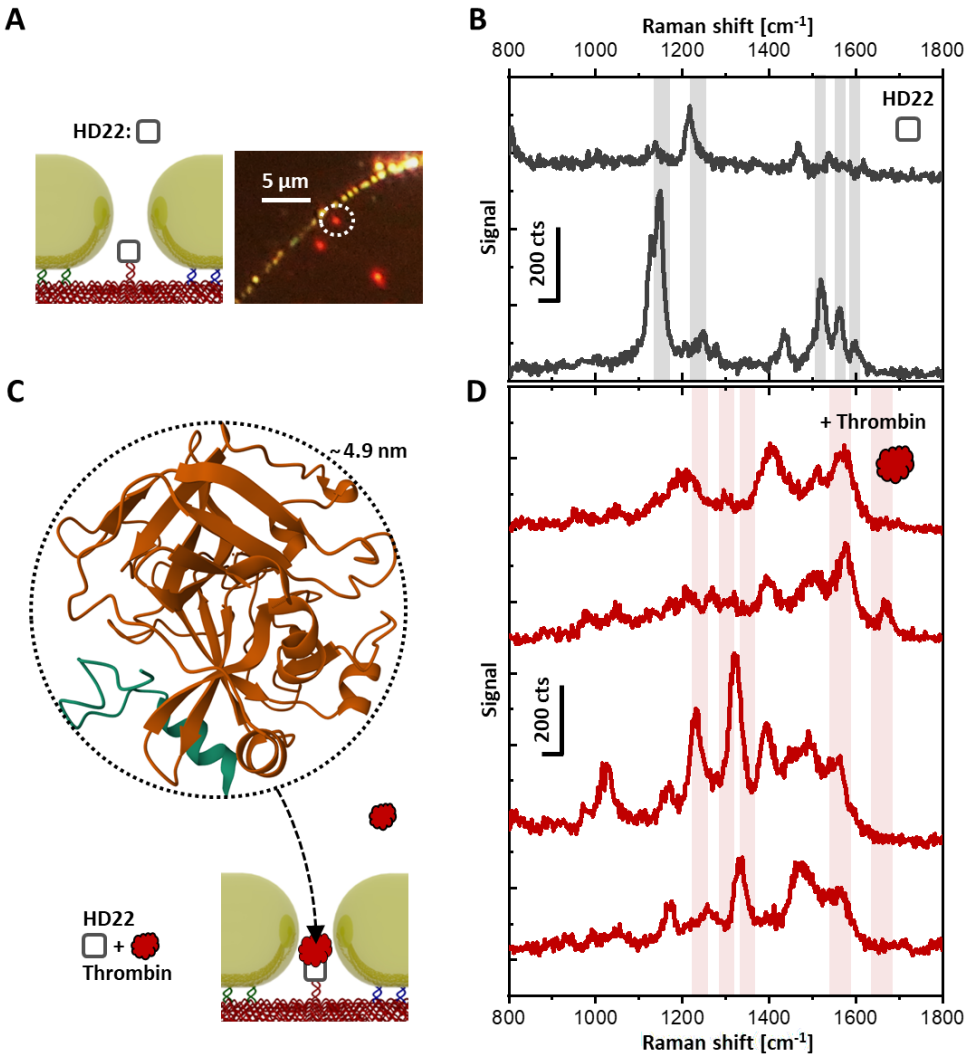

Figure 4.2.2: Thrombin SERS in aqueous Solution. A Sketch illustrating a GNR dimer gap with an HD22 binding site, as well as DFM image of such antennas. **B** SERS spectrum (from antenna circled in A) of the aptamer (with DNA/HD22 peaks highlighted in light grey). **C** 3D rendering of thrombin (circled) from data of [187], without ligand and water molecules. Image from the RCSB PDB (**RCSB.org**) of PDB ID 1UVT ([187]). The sketch illustrates thrombin entering the nanogap and binding to HD22. **D** SERS spectra after adding thrombin – for a concentration of ~28 µM (with thrombin peaks highlighted in light red). All spectra were obtained with 0.5s integration times, with later SERS spectra at lower positions in their respective stacks, and Raman peak assignment featured in **Table 2**. This figure has been adapted from: [136].

The next step consisted of adding thrombin to the solution. An illustration of the protein binding in hotspots is shown in **Figure 4.2.2 C**. After incubation, SERS measurements yielded signal depicted in **Figure 4.2.2 D**. This corresponded to thrombin at 1230-1250 cm^{-1} from amide III/β-sheet [139, 182], 1340 (and 1360) cm^{-1} (tryptophan) [139, 182], and ~1550-60 cm^{-1} from amide II and/or tryptophan [139, 182]. Signal at 1302 cm^{-1} is assignable to Amide III as well as protein CH_2 twisting [139, 180, 183]. Intriguingly, amide I/β-sheet Raman was not consistently

visible via signal between 1639-70 cm^{-1} [139, 182, 184]. Together with signal fluctuations this points towards degradation of the sample, as well as potential carbonization.

To examine the effect of carbonization, protein measurement signal was integrated, for results from the streptavidin as well as thrombin measurements displayed in **Figure 4.2.1 D** and **Figure 4.2.2 D** respectively. This is depicted in **Figure 4.2.3 A** for streptavidin, and **Figure 4.2.3 B** for thrombin. Both spectra indicate a lack of carbonization humps, with sharper protein peaks remaining visible at and around wavenumbers of relevance.

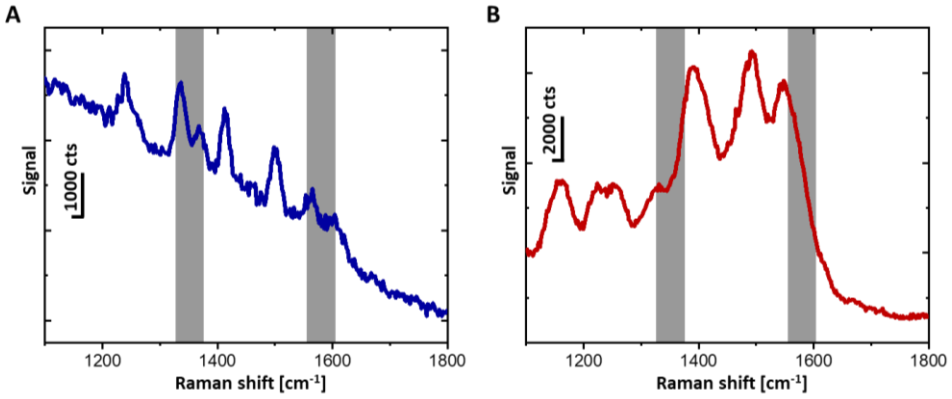

Figure 4.2.3: Protein SERS with longer Integration Times. A SERS spectrum of streptavidin measured with 5 mW. **B** SERS spectrum of Thrombin measured with 2 mW laser power. Overall integration times were 30 seconds for both spectra. These lack broad peaks at 1350 and 1580 cm^{-1} (locations indicated by dark grey bars). This figure has been adapted from: [136].

The finding indicates that both heating as well as hot electrons are, at the very least, not a detrimental issue for these GNR dimer measurements. The thermal aspect is consistent with results for plasmonic heating (**Figure 4.1.6**) where GNR temperatures lie at ~49°C even for 5 mW of excitation power. At these temperatures, protein denaturation can however still be a factor, even in buffer. Together with analyte molecule movement in the hotspot, it might therefore explain some of the signal fluctuations. Antenna alteration, such as angling and shrinking gaps, might also have taken place. Carbonization of ssDNA can also not be excluded entirely from these results. Nevertheless, the findings confirm the use of GNR dimers structured using DNA origami for single protein SERS from aqueous solution.

A question which remains here, is to what extent measuring SERS was analyte specific. To further test for this, two additional types of aqueous GNR dimer measurements were conducted. They are outlined in **Figure 4.2.4 A**. One with only myoglobin, and one in which both streptavidin and myoglobin were added to the solution. The latter oxygen (via iron) binding protein is found in muscle of mammals. It was chosen, as it does not bind to biotin. Additionally, its size, with a (hydrodynamic) diameter of ~3.5 nm [188] (and mass of 17 kDa), allows for it to fit into the plasmonic antenna hotspots.

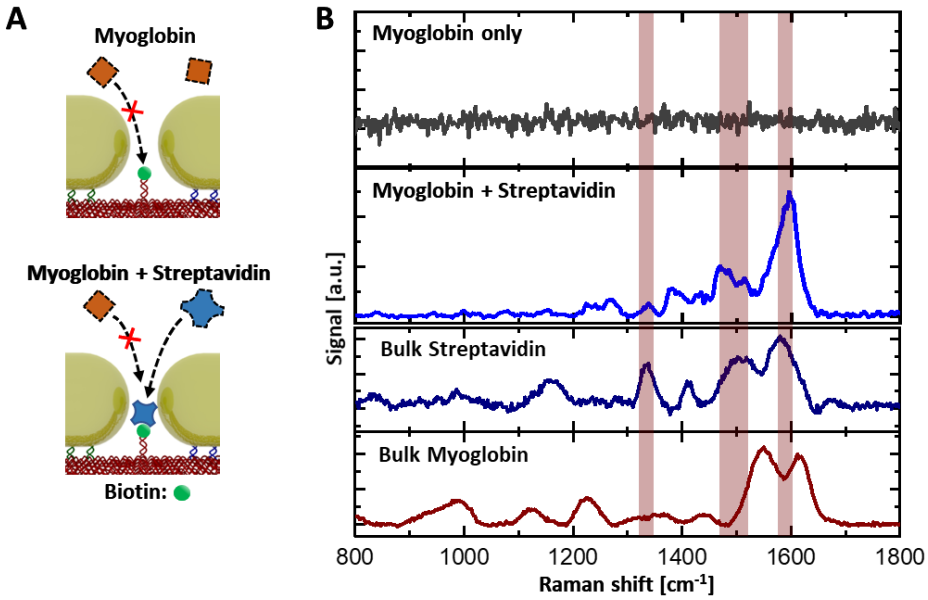

Figure 4.2.4: Protein Binding Specificity SERS Measurements. A Sketch of specificity measurements. Here GNR dimer gaps featured biotin equipped binding sites. Measurements were conducted either with only myoglobin, or myoglobin as well as streptavidin, added to the solution. **B** SERS measurement results with myoglobin only not being detectable, as well as a combination of myoglobin and streptavidin delivering streptavidin signal. Spectra shown were acquired within 0.5s of integration time and at 1 mW excitation power. The results are confirmed by bulk Raman measurements of both proteins. Spectra, apart from that of myoglobin only, feature background subtraction. This figure is adapted from: [136].

The measurements were conducted with biotin equipped GNR dimers. The presence of myoglobin alone in solution did not deliver a matching Raman spectrum, even after prolonged measurements. Measurements including streptavidin as well as myoglobin yielded SERS of streptavidin. Examples for this are shown in **Figure 4.2.4 B**. A comparison with both myoglobin and streptavidin bulk Raman spectra serves to further confirm the results. These measurement specificity findings indicate that GNR dimers function as intended by capturing analyte from solution.

4.2.2 GNR Dimer SERS Hotspot Effectiveness

In the previous section, the use of GNR dimers for SERS detection of larger proteins after diffusing into their accessible hotspots was demonstrated. However, some questions remain regarding the effectiveness of the system. In particular, these concern enhancement factors necessary for SM-SERS detection, as well as the time scales necessary for proteins accessing the hotspots. The aim of this section is to analyze and address these aspects.

For one, experimentally, single Cy3.5 molecules might not have experienced sufficient enhancement in ~8 nm hotspots for SERS. Instead, gaps they were prefixed into were potentially required to shrink. This regarding, Le Ru & Etchigoin identified necessary Raman enhancement factors of 10^9-10^{10} (~2-300[4]) for detecting single small nonresonant molecules, in a 2012 meta

study [189]. In 2021 work by Tapio et al. nonresonant SM-SERS of dye (TAMRA at 633 nm) required E-field enhancement factors around 300 from ~1-2 nm nanosphere gaps [40]. For the following, calculations will be used for further comparative analysis regarding Raman enhancement factors of dimer hotspots.

Peak E-field enhancements are significantly higher for GNR than GNS dimers at the same gap-lengths, as shown in **Figure 4.2.5 A**. They are also located more firmly in the bio-optical window according to corresponding peak enhancement wavelengths given in **Figure 4.2.5 B**. For ~8 nm gaps, the factors do however not match previously stated requirements for SM SERS detection. This also presents a concern for measuring SERS from smaller proteins such as biotin (0.24 kDa).

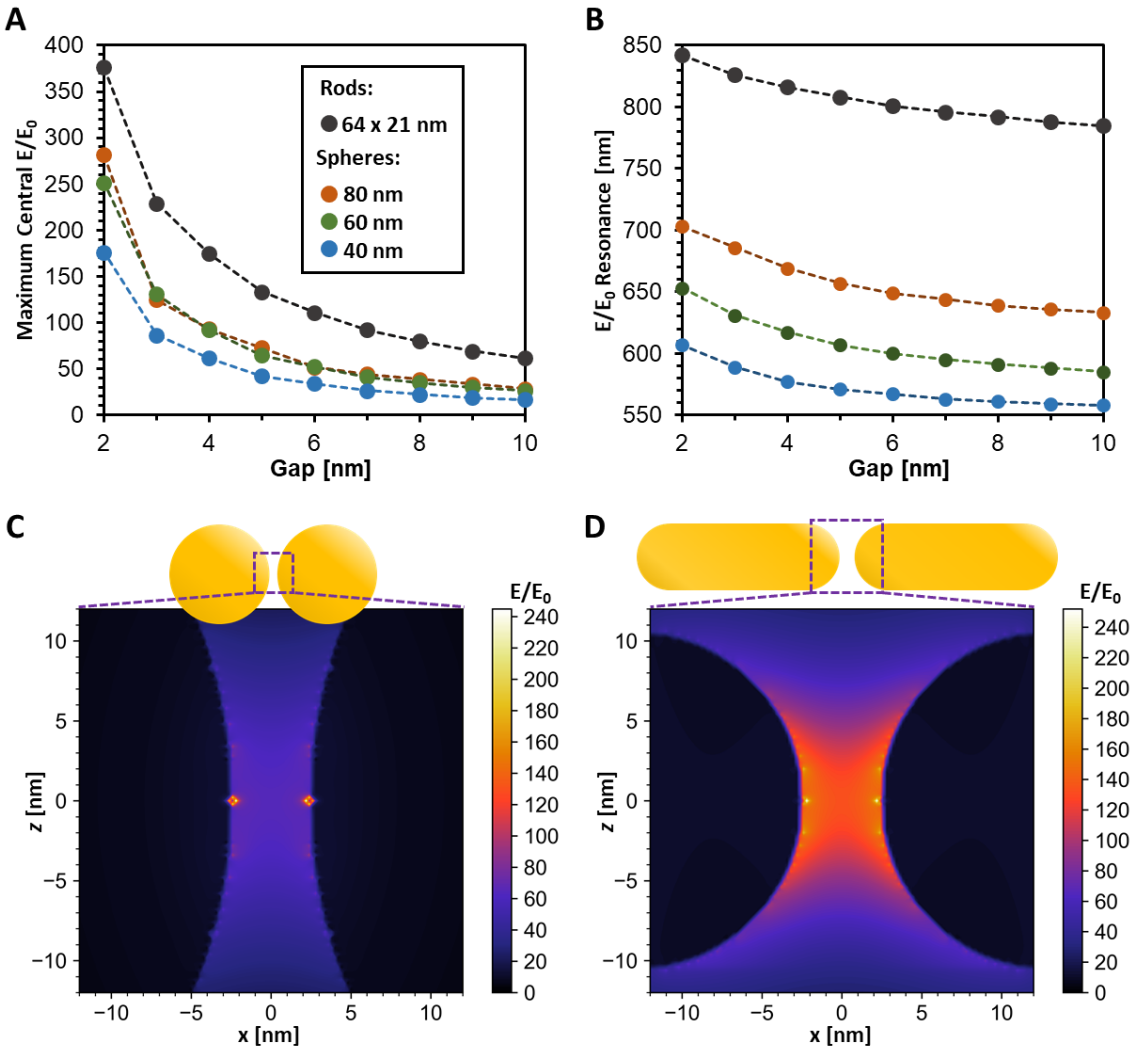

Figure 4.2.5: GNR and GNS Dimer E-Field Enhancement. A E-field enhancement maxima at gap centre, between two gold nanorods and nanospheres, in water, on glass. **B** Wavelength of maximum field enhancement (A) for a given gap. **C** Peak (at 607 nm) E-field enhancement map of GNS dimer with 5 nm gap. **D** Peak (at 808 nm) E-field enhancement map of GNR dimer with 5 nm gap. A, C and D have been adapted from: [136].

At first, this poses a potential conundrum of significant gap shrinkage being required for single Cy3.5 and biotin SERS, whilst open hotspots were usable for detecting single larger protein Raman signal. This might however be solved by the size of streptavidin and thrombin. Firstly, their molecular subgroups are relatively large, compared to typical gasses for example, thus featuring bigger Raman cross sections [5]. Whilst this is also the case for some of the smaller molecule components, larger protein's secondary structure subgroups often appear repeatedly. A primary example for this, is amide β-sheet in streptavidin and thrombin. In the case of streptavidin, as a tetramer, it is made up of four similar groups, each comprising of 70% of β-sheet [190]. This leads to a large amount of similar molecular oscillators, with the same Raman active modes. Therefore, measured single protein Raman spectra result from a superposition of many smaller scattering cross sections. This results in significantly more signal than what would be expected from conventional smaller single molecules. The effect does however require Raman enhancement of the whole molecule in the plasmonic hotspot. It might be expected from sphere-based dimers due to their lower curvatures, and thus potentially more homogenous gaps, as depicted in **Figure 4.2.5 C**. Here, as shown in **Figure 4.2.5 D**, higher curvature tips of GNRs do not appear to be a hindrance. The GNR dimer hotspots are calculated to be large enough to encompass whole ~5 nm proteins. Again, this is with the added benefit of significantly higher E-field enhancement compared to the sphere-based dimer.

For such GNR dimer hotspots, calculations reveal ~100 nm^3 with a peak EF above 100 in a 5 nm gap, and a central $4.1 \cdot 10^7$ peak EF^4 for an 8 nm gap, as examples. In contrast, 60 nm sphere counterparts feature ~0 nm^3 (excluding meshing related numerical artefacts), and $1.5 \cdot 10^6$ respectively. This indicates that, unlike ~1-2 nm gap 60 nm diameter GNS dimers [40], more openly accessible ~5+ nm gap hotspots between such GNS would not enable SM-SERS detection. According to calculations (**Figure 4.2.5 A**) comparable 80 nm GNS dimers would also be insufficient in hotspot strength for SM-SERS. It should be noted though, that together with 60 nm GNS counterparts, they would still fare significantly better than dimer antenna designs relying on 40 nm gold nanospheres.

An additional consideration can be linked to the bio-optical window measurement requirement. GNR dimers were successful here experimentally, and are inherently tunable via GNR aspect ratio. On the other hand, especially 40 nm, but also 60 nm and even 80 nm GNS-based dimers are not ideal for enhancement at and in the NIR according to FDTD calculations shown in **Figure 4.2.5 A** and **B**. Here, particularly 40 nm GNS designs – whilst having been highly successful for (SM-)SERS detection [38, 128, 129] – appear to feature subpar EF performance. This might be explained by a prevalence of more interband plasmon damping [59] due to their bluer (comparatively far lower than ~690 nm) BDP resonance. This disadvantage features despite higher nanoparticle curvatures around the hotspot, compared to the larger GNS

dimers. Smaller particles do however also feature smaller polarizabilities and optical interaction cross sections. The GNR-based dimer superiority therefore appears at least in part founded on the ability to maximize effective tip curvature and plasmonic excitability, whilst minimizing interband damping.

The requirement of larger gold nanospheres for measuring at the NIR might also grant GNR dimers a geometrical advantage, regarding DNA origami scaffolding, for analyte binding site placement. Larger GNS radii would necessitate longer linker strands for reaching into the dimer hotspot. Flexibility of double stranded DNA, with persistence length of ~50 nm [191], could thus impact the positional accuracy of analyte in the gap significantly. This might necessitate a more complex binding site design, which could also result in less openly accessible SERS hotspots.

At this point, it should be mentioned, that the desire to measure SERS close to the NIR also comes at a cost, namely of reduced Raman radiation by analyte according to **Equation 2.11**. With radiated energy scaling with $1/\lambda^4$, and thus photon count with $1/\lambda^3$, shorter wavelengths are inherently beneficial. From this perspective, ideally, the excitation wavelength is at the shorter end of the preferred wavelength range (the bio-optical window), which is the case here with 671 nm. The wavelength is also similar to that used in other aforementioned studies on gold nanoparticle-based dimers (typically around 600 nm). This renders results comparable regarding E-field enhancement for SERS. GNR resonance tunability is thus again particularly useful. It could in theory allow for limited further optimization of excitation and antenna resonance towards the lowest wavelengths of the bio-optical window.

The GNR dimer hotspots do also not present significantly more volume of strong Raman enhancement, than the size of streptavidin and thrombin according to modelling presented in this chapter. This indicates that it was only single analyte molecules, or at the very least, that it cannot have been significantly larger quantities of such, which were detected. This in turn supports theory of high E-field enhancement factors, and that the detection scheme functioned via binding of single analyte at the hotspot. However, within the scope of this project only an estimated ~10-15% of DNA origami-based GNR dimers yielded protein SERS signal. To explained this, several factors are examined in the following.

For one, these include time scales on which proteins might enter the hotspots and how probable this is during a sample measurement procedure. Towards analyzing this, mean diffusion times for proteins entering dimer gaps were approximated with a numerical 3D random walk model. The hotspot was approximated with a 4 × 4 × 4 nm “hitbox”, freestanding in a 400 × 400 × 400 nm simulation volume (with reflective surfaces). This is illustrated in **Figure 4.2.6 A**. Diffusion proceeded stepwise, in 4 nm increments. The value was chosen to account for nanoscopic protein scale path self-overlap, as it is not relevant to more macroscopic diffusion into dimer gaps. It also

corresponds to the hitbox width. Considerable diffusion movement within a diffusion path step might therefore approximate exact protein positioning for binding within a diffusion time step. The average amount of time it would take for a molecule to travel the 4 nm path step distance by diffusion, was derived via diffusion coefficients:

$$D = \frac{k_B \cdot T}{6\pi \cdot r \cdot \eta}. \tag{4.1}$$

Here, r is the hydrodynamic radius, with 2.82 nm for streptavidin [171], and 2.05 nm in the case of thrombin [185], resulting in a D of $7.72 \cdot 10^{-11}$ m^2/s for streptavidin and $1.06 \cdot 10^{-10}$ m^2/s for thrombin in water. This corresponds to 4 nm step times of 207 ns and 157 ns respectively.

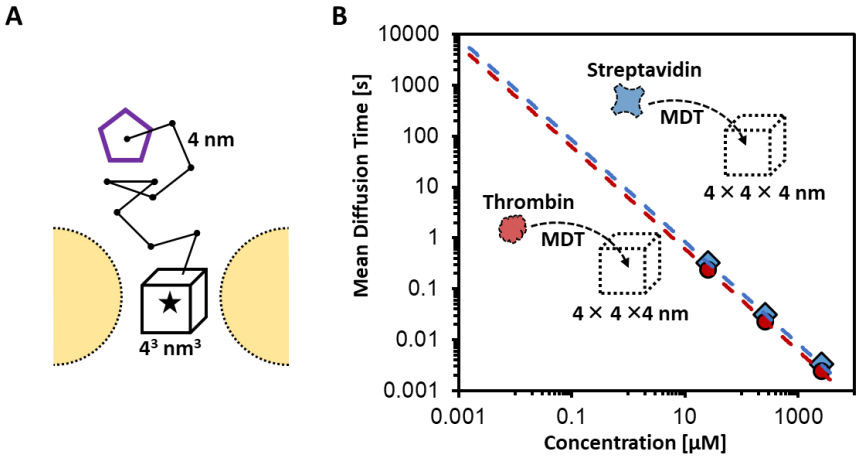

Figure 4.2.6: Localization of Proteins in Hotspot. A Illustration of mean diffusion time modelling for proteins (purple pentagon) to enter GNR dimer hotspots. **B** Calculated concentration dependent diffusion times for streptavidin (blue) and thrombin (red). Different numbers of "proteins" were positioned randomly in the volume, representing different concentrations, and were made to diffuse stepwise. This was done 100 times for each concentration, with the average number of steps it took, multiplied with the 4 nm diffusion step time, to find the mean diffusion time (MDT). The dashed lines (linearly) fit the inverse relationship between (logarithmic) concentration and (logarithmic) MDT, and are extrapolated to consider both experimental and physiological concentrations. This figure has been adapted from: [136].

The results of these calculations are depicted in **Figure 4.2.6 B**. Here a clear inverse relationship between MDT and concentration is visible, via relationships of 8.4 s·µM for streptavidin and 6.1 s·µM for thrombin. This means that diffusion into hotspots was not a limiting factor for both streptavidin, and thrombin in experiments with concentration ranging between 0.33-4.2 µM and 6.9-61 µM respectively. More explicitly, these molarities correspond to MDTs around 0.1-10s.

Calculated mean diffusion time scales do however fall well within the usual time series span of ~50s employed in this work, for measuring SERS. The question whether analyte might not have entered hotspots during the SERS accumulations does therefore arise. Here, these dielectric particles could then be held in place by laser induced trapping forces. Such optical tweezing forces can be strong enough for trapping both micron scale dielectric particles in a laser focus [192], as well as smaller protein molecules in metallic nanohole hotspots [193]. If maintaining such optical

traps was in fact necessary, this would negate SERS specificity via analyte binding sites. It could also impose limits to the GNR dimer system when measuring both experimental, as well as real world analyte concentrations. For example, physiologically relevant levels of Thrombin [194] of 1-500 nM, could present a time constraints, as diffusion times into hotspots might range from ~1s to several hours. Therefore, optical trapping forces could not only counteract measuring specificity via analyte binding. A potential requirement of measuring a single antenna for such a long time might also not be practical.

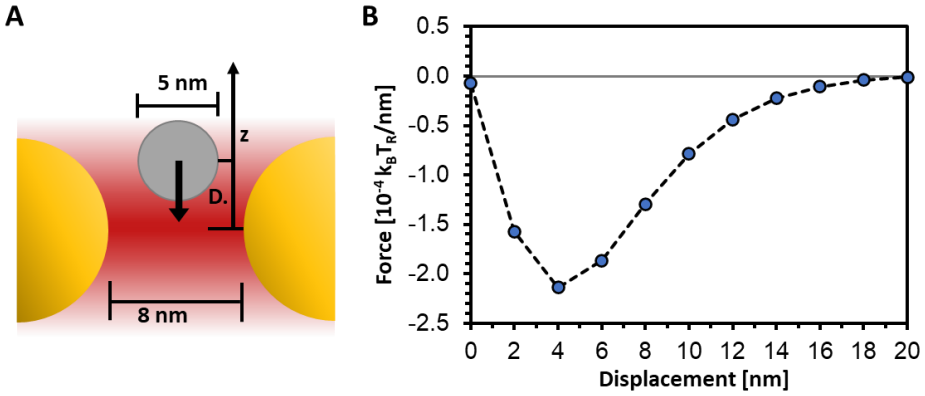

Figure 4.2.7: Optical Trapping Forces in Hotspot. A Illustration (not drawn to scale) of dielectric trapping with the black arrow denoting optical force pulling the particle along the displacement (D.) z-axis into the GNR dimer hotspot centre. **B** Calculated restoring force for dielectric sphere into hotspot centre of a GNR dimers with an 8 nm gap. The system was simulated on a glass substrate in water, with displacements perpendicular to the substrate plane. Excitation intensity corresponds to the laser focus centre with a power of 1 mW.

A trapping effect, illustrated in **Figure 4.2.7 A**, could be particularly pronounced here. This stems from the mW scale powers of the focused laser combined with significant E-field enhancement, strongly gradated at the GNR dimer hotspot. It was therefore also calculated using FDTD for GNR dimers with 8 nm gaps, with results depicted in **Figure 4.2.7 B**. This was done for a 5 nm sphere, with a refractive index of 1.6, chosen to approximate proteins in aqueous solution [195]. As can be seen, it does not experience significant forces in the context of room temperature energy when displaced off-dimer axially, from the hotspot centre. Trap depths within the 10 nm scale potential might thus be 2-3 orders of magnitude bellow room temperature energies of 1 k_BT_R during experiments. The results therefore support analyte detection specificity via the binding sites of the GNR dimers for the proteins studied here.

Nevertheless, forces experienced by the proteins are significant, reaching $10^{2\text{-}3}$ aN at experimentally used laser powers. They could thus contribute to stabilizing potential analyte directly in the SERS hotspot. They might also contribute to observable Raman fluctuating and signal becoming stronger from the start of measurements. Further, scaling of optical forces with the analyte polarizability, results in a third power dependency with its span [88]. For larger biomolecules and higher laser powers this could in principle also lead to significance of the optical trapping effect.

Another likely factor in the low SERS yields is the range of synthesis outcomes. Intra dimer GNR angling, discussed in the previous **Subchapter 4.1** does not appear to be a major factor in terms of field enhancement. It could however misalign the linker strand and binding site from the plasmonic hotspot, as well as make the gap less accessible. Gap size variations can also be expected to influence SERS signal yields. On the one hand, according to the measured distribution (**Figure 4.1.3 G** and **H**), a significant proportion of GNR dimers might exist, with gaps which are too small for streptavidin and thrombin to enter the hotspots fully. On the other end of the scale, gaps too large for E-field enhancement to be sufficient for clear detection by SERS might also exist. Therefore, only a proportion of the antennas might have been suitable for single protein SERS. For antennas with gaps around 8 nm in span ~40% of the dimers fell within a gap range of 3 nm (for example 6.5-9.5 nm). This value drops to ~30% and ~15% for 2 nm and 1 nm gap size ranges respectively. This aspect can still apply for shrunken gaps from laser excitation and after angling. Gap variations could therefore have contributed significantly to a limited SERS yield.

To further examine GNR dimer hotspots, additional measurements with the aim of detecting Raman scattering of biotin-binding immunoglobulin G (IgG) were conducted. IgG was chosen, as the molecule is significantly larger than both streptavidin and thrombin. It has a size of 14.5 × 8.5 × 4 nm [196], a hydrodynamic diameter of 10.6 nm [171] and a mass of ~150 kDa. The protein is also the most common serum antibody found in human blood [197]. SERS measurements were carried out in solution at concentrations ~0.13 µM, with biotin functionalized antennas. Measurements would be expected to feature slightly longer, but similar mean diffusion times into hotspots as streptavidin and thrombin. Here, SERS detection was unsuccessful, even after hour long incubation times. This indicates that hotspots large enough for accepting IgG might not be strong enough for sufficient Raman scattering by the protein.

Whilst SERS of single proteins was measurable from solution with these GNR dimer nanoagents, the findings also present limitations of the antennas. These do however suggest an opportunity to improve upon the gold nanorod dimer design, which is investigated in the following subchapter.

4.3 Improving Nanorod-Based SERS

The question how these already functional GNR dimers might be improved upon encompasses multiple aspects. In terms of antenna stability, recent scientific advances have shown that DNA origami can be silicified [198], to strengthen it against thermal and mechanical influences. Further, this can be done site specifically [199], so as to allow for binding sites to remain functional [200]. Stability might also be increased by lowering antenna temperatures. This can be achieved using more effective environmental heatsinks such as graphene coated glass [201], or even sapphire (~20 W/(m·K) thermal conductivity vs. ~1 W/(m·K) for glass) substrates [202]. Such modifications would also allow for greater laser powers to be used, without destroying the nanoagents and analyte, thus increasing SERS signal. On the one hand, this might enable faster detection of a larger range of molecules, from bigger hotspots. On the other hand, there are also potential downsides to these modifications. For one, stabilizing the antennas against deformation could inhibit increased E-field enhancement factors from shrinking gaps. Additionally, free substrate choice might not be possible in practical applications of the nanoagents.

Another method lies in an increase of electromagnetic Raman enhancement factors directly, which is the focus of the following section. One of the first aspects which might come to mind is the curvature of the hotspot forming particle ends, and how to improve upon spheroidal metallic nanorod tips. The second relates to the properties of metallic particles constituting the antennas. A third option discussed, is using more than two GNRs for generating SERS hotspots.

4.3.1 GNR Tip Curvature at the Hotspot

In essence, gold nanorods already feature ends with higher overall curvatures than gold nanospheres of similar volume. Thus, even sharper tips might appear as a logical step in dimer evolution, to further raise Raman enhancement factors. In fact, numerous studies have been devised using different types of particles featuring more point-like ends for assembling dimers. The particularly impressive example by Zhan et al. [42] involved bowtie nanoantennas, where 5 nm gaps yielded enhancement factors ~220 experimentally and central EF of ~600 in calculations. Other studies have included bi-Au(Ag) nanostars [41, 130, 131], albeit with ill-defined nanogaps, and where monomers alone featured sufficient field enhancement for SERS [41]. Further, dimers based on sharply tipped bipyramids have been exploited experimentally for their field enhancement, by Kaur et al. [146]. Whilst the antennas enabled detection of single thioflavin molecules, unquantified hotspot size appeared to be well under 3 nm according to TEM.

Here, in the scope of GNR dimers, nanorods with conical tips at the gaps were examined, as is depicted in **Figure 4.3.1 A**. This shape might be somewhat hypothetical, also due to the

asymmetry involved. It does however allow for varying an effective tip sharpness and enables direct comparability to spherically endcapped GNR-based dimers. An important constraint to consider here is that metal lattice structures do not allow for infinite tip curvatures. The endcap cones were therefore truncated with different radii. Results (**Figure 4.3.1 A**) show that sharper GNRs appear to offer benefits for SERS (over their spherically ended counterparts) for smaller gaps, but not for larger hotspots.

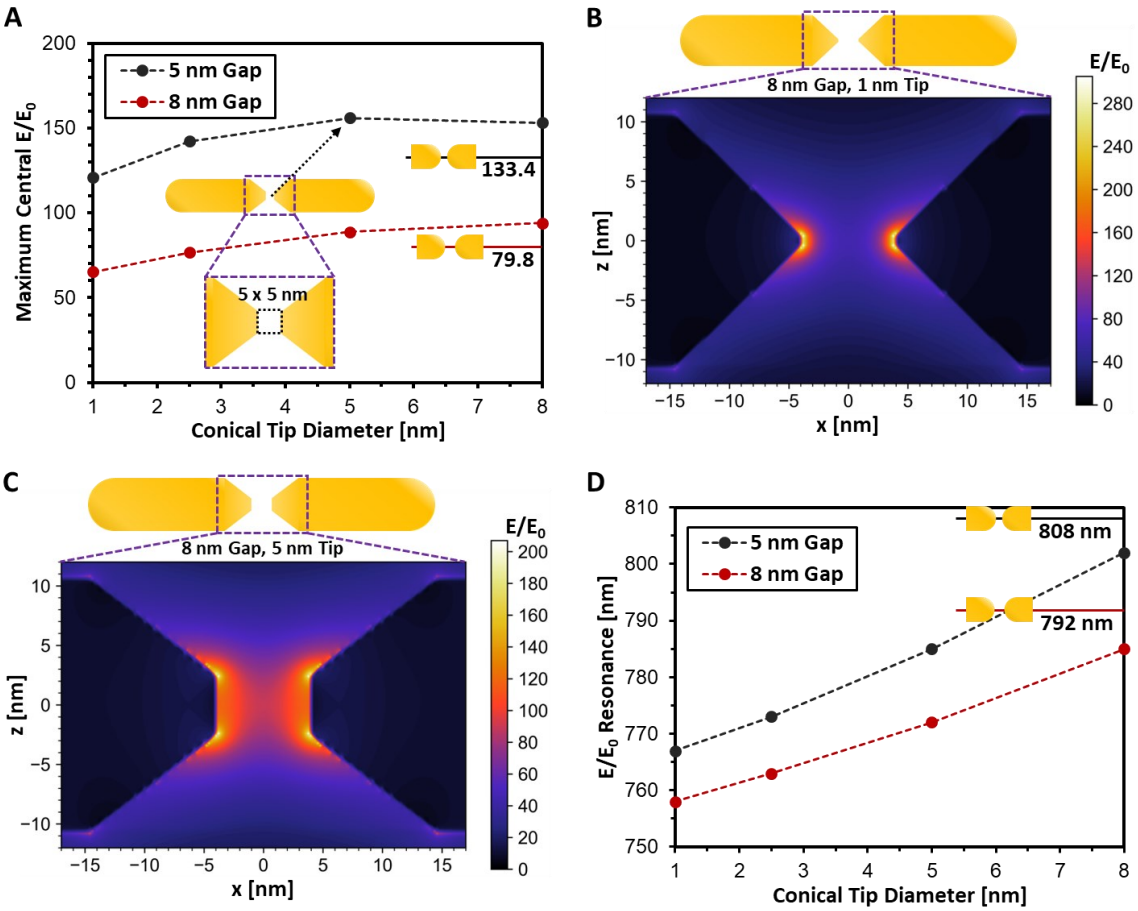

Figure 4.3.1: Effects of Tip Sharpness on the Plasmon Hotspot. A Calculated maximum central E-field enhancement for GNR dimers with truncated tips at hotspots (21 × 64 nm GNRs, as illustrated in sketch). Truncation diameter is varied for 5 and 8 nm gaps, with a comparison to spherically endcapped GNR dimers. **B** Maximum E-field enhancement (at 758 nm) map covering 1 nm truncation diameter capped GNR dimer hotspot. **C** Maximum E-field enhancement (at 772 nm) map around 5 nm truncation diameter capped GNR dimer hotspot. **D** Wavelength of maximum E-field enhancement at hotspot centre for structures shown in A. Calculations were performed with antennas on glass, in water. A, B and C have been adapted from: [136].

A limited E-field enhancement from sharper tips is not only found at the gap centre, but also throughout the hotspot (excluding truncation edges). This can be seen for the 8 nm inter-connical-tip distance example in **Figure 4.3.1 B**, with 1 nm tip diameter. Here too, more blunt tips with a 5 nm diameter example featured in **Figure 4.3.1 C**, appear favorable. The reason for this finding might lie in the reduced plasmonic coupling between the plasmonic particles constituting the dimer. This is supported by the wavelengths corresponding to hotspot centre resonance depicted in **Figure 4.3.1 D**. These blue-shift for sharper tips. A possible explanation would be effectively

higher tip curvatures, raising the effective interparticle distance around the span of the gap. This span is uniform within the truncation diameter. It also matches a strong decrease in hotspot intensity outside of the central truncation diameters. Tip curvature alone might however effect resonance slightly as can be seen in **Figure 2.2.3**. Here lowered curvatures, from an ellipsoid to a rod, result in a red-shifted resonance. However, dimers with smaller 5 nm gaps feature stronger resonance red-shifts than 8 nm gap counterparts when conical tip diameters increase (**Figure 4.3.1 D**). As this coincides with smaller gaps leading to stronger plasmonic interaction, nanoparticle coupling does appear to be influenced significantly by tip geometry as well.

Sharper tips might still offer greater benefits for single smaller molecule SERS, or partial analysis of larger analyte. An extreme example of this is TERS. Increasing Raman scattering from larger molecules does however require wider hotspots for them to fit inside. These appear to benefit from more bluntly tipped nanoparticles, especially when the goal is to probe the whole molecule. Further, hotspots formed by very sharp tips might be particularly susceptible to misalignment between the nanoparticles. Due to the small coupling interfaces, even small absolute amounts in off-axiality of tips might greatly change the hotspot in terms of location, size and strength. In practice, this could make synthesis of dimers with functional and accessible hotspots from sharp tips difficult and unreliable. Past attempts have thus relied on linker strands spanning and thus obstructing the hotspot by directly connecting bipyramid ends [146]. This might be particularly detrimental to analyte capturing schemes, as the hotspots are already limited in size. Template binding schemes on the other hand have so far offered no definitive way of aligning tips of metallic nanostars towards one another [41, 130, 131].

Additionally, whilst 5 and 8 nm capping diameters of conical tips appear to offer high field enhancement, clear synthesis strategies for achieving these do not appear to exist. Therefore, GNRs with more rounded tips seem to present an advantageous option for assembling dimers for SERS from larger gaps. This also poses the question whether less hemispherical, effectively more flat ellipsoidal ends might not offer further benefits for SERS from nanorod dimers. To answer it, calculations were performed on ellipsoidally endcapped GNRs.

Here an ellipsoidicity parameter describes the length to radius ratio of the endcap. For spheres it equals one, for flatter tips it is smaller. Examples for field enhancements at 8 nm gaps are depicted in **Figure 4.3.2 A** and **B**, for ellipsoidicities of 0.5 and 0.25 respectively. As can be seen, the hotspots become larger and more homogenous for blunter tips. Interestingly, for the lower ellipsoidicity nanorods relatively highly curved edges of the endcaps appear to dominate in terms of potential Raman signal enhancement factors. This stands in contrast to spherically endcapped GNR dimers. For these highest E-field enhancements were found around the tips, at the central antenna axis.

Hotspot homogeneity also translates to maximum central E-flied enhancements shown in **Figure 4.3.2 C**. Here, blunter tips feature larger enhancement as of ~7 nm, whilst below this span sharper tips dominate. The effect might stem from higher enhancement at sharper tips overweighing the impact of a more uniform hotspot for smaller gaps. **Figure 4.3.2 D** depicts wavelengths of maximum enhancement for the three differently endcapped GNRs. Again, increased plasmonic coupling, manifesting in red-shifted resonance, appears to go hand in hand with more homogenous field enhancement across dimer hotspots. It should however be noted once more, that tip bluntness alone can result in red-shifted resonance between antennas with the same aspect ratio. Nevertheless, spectral peak position differences between dimer types (in terms of GNR endcap curvature) increase when shrinking gaps from 12 to 3 nm. Coupling therefore appears to increase with lower values of tip ellipsoidicity.

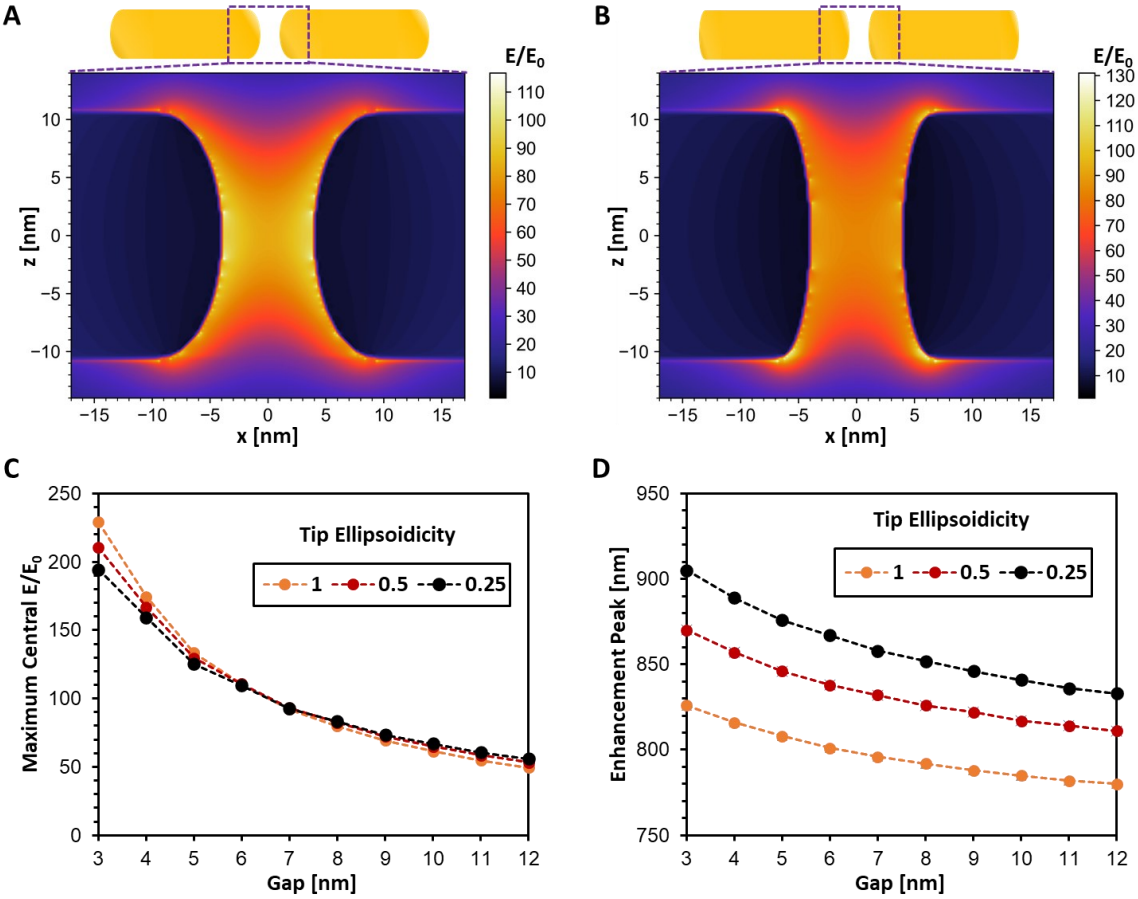

Figure 4.3.2: Effects of GNR Tip Ellipsoidicity on plasmonic Hotspots. A Calculated maximum (at 826 nm, for the hotspot centre) E-field enhancement map for dimer based on tips with an ellipsoidicity of 0.5. **B** Calculated maximum (at 852 nm) E-field enhancement map for dimer based on tips with an ellipsoidicity of 0.25. **C** Calculated maximum central E-field enhancement for dimers consisting of GNRs with differing tip ellipsoidicity and gaps. **D** Wavelength of maximum E-field enhancement at hotspot centre of dimers with differently tipped GNRs.

According to these results, blunter tips might feature advantages, over higher curvature counterparts, for SERS of larger molecules such as IgG. Hotspots between such ellipsoidal endcaps might however be impacted more significantly by angling, than between spheroidal ends

shown in **Figure 4.1.8**. For ellipsoids, hotspot shape would not remain unaffected around the gap span. The span would also shift towards the inside of the angle. Such effects might already have taken place to a certain extent in experiments. Even if here chemically synthesized GNRs feature relatively hemispherical ends according to electron microscopy results. Synthesizing GNRs with explicitly flatter ends for dimers might therefore be an effective way of obtaining stronger SERS signal for larger analyte.

4.3.2 Silver Nanorod Dimers

A frequently asked question when discussing plasmonic antennas is whether it might not be possible to use silver instead of gold particles to enhance efficiencies for radiative applications. Here an advantage of silvers over gold stems from a lack of interband damping in the visible range. Thus, silver nanosphere plasmonic coupling derived hotspots have been used to great effect for single protein SERS studies [40, 143]. Silver nanorods (AgNRs) are also synthesizable [203, 204], and have been employed for sensory experiments, including SERS detection of aqueous dye molecules at µM concentrations [205]. In the context of this thesis, silver nanorod dimers will be discussed theoretically.

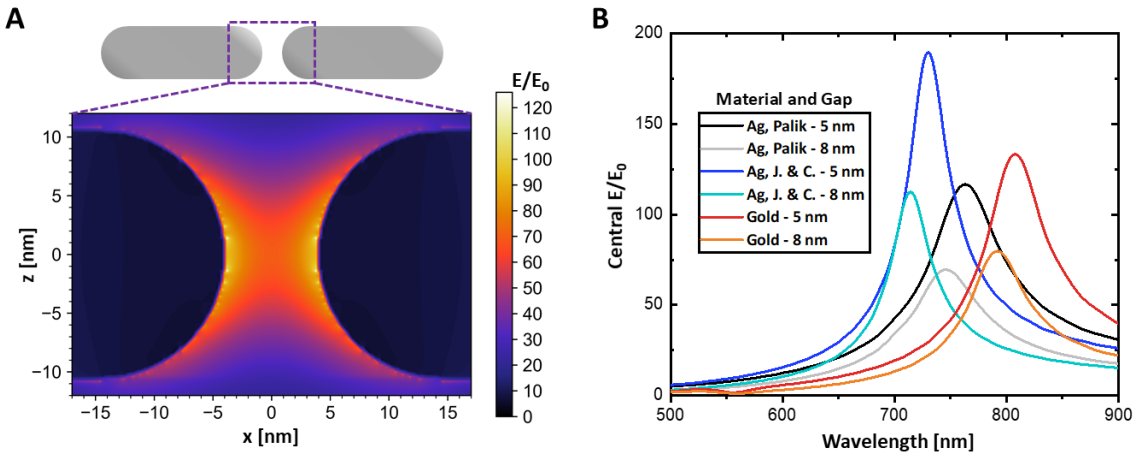

Figure 4.3.3: Calculated E-Field Enhancement of Silver Nanorod Dimers. A Maximum (at 746 nm) E-field enhancement Map for 8 nm gap AgNR (21 × 64 nm, tip to tip, on glass and in water) dimer, with Silver from Palik [206]. **B** Comparison between gold (single crystalline from Olmon et al. [55]), and silver with differing permittivities (Palik [206], and Johnson and Christy [57]) nanorod-based dimer E-field enhancement spectra at hotspot centres.

The first step of this brief analysis was to conduct FDTD calculations of E-Field enhancement for silver counter parts of the GNR-based dimers examined in previous sections. As is displayed in **Figure 4.3.3 A** for an 8 nm gap, E-field enhancement is significant throughout an antenna's hotspot. However, calculations also reveal that there might be a disadvantage in field enhancement compared to GNR-based dimers. These are shown in **Figure 4.3.3 B**, and display a strong dependence of EF results on the experimental permittivities used for modelling.

Besides a potential lack of improved electromagnetic Raman enhancement, silver-based GNR dimers might also feature other downsides. Notably, silver is less chemically inert than gold, and, in particular can oxidize [207], incorporating oxygen into the lattice and releasing Ag^+ ions into aqueous solution, causing toxicity [208]. Additionally, plasmonically excited silver nanoparticles are likely to carbonize their surroundings, as described in **Section 4.1.5**, potentially including analyte [145]. This effect is however less pronounced in water, which is favorable to protein measurements similar to the ones presented here. Further, issues of analyte alteration and silver oxidation might be alleviated by a thin gold coating of the AgNRs [209]. There might however still be an overall insufficiency of incentive for using silver nanorods for SERS in the bio-optical window.

In terms of E-field enhancement, the main advantage of silver can be explained by the lack of interband damping of gold at wavelengths at and in the NIR [59]. In fact, silver according to Palik [206] (1985) appears to feature larger imaginative permittivities than gold at red and NIR wavelengths. These are however lower according to Johnson & Christie [57] (1972). In practice, results might lie somewhere in between the two according to later (2016) work by Jiang et al. [210]. Therefore, this still presents a potential advantage for silver. Another advantage might lie in the geometry of silver nanorods. Here, gold nanorods coated with a silver layer [211] appear to feature significantly flatter endcaps than spheres according to TEM images. This might be a useful basis for more homogenous hotspots for SERS of larger analyte, as discussed in the previous **Section 4.3.1**.

Silver-based nanorods therefore appear promising for future studies. Proneness to environmental carbonization, chemical stability and synthesizability of geometries should however be kept in mind when looking into alternative metals to gold for designing SERS nanoagents.

4.3.3 GNR Trimers and Tetramers

A third path, besides sharper tips and alternate metals, for constructing more effective plasmonic hotspots, lies in structuring nanoantennas with more than two GNRs. Such multimers, with DNA origami scaffolding templates, have been employed before in SERS studies by multiple researchers. For one, Pilo-Pais et al. used gold nanosphere tetramers connected by rectangular templates for detecting 4-aminobenzenethiol [142]. Also, Heck et al. employed triangular templates for pattering silver sphere trimers around single streptavidin molecules [143]. Finally, Fang et al. used up to 4 GNS on triangle-based templates for detecting single SYBR Green I dye molecules [144]. In these cases, however, the main SERS hotspot of an antenna was found in the gap between only two of its multiple nanospheres. Thus, more than two nanoparticles might not

necessarily benefit single-molecule detection from a single hotspot significantly. This might be underlined with a particularly extreme case of pattering rows of plasmonic nanostars with DNA origami, to generate rows of similar hotspots by Kaur et al. [132]. Plasmonic nanoantenna-based multimers for generating larger hotspots have been demonstrated with the help of focused ion beam milling (FIB) [212]. Here, Morshed et al. detected SERS from two-bowtie antennas. The tetramers with 30 nm central gaps featured 4 planes of symmetry. This offered similar enhancement for circular as well as linearly polarized light for detecting Raman signal of bulk ethanol, in the central antenna hotspot.

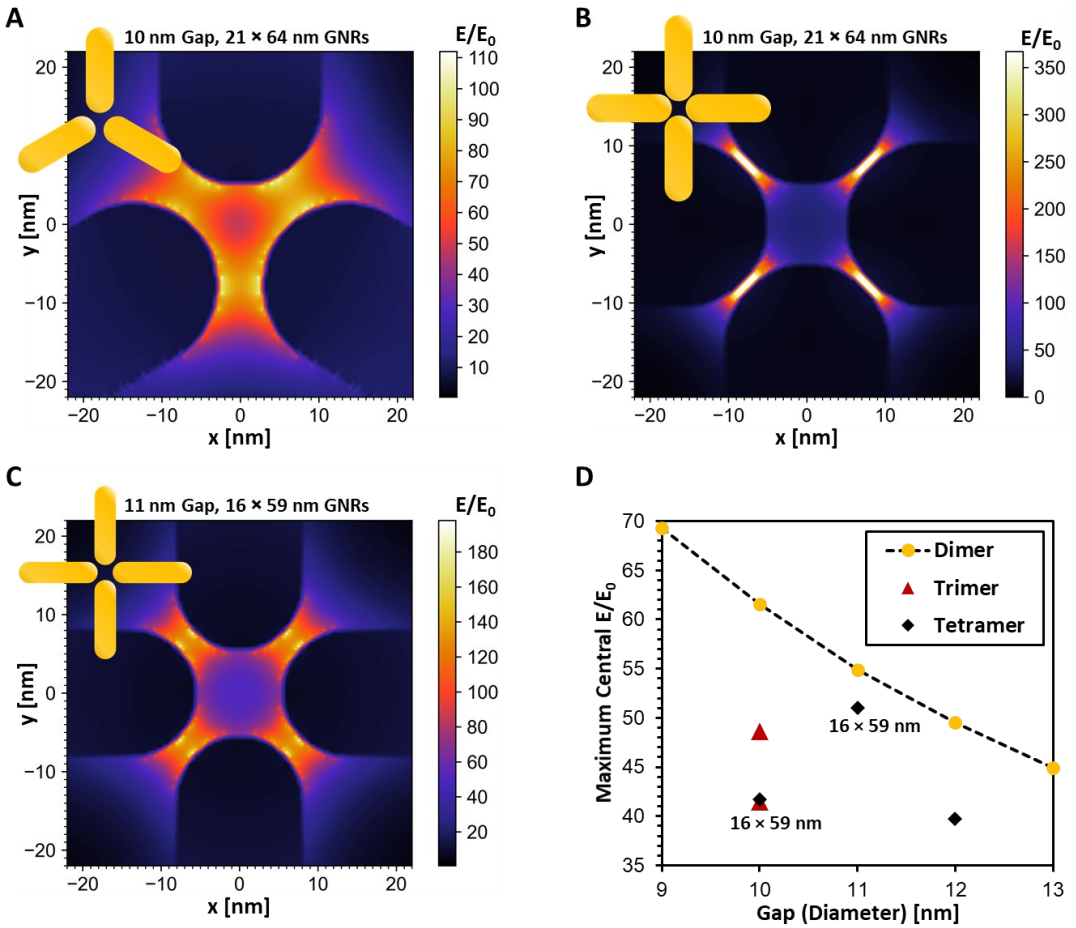

Figure 4.3.4: Effects of using multiple GNRs for E-Field Enhancement. A Maximum E-field enhancement (at 807 nm) map of a GNR-based trimer, with 10 nm circular gap. **B** Field enhancement (at 866 nm) map of a GNR tetramer, with a 10 nm (circular diameter) gap. **C** Field enhancement (at 871 nm) map of a 16 × 59 nm GNR based tetramer, with an 11 nm circular gap. **D** Exemplary maximum hotspot central E-field enhancement of different GNR-based multimers for different gaps. GNR dimensions are 21 × 64 nm, if not stated otherwise. Here (for trimers and tetramers), excitation occurred with circularly polarized light to account and approximate for the additional symmetry and enhancement axes (particularly under conditions of circularly polarized excitation). A and B are adapted from: [136].

To examine how GNR-based multimers might perform, FDTD calculations on trimers and tetramers with symmetric starlike shapes were conducted. An example of a trimer with a 10 nm gap (diameter of a circle around which GNR tips are oriented) is shown in **Figure 4.3.4 A**. Here it can be seen that the antenna features strongest E-field enhancement in the narrow gaps between

neighboring GNR tips and not at its centre. This phenomenon has also been reported on in the context of silver nanodisc trimers [213]. In fact, here (**Figure 4.3.4 A**) the central enhancement is lower than that of comparable GNR dimers. A comparable tetramer featured similar patterns of enhancement to the trimer, with strongest enhancement between the antenna tips in **Figure 4.3.4 B**. The central hotspot was however stronger in general. Shrinking nanorods (to 16 × 59 nm) offered an increased advantage for a central 11 nm hotspot, as depicted in **Figure 4.3.4 C**. At least in the xy-plane. Coupling between neighboring GNR tips was further reduced, as indicated by lowered field enhancement at those locations. However, GNR dimers featured higher central E-field enhancement factors for the same central gap diameters. This was also the case for additional multimer examples as shown in **Figure 4.3.4 D**.

Whilst GNR trimers are found to perform worse than similar dimers, tetramers appear to feature some merits. For one, E-field enhancement is more homogenous throughout the gaps. This results in larger effective hotspots, in the xy-plane. Also, Raman enhancement can take place along multiple axes. The later aspect might effectively double SERS signal of tetramers over that of dimers. Coupling between neighboring GNR tips is also particularly reduced for growing gaps and thinner/smaller GNRs. The latter should however suffer limitations in hotspot size in the z-axis. Further, tetramers in general might be more complex to structure than dimers, and be more prone to synthesis variation, with potentially negative impacts on SERS performance. Additionally, gap shrinkage, potentially necessary for SM-SERS, could be hindered by nanorod tip interference. It could also result in increased E-field enhancement between neighboring GNR tips instead of at the multimer gap centre. This might also be particularly disadvantageous to the use of more flatly tipped metallic nanorods, for increasing hotspot effectiveness, as described in **Section 4.3.1**. Here particularly, E-field enhancement might be highest in confined spaces between edges around the nanorod tips, instead of in the open hotspot centre.

Nevertheless, tip-to-tip metallic nanorod tetramers still present advantages. They should therefore not be disconsidered as potential candidates for detecting even larger diffusive molecules, than streptavidin and thrombin.

Again, whilst offering potential benefits for future detection SERS schemes towards larger biomolecules, this subchapter supports the finding that GNR-based dimers are advantageous for SERS. At the very least regarding design complexity and synthesis, compared to other nanorod multimers. Together with silver nanorods, especially tetramers might offer further advantages for Raman detection. Overall, however, a simple dimer design with nanorod tips featuring lower curvatures appears particularly promising. Further reductions in design complexity, for generating coupled plasmonic particles towards SERS, are the subject of the next chapter.

5 Split Gold Nanorods as Dimers for SERS

The previous chapter demonstrated the use of GNR dimers structured with DNA origami for measuring SERS from larger gaps. More specifically, this was accomplished for ~5 nm large proteins. For smaller analyte, smaller accessible hotspots with higher field enhancements might however be better suited. Recently, a method for generating plasmonic nanodimers on a substrate with light, directly from a solution of plasmonic nanorods, was discovered by C.M. Maier in the context of his 2020 PhD thesis [56]. In this work a focused NIR laser was used for optically splitting nanorods into two spheroids, and printing these onto glass substrates as dimers. This GNR dimerization process is described in **Subchapter 5.1**. Preliminary spectroscopic results [56] suggested a potential existence of gaps, significantly smaller than 1 nm. This chapter presents an answer to the question of such gaps as hotspots for SERS. It is based on: [214] (Schuknecht, Maier et al.).

Whilst sub nanometer gaps might limit the size of analyte fitting into the hotspot, they can offer particularly high field enhancement, as theorized by Esteban et al. [76]. Traditional top-down lithography methods require more extensive work to pattern such features (in limited dimensions). For example, two-step electron beam lithography (EBL) for angstrom gapped gold nanocylinder dimers, by Zhu et al. (2014) [215]. Alternative sequential optical printing methods of metallic nanospheres from solution with a focused laser, as by Urban et al. [84] have also been explored. These have yielded limited results for printing GNS dimers with nm small gaps [216] due to thermophoretic forces [217]. These arise when the first printed particle is heated, thereby disturbing printing of the second.

To avoid thermophoretic effects, printing has also been conducted on polymer, which was heat shrunken to close gaps between neighboring particles [218]. Additionally, Gargiulo et al. have printed Au-Ag heterodimers, thereby lowering simultaneous plasmon resonance and heating, on glass substrates [216]. Further, more highly thermally conductive graphene oxide coated sapphire substrates, for lowering thermal gradients in general, were explored for printing Au-Au dimers [202]. Gaps here were either at least in the several 10s of nm range, strongly limiting field enhancement, or the particles appeared merged, eliminating plasmonic hotspots altogether. This calls for alternative ways of optically assembling SERS nanoagents, such as via GNR splitting.

Here, in **Subchapter 5.2**, the presence of gaps is confirmed by HR-TEM, and their sizes are determined to be ~0.8 nm spectroscopically. GNS dimer printing from optically split GNRs therefore have potential for SERS. Demonstration of this is the subject of **Subchapter 5.3**. It is followed by a discussion on what determines particle separation in **Subchapter 5.4**. This culminates in an outlook on tuning such optically generated plasmonic dimer nanoagents.

5.1 Optical GNR Splitting and Dimer Printing

The first step in analyzing dimers generated by optically splitting GNRs lies in understanding the reshaping process and producing samples. For this, CTAB (cetrimonium bromide) capped GNRs resonant to 1064 nm light in aqueous solution (25 × 137 nm, 0.07 nM, purchased from *Nanopartz*) were employed. An exemplary GNR and its scattering spectrum, is depicted in **Figure 5.1.1 A**. Its main longitudinal plasmon peak in the NIR is located similarly to that calculated for a GNR in **Figure 5.1.1 B**. Here, the longitudinal plasmon peak is blue shifted from 1064 nm due to the GNR environmental refractive index being lower in air than in water. Experiments involved ~3 µl of the GNR solution injected into the water droplet medium of a DFM setup.

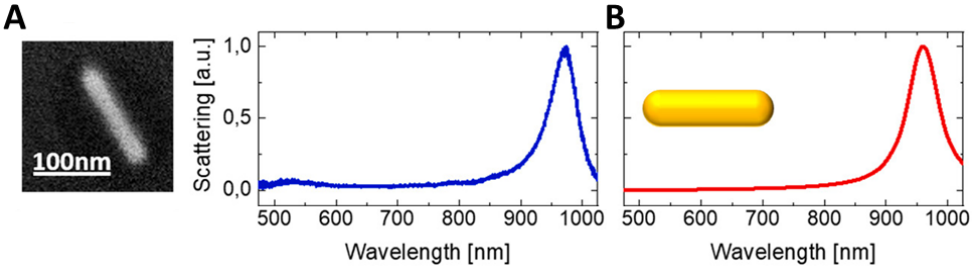

Figure 5.1.1: Gold Nanorod used for Dimerization. A SEM image of GNR and corresponding scattering spectrum in air. **B** Scattering spectrum (for longitudinally polarized excitation) of a 25 × 137 nm GNR, on glass in air. Adapted with permission from [214] (Schuknecht et al.). Copyright 2023 American Chemical Society.

Generating dimers by optical splitting and printing is illustrated in **Figure 5.1.2 A**. It starts similarly to previous work on printing aqueous gold nanorods [81]. The nanorods diffuse into the beam of a focused laser, resonant to their longitudinal plasmon modes. Optical torque can begin aligning metallic antennas parallelly to the laser polarization axis [86, 87]. With the laser focused onto a substrate, they can then be printed by optical force [219]. The difference between GNR reshaping and more traditional optical GNR printing with a 1064 nm laser lies in the powers used. Rising laser intensities deliver geometries increasingly divergent from rods. Exemplary results of the power dependent optical printing processes are depicted in **Figure 5.1.2 B**.

Dimerization of GNRs was observed at laser powers ≥100 mW [56, 214]. Resulting dimer antennas were found to consist of ~40 nm gold spheres by SEM. Crucially, dimer printing appeared to take place ~1 µm below the laser beam focus. Shifting the laser beam focus from the substrate was thus a requirement. The dimers were aligned parallelly to the laser polarization in terms of their long axes, with a standard deviation of 45°. Positionally, printing was observed to lie within ~1 µm of the laser focal axis, by camera. Dimer volume (~$6.7 \cdot 10^5$ nm^3) was similar to that of a single 25 × 137 nm GNR. It features $6.7 \cdot 10^5$ nm^3 or $6.3 \cdot 10^5$ nm^3, when modelled as a full 25 × 137 nm or a spherically endcapped cylinder respectively. This indicates that dimers stem from GNRs which are split in half. Understanding this light driven process can begin by examining GNR reshaping at lower laser powers.

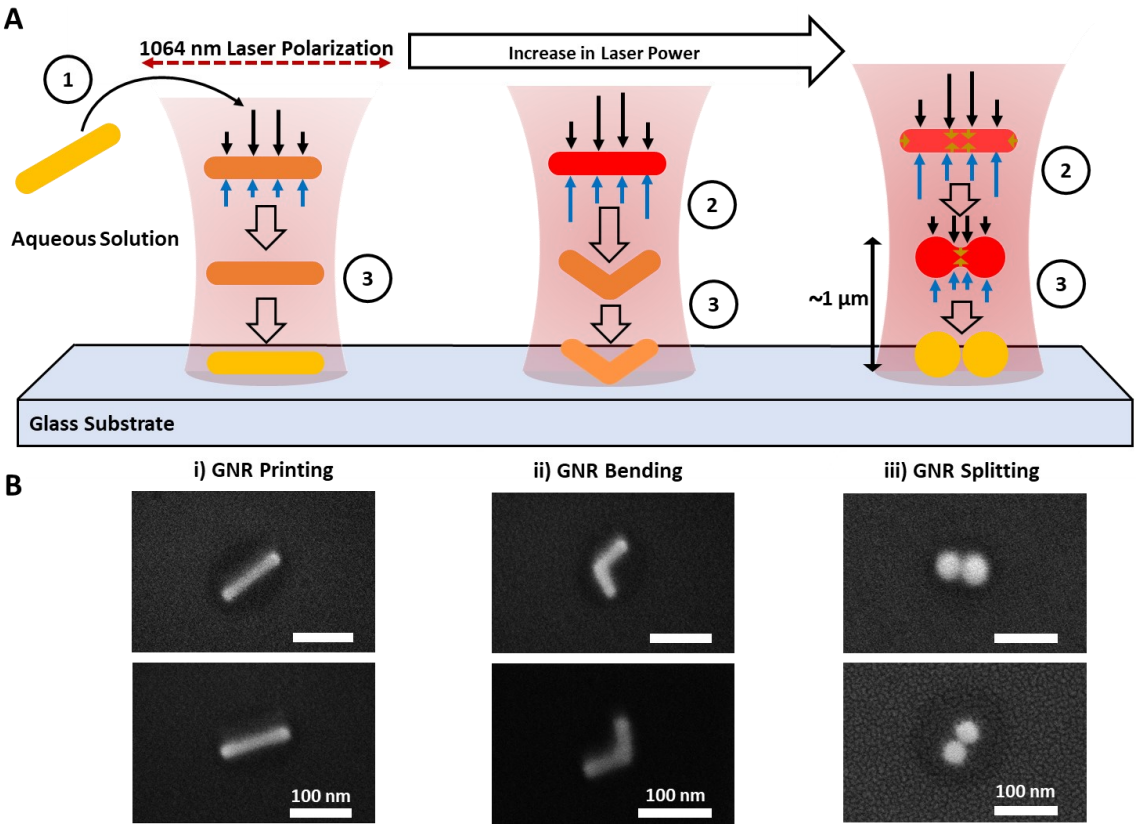

Figure 5.1.2: Gold Nanorod Printing, Bending and Dimerization with Light. A Sketch of different GNR printing outcomes with rising laser powers, beginning with GNRs in aqueous solution diffusing into the laser beam. Here, they experience plasmonic heating (illustrated by discoloration from golden to red), differential optical load (solid black arrows) and differential hydrodynamic forces (blue arrows), as well as Rayleigh instability mediated reshaping (golden arrows), whilst being printed (hollow black arrows) through the laser beam. They can thus either be printed, at the lasers focus, as GNRs (**i**) with a laser power of 10 mW, or bent (**ii**) with a power of 25 mW, or split into a dimer (**iii**) with ≥100 mW of power. **B** SEM images of different laser power dependent GNR printing outcomes corresponding to A.

For laser powers on the order of 10 mW (illumination intensities in the region of 1 MW/cm^2), Babynina et al. found that GNRs could be bent before being printed [98]. Plasmonic heating [220] alone, to elevated steady state temperatures, cannot explain this effect. These might instead lead to spheroidization of the GNRs [221]. Therefore, whilst plasmonic heating might weaken the particles structurally, an additional bending force is required here. It will be discussed in the following.

A bending moment acting on the GNRs was attributed to differential optical load [89], as well as hydrodynamic force [98]. The first component is depicted in **Figure 5.1.3 A**. Here optical load, defined as force per unit length, acts strongest at the centre of the GNR. Integrating these loads $\boldsymbol{q}$ over the length of the rod L results in a total optical force $\boldsymbol{F}_{opt.} = \int \boldsymbol{q} dL$ acting on the particle. It can be employed for simulating interactions of the GNR with its liquid environment. For calculations, total drag force was obtained by integrating pressures p in propagation direction z over the GNR surface S in propagation direction z with $\boldsymbol{F}_{drag} = -\int p\hat{\boldsymbol{n}}_z dS$. It was matched with total optical force in FEM calculations, resulting in a velocity of 0.35 m/s in the laser focus.

Results for hydrodynamic pressure are depicted in **Figure 5.1.3 B**. As can be seen, drag is strongest around the tips of the GNR and weaker at its centre. Combined, these differential forces introduce a bending moment to the nanorod by effectively pushing downwards at its centre and upwards at its ends. This can explain GNR bending with light.

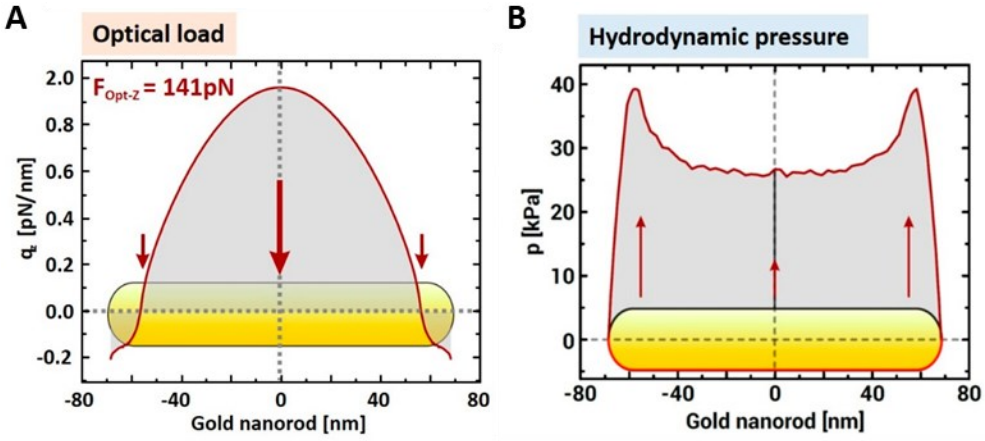

Figure 5.1.3: Differential Forces acting on GNR during Splitting Process. A Optical load q_z acting on a GNR in the focus of a 100 mW power laser. Optical force acts along the arrow directions. F_{Opt-z} denotes the total force acting on the nanoparticle. **B** Hydrodynamic pressure profile along the bottom of a GNR pushed through water by the optical force depicted in A. Drag force acts along the arrows. The particles was aligned in parallel to the laser polarization and perpendicularly to the flow direction of water. Optical forces were calculated with FDTD (see **Section 2.2.3** and **3.2.1**) [214]. Hydrodynamic interaction was simulated with FEM for the Navier-Stokes equation for noncompressible fluid under mass conservation [214]. Adapted with permission from [214]. Copyright 2023 American Chemical Society.

Again, higher laser powers (≥100 mW) were then found to split the GNRs and print resulting double spheres onto a glass substrate. On its own, the bending moment acting on GNRs, during the optical printing process, would imply further kinking and possibly a break at the centre, into two shorter nanorods. Therefore, further effects must be involved.

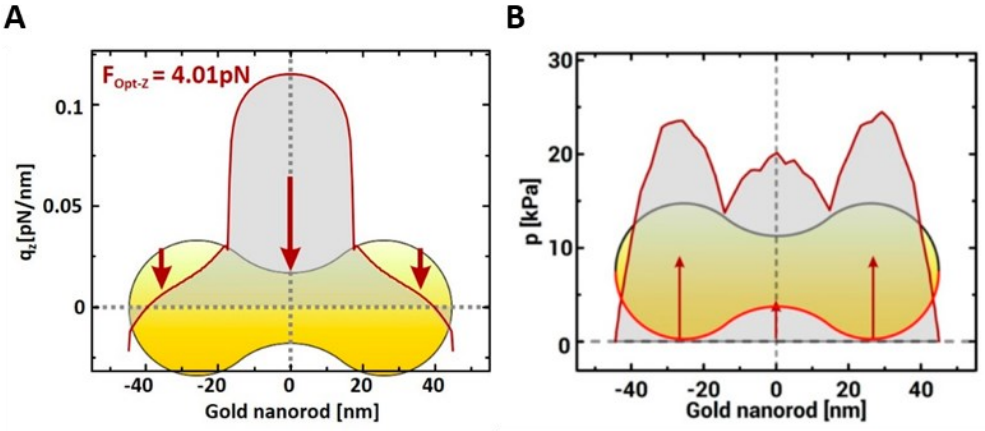

Figure 5.1.4: Differential Forces acting on Dumbbell during Splitting Process. A Optical load q_z acting on a dumbbell in the focus of a 100 mW power laser. Optical force acts along the arrow directions. F_{Opt-z} denotes the total force acting on the nanoparticle. **B** Hydrodynamic pressure profile along bottom of a dumbbell pushed through water. Drag force acts along the arrows. The particle was aligned in parallel to the laser polarization and perpendicularly to the flow direction of water. Optical forces were calculated with FDTD [214]. Hydrodynamic interaction was simulated with FEM [214]. Adapted with permission from [214]. Copyright 2023 American Chemical Society.

One key mechanism identified behind this GNR dimerization is (Plateau-)Rayleigh instability [222, 223]. It was first reported on by Plateau and Lord Rayleigh, in 1873 and 1878 respectively, in the context of liquid columns and jets disintegrating into droplets due to capillary forces. Such principles of surface area (to volume) minimization were also found applicable to gold nanowires, forming chains of droplets when heated to 500°C [152]. However, according to previous reports on cylindrical rods, minimum aspect ratios for bispheroidization are 7.2 [224], whilst the GNRs employed here have a length to width quotient of ~5.5. This supports that additional factors are at play. These were identified as differential optical and hydrodynamic forces acting not only on the GNRs, but also on their transition phases as dumbbells [56]. Such forces are illustrated with **Figure 5.1.4 A** and **B** respectively. These forces also induce a bending moment, by pushing strongest at the centre optically, and resisting strongest around the ends hydrodynamically. This might lead to dumbbell kinking and finally splitting in the middle. The heated halves could then fully spheroidize via surface tension.

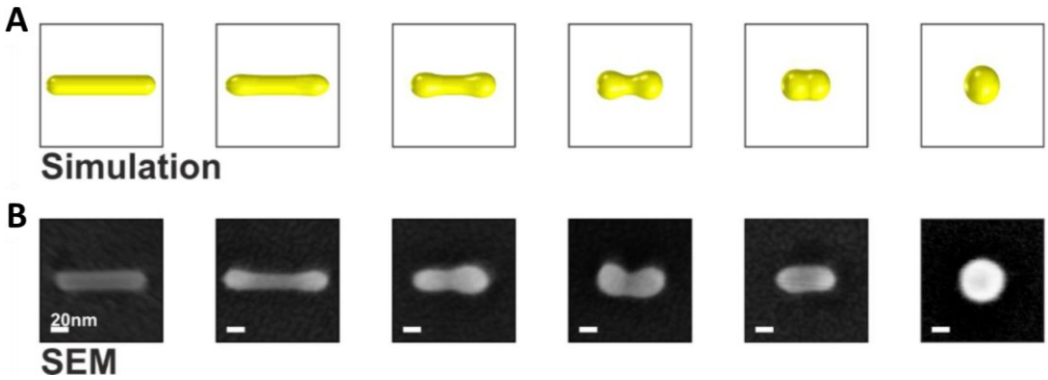

Figure 5.1.5: Static Melting of GNRs. A FEM (*COMSOL*) simulation of GNR melting without optofluidic forces, via a nanorod shaped liquid droplet relaxing under surface tension. **B** SEM images of GNRs on glass substrates reshaped by plasmonic heating through laser excitation. NIR (1064 nm) laser powers used for heating (100 mW) corresponded to those in optical printing and splitting experiments. Reprinted with permission from [214]. Copyright 2023 American Chemical Society.

The necessity of optofluidic force contributions in dimerization is further supported by results of static GNR melting [56, 214]. Here, immobilized GNRs allowed for analyzing more isolated effects of heating, by suppressing and counteracting hydrodynamic as well as optical forces (in the printing direction). Results of simulations and experiments are shown in **Figure 5.1.5 A** and **B** respectively. In the case of experiments, intermediate melting states were achieved from random variations in GNR orientation (against polarization) and positioning (from focus) in the laser leading to different heating powers. Here, reshaping was arrested at different stages, by plasmon resonance shifts away from the laser wavelength (leading to reduced heating). Both calculations, as well as experiments on static GNR reshaping featured dumbbell states during spheroidization of the nanorods, indicative of Rayleigh instability. However, dimerization was not induced. Instead, the GNRs were molten into single spheroids. Other work on stationary gold

nanoantennas with an aspect ratio of 8 (50 × 400 nm), heated with fs pulsed NIR light, also revealed incomplete dimerization [225]. Therefore, both Rayleigh instability, as well as optofluidic forces appear vital for splitting GNRs into GNS dimers with light.

Here, to increase dimer yield on glass substrates, these were plasma treated, prior to experiments. This was necessary as, at a water interface, fused silica displays dissociation of silanol groups leading to a negative substrate surface charge [226]. In contrast, CTAB – which is adsorbed to the GNRs, where it forms bilayers – is positively charged in water. As such, it prevents aggregation of the nanoparticles, but also causes them to adsorb to glass substrates. To prevent this, substrates were plasma functionalized (with air), to give them a positive surface charge, prior to experiments. This was done for 2 minutes with a *Harrick PDC-32G-2* plasma-cleaner. Additional CTAB was added to the solution, via 1 µl of aqueous solution at a concentration of 1 mM, to raise positive surface charging and electrostatic repulsion. For silicon nitride Si_3N_4 in aqueous solution surface potential is pH-dependent (positive in an acidic and negative in a basic environment) [227]. Plasma treatment was also conducted for the Si_3N_4 substrates to ensure positively charged surfaces, and was found to be successful in hindering adsorption of GNRs.

With this, further GNR splitting, and dimer printing was conducted experimentally. The size of potential gaps, and their use for SERS, are the subject of this work's following subchapters.

5.2 Approximating the Dimer Gap Size

SEM images of optically split gold nanorods, as presented in **Subchapter 5.1**, depict two adjacent spheroids (**Figure 5.1.2 B**). When viewed from a perspective of electromagnetic enhancement two key questions arise: Firstly, whether these dimers feature gaps and secondly, how large such potential plasmonic nanoagent hotspots are. Answers to these questions are the subject of this subchapter.

Besides SEM imaging resolution, another inhibiting factor to the method for identifying plasmonic gaps is the necessity of conductive substrates. Nanodimers printed onto glass substrates for DF-scattering (including basic visual confirmation of printing) and SERS experiments, had to be sputtered with an nm-thick conductive gold-palladium layer (**Section 3.1.2**). This potentially obscures nanoscopic interparticle gaps. The necessity of sputtering was avoided by printing dimers onto conductive silicon nitride membranes, suitable for higher resolution transmission electron microscopy.

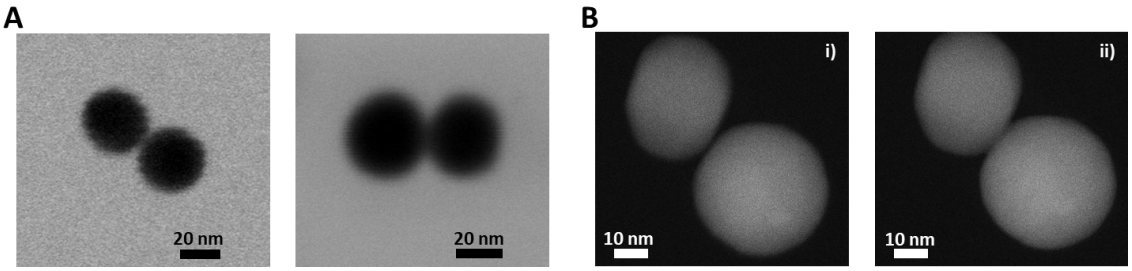

Figure 5.2.1: TEM Imaging of Intradimer Gap. A Exemplary T-SEM (30 keV) images of dimers, with limited resolvability of gaps. **B** Consecutive high-resolution HAADF-STEM images of dimer. Image **i**) was followed by image **ii**), with the later taken after more electron beam exposure. B: Adapted with permission from [214]. Copyright 2023 American Chemical Society.

The presence of gaps is strongly suggested by scanning T-SEM measurements depicted in **Figure 5.2.1 A**. The images also clearly show the spheroidal nature of the dimer halves. Small, potentially threadlike, connections between them can however not be excluded. To confirm gaps between the dimer spheres more absolutely, high-resolution (HR) TEM was conducted (**Figure 5.2.1 B**). Here it was found that the 300 keV electron energy beam melted the dimer together at the gap. Whilst a gap presence could be confirmed, its span was however not measurable with atomic resolution. HR-TEM was also not conductible in a statistically significant manner.

Thus, to approximate gap sizes, scattering spectra of optically generated dimers printed onto glass substrates were acquired in water. These spectra could then be analyzed for bonding dipolar mode resonances, in light of plasmon coupling. Printed (potential) dimers were preliminarily identified by their bright whitish color with DFM as shown in **Figure 5.2.2 A**. These spots were subsequently targeted for acquiring DF scattering spectra. Afterwards, potential dimer geometries were analyzed via SEM as shown in **Figure 5.2.2 B**. Here not all whitish spots proved to match dimers. However, in general yields of up to ~40% were achievable in terms of all printed particles.

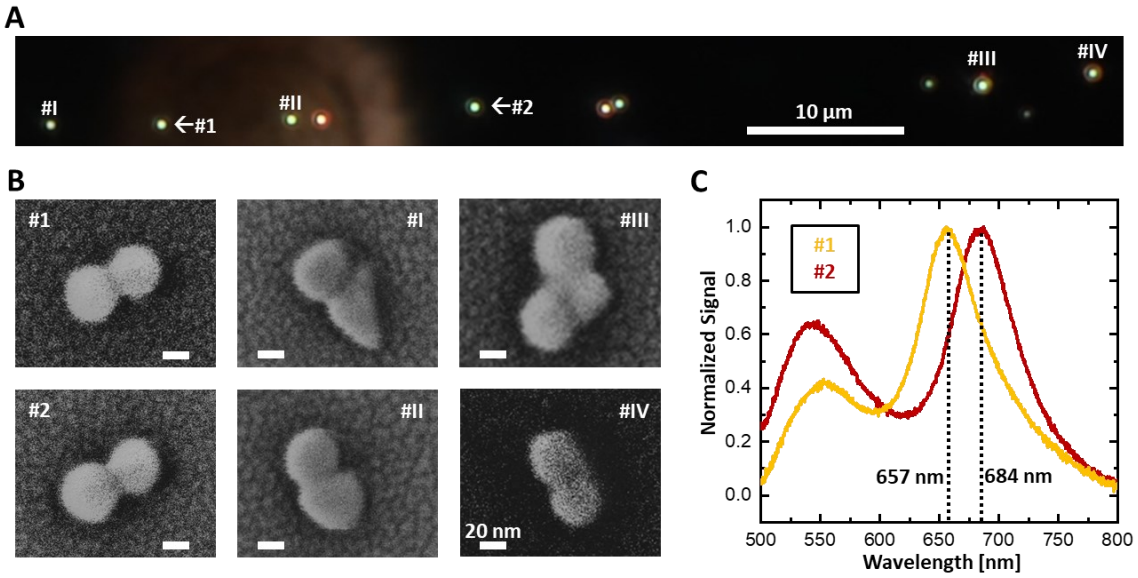

Figure 5.2.2: BDP Resonance for estimating Gap Length. A DFM image of line of printed antennas with identification markers. **B** SEM images of printed antennas in A. Here #1, #2, #II and #IV were identified as GNS dimers, whilst #I and #III were not. Scale bars are 20 nm in size. **C** Exemplary scattering spectra of two of the dimers, with indicators of BDP peak location. Adapted with permission from [214]. Copyright 2023 American Chemical Society.

Next scattering spectra could be evaluated with examples for dimers confirmed via SEM depicted in **Figure 5.2.2 C**. Here, the longitudinal red BDP modes dominate. Peaks around 550 nm might correspond to a combination of higher order (bonding) quadrupolar [76] - and transversal plasmon - modes. Analysis of the BDP peak was then carried out for further printed dimers.

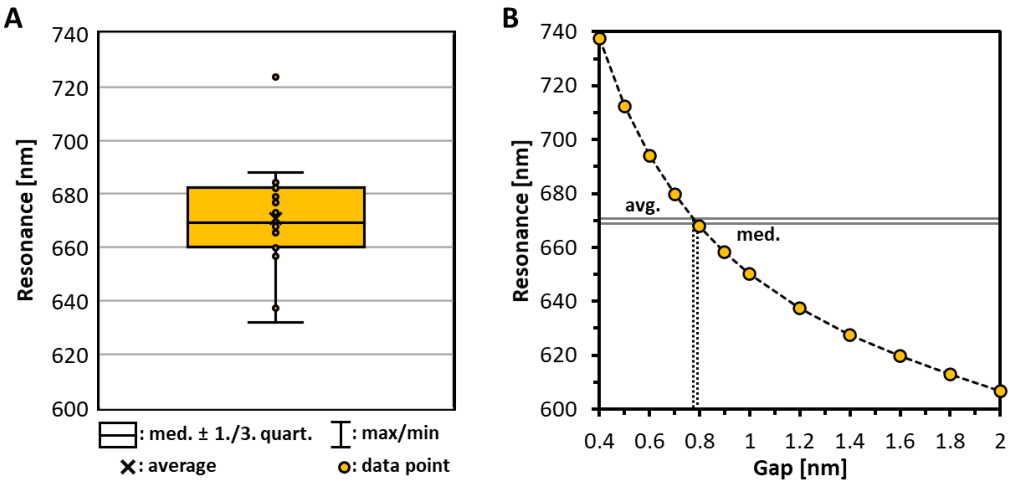

Figure 5.2.3: BDP Resonance for estimating Gap length. A Boxplot of bonding dipolar plasmon peak position in water of 17 dimers (determined via SEM), with legend. Average resonance was located at 671 nm (with a median of 669 nm, and one outlier). This corresponds to a gap of ~0.8 nm according to calculations in B. **B** BDP resonance wavelength for interparticle gap span according to FDTD simulations of dimers on glass, in water. Here, grey, and dashed lines match average and median resonances to gaps respectively. Calculations in B were conducted with longitudinal excitation and 5 nm spectral resolution, with resonances determined by Lorentzian fitting. Adapted with permission from [214]. Copyright 2023 American Chemical Society.

A statistical analysis of GNS dimer BDP mode resonance is shown in **Figure 5.2.3 A**. Here a plasmon resonance around 670 nm was found. This presents a significant red-shift from single or uncoupled gold nanosphere plasmonic resonance under similar conditions, which lies around 530 nm (**Section 2.2.1**). To approximate how gap size and resonance are linked, FDTD calculations were performed, which are shown in **Figure 5.2.3 B**. Qualitatively, again, smaller gaps lead to stronger coupling and greater red-shifts of the longitudinal plasmon mode.

A direct comparison between experiments and classical simulations on the BDP mode yields a dimer gap length around 0.6-1.4 nm, skewedly distributed around a mean of ~0.8 nm. For such angstrom scale distances, the question arises whether quantum mechanical electron tunneling effects might have to be considered. These are the subject of a number of studies on metallic dimers in air/vacuum, not limited to the following, of both of a theoretical [76, 78, 228], as well as an experimental [215, 229, 230] nature. Here, more specifically, according to calculations Esteban et al. [76], an additional longitudinal (quantum tunneling) charge transfer plasmon (CTP) was only clearly observable as of ~0.1-0.2 nm of separation (in vacuum). Electron tunneling is also not a (major) detrimental factor to the BDP mode (in terms of red-shift and intensity) up until around 0.3 nm. A similar value for screening of the BDP mode was found experimentally by Savage et al. [229]. At the same time, the BDP mode can blue-shift shortly before contact of the dimer halves, as, again, found both in theoretical [76, 78, 228] and experimental [229] work. Despite differences in parameters, including an aqueous instead of air/water environment, a similarly V-shaped relationship between gap length and resonance energy, could thus be presumed here.

Therefore, the question whether the 671 nm average resonance might (partially) stem from a suppressed bonding plasmonic mode, with a significantly smaller gap than 0.8 nm, does come to mind. Nonlocal effects would then be more considerable, corresponding to further reduced actual compared to calculated gap spans [78, 79]. Besides HR-TEM imaging results, two other arguments speak against this. The first is linked to E-field enhancement within the gap. It would be suppressed (together with the BDP mode) by electrical contact for significantly shorter gap spans. Instead, it can be exploited for SERS, described in the next subchapter. The second relates to forces involved when printing the dimers. It is discussed in the final subchapter.

5.3 SERS of NTP

The previous subchapter serves to discuss the existence and size of gaps between the GNSs constituting dimers created by optical splitting of GNRs. This subchapter focuses on the potential uses of such gaps in generating E-field and thereby Raman enhancement. To do so, dimers printed onto glass substrates and submerged in water, were functionalized with 4-nitrothiophenol (NTP). This was done by adding 10-30 µl of ethanol containing NTP at a 1 mM concentration. This corresponded to a concentration of 0.09-0.23 mM NTP in the solution. The molecules could then adsorb to the gold nanoantenna surfaces via thiol bonds, with the attached molecule illustrated in **Figure 5.3.1 A**. Such samples could then be blow dried and resubmerged in water for further analysis with a DFM setup.

Potential dimer antennas were identified by their whitish color, and then irradiated with circularly polarized 671nm laser light. Here a power of 0.2 mW was used to generate SERS. This relatively low power was chosen to avoid altering the nanoparticles and analyte by plasmonic heating. Dimeric properties were confirmed after these optical experiments by SEM. An example of for such a dimer is given in **Figure 5.3.1 B,** with corresponding SERS signal in **Figure 5.3.1 C**. Here distinct peaks were found at 1070 cm^{-1} – corresponding to ring C-H bending, 1320 cm^{-1} – matching symmetric NO_2 stretching, and 1570 cm^{-1} – for C=C stretching of the aromatic ring, in accordance with literature [231, 232]. The sharpness of the peaks indicates that carbonization and cross linking of the adsorbate molecule did not play a major role here. In particular, the spectrum also lacks significant SERS signal peak broadening around the aromatic ring mode at 1570 cm^{-1}, which has been measured for carbonized thiophenol [164].

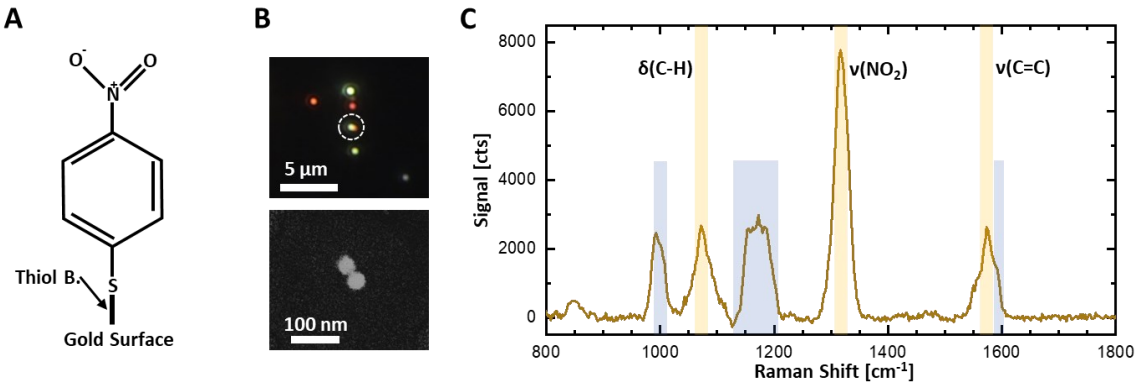

Figure 5.3.1: Dimers for SERS of NTP. A Sketch of a 4-nitrothiophenol molecule with thiol bond to gold surface. **B** DFM image of exemplary dimer (circled whitish spot) and SEM image of same dimer. **C** Background subtracted SERS spectrum from dimer identified in B, with labelled NTP Raman modes highlighted in gold, and potential ATP (and DMAB) signal highlighted in blue. The spectrum was acquired with a 25s integration time. Raman peak assignment is featured in **Table 3**. B and C: Adapted with permission from [214]. Copyright 2023 American Chemical Society.

What was however observed, was additional Raman signal at 1000 cm^{-1} and around 1170 cm^{-1}. Here, it might correspond to 4-aminothiophenol (4-ATP) at 1000 cm^{-1}, and 1170 cm^{-1}

[233, 234], as well as dimercaptoazobenzene (DMAB) at 1000 cm^{-1}, 1144 cm^{-1} and 1185 cm^{-1} [234, 235]. The presence of ATP can be explained by a hot electron induced reduction of NTP [235], where the NO_2 group is reduced to NH_2. ATP generation would also match the peak shoulder, around 1590 cm^{-1} [233-235], of the NTP C=C aromatic ring stretching mode (1570 cm^{-1}). DMAB on the other hand is a possible intermediate state in an NTP to ATP reaction pathway, where two NTP molecules are joined via an N=N bond [235]. Corresponding reactions might also have been assisted by plasmonic heating.

Table 3: NTP Measurement Raman Peak Assignment.

Peak Positions [cm^{-1}]	Raman Peak Assignment
1000	ATP [233, 234], DMAB [234, 235]
1070	NTP [231, 232] ring C-H bending
1144	DMAB C-N vibration [234, 235]
1170	ATP C-H bending [233, 234]
1185	DMAB C-H bending [234, 235]
1320	NTP symmetric NO_2 stretching [231, 232]
1570	NTP ring C=C stretching [231, 232]
1590	ATP ring C=C stretching [233-235]

Here, it should also be noted, that 671 nm does correspond to resonance Raman in the case of NTP, for all three of its main characteristic modes [232]. This boosts Raman cross sections significantly to $\sim 10^{-25\text{-}26}$ cm^2. On the one hand, no clear SERS signal was detectable for non-dimerized GNR structures as side products of the laser printing and reshaping process. On the other hand, 15 out of 16 (94%) dimers (structurally confirmed by SEM), yielded NTP Raman. In these cases, a rate of detected counts in the region of $10^{3\text{-}4}$ s^{-1} per (background subtracted) main (NO_2) peak was observed. This is considerable and indicates strong electromagnetic enhancement from the dimer hotspots.

CTAB Raman signal, with most prominent peaks (from CH_2 and CH_3 deformation) at 1450 cm^{-1} [236], was not distinctly observable. This suggests that the ligands were stripped from the metallic nanoparticles due to plasmonic heating in the optical splitting process. They might also have decomposed at temperatures exceeding 200-250 °C [237], which is significantly below golds bulk melting point and temperatures reached during the dimerization process. Readsorption of some of the free CTAB ligands from the printing solution to the dimer GNSs can however not be excluded. In particular, as their Raman cross sections might be significantly smaller than those of NTP, making it difficult to detect with SERS. Additionally, the molecule which forms 3.6 nm bilayers on gold nanoparticles [238], might not fit into the dimer gap, where Raman enhancement is highest. Therefore, whilst potentially present, CTAB does therefore not appear to hinder the use of these dimers for SERS detection here.

According to calculations presented in work by Esteban et al. [76, 228] E-field enhancement factors for 40 nm bispheres in vacuum are in the region of 10^3, at the centres of 0.8 nm gaps. Such E-field enhancement factors are sustained from roughly 1 nm until 0.2-0.3 nm distances. Below these, electron tunneling suppresses field enhancement in the hotspot. The effect is explainable by electron tunneling lowering charge displacement around the nanosphere gaps. Further experimental work in air by Zhu et al. [215], corroborates this. It showed a Raman enhancement factor of $1.2 \cdot 10^9$ for 90 × 20 nm (width by height) gold disc dimers distanced by 0.67 nm, which was suppressed to $2.4 \cdot 10^8$ for a 0.20 nm gap.

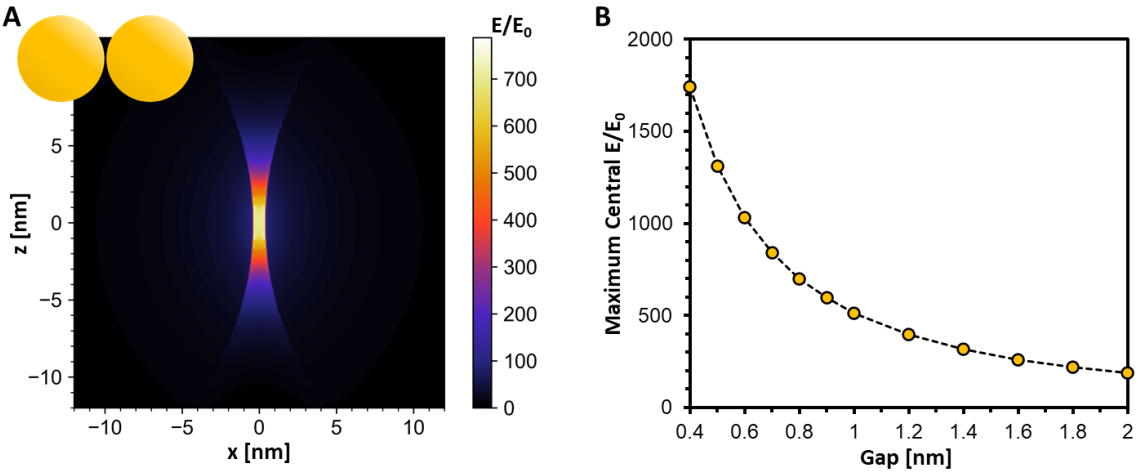

Figure 5.3.2: Classical E-Field Enhancement in Gap. A Maximum E-field enhancement map (at 663 nm) for a 40 nm GNS dimer with a 0.8 nm gap. **B** Maximum E-field enhancement at centres of dimers with varying gap spans. Calculations were performed with antennas on glass, in water. Calculations in B were conducted with 5 nm spectral resolution, with Lorentzian fitting at the peak to determine maximum enhancement.

Here, in aqueous solution, classical calculations indicate that peak field enhancement factors are relatively high, reaching ~700 for 0.8 nm gaps displayed in **Figure 5.3.2 A**, albeit confined to a small part of the hotspot. In general, they were calculated to be in the region of ~300-1000 for the centres of experimentally achieved ~1.4-0.6 nm gaps, as depicted in **Figure 5.3.2 B**. This implies significant EF^4 Raman scattering enhancement factors of ~10-12 orders of magnitude. In air at least, suppression of this Raman enhancement via quantum tunneling would not be expected. Additionally, the small gaps might have led to particularly strong image dipole enhancement (touched upon in **Section 2.1.2**). This could have contributed to identifiable SERS as well as significant signal background. These aspects support the strong Raman signal observed, and that this type of dimer does in fact feature freely accessible hotspots open to sub-nm diffusive analyte. Here, a remaining question is whether the aforementioned E-field enhancement might not be at least partially quenched by quantum tunneling in water. This is addressed in the following subchapter, which focuses on what might cause and determine the sizes of these hotspots.

5.4 Dimer Gaps and Optical Forces

A further important question that arises, is why ~sub-nm gaps should exist between the printed spheroidized GNR halves. Instead, GNSs could be expected to drift apart via Brownian motion. An explanation can be sought in DLVO theory [239], named after Derjaguin, Landau, Verwey and Overbeek. It describes the force between surface charged particles in a liquid medium. Here, van der Waals attraction is combined with surface charge effects. The latter includes repulsion via charged ligands which can be screened by an electrical double layer of counterions. Positively charged ligands might be present here, in the form of free CTAB, attaching to the dimer GNS from solution after GNR splitting. The use of deionized water in experiments does however suggest that screening of surface charges by ions is not a major factor. Overall, the exact contribution of CTAB is difficult to quantify here. On its own, the surface charge effect could be expected to cause gaps of at least 2 CTAB bilayer widths, or ~7 nm, which is significantly larger than experimental observations. Therefore, van der Waals forces might have overcome electrostatic repulsion. These attractive forces from fluctuating polarizations, can become particularly significant for small distances. For sub-nm gaps between metallic nanoparticles, potential energies have been calculated to reach and exceed eV (~40 $k_B T_R$) depths [240-242]. Further, for particularly small distances between nuclei (~0.4 nm for gold [243]) van der Waals repulsion comes into play.

For one, these forces appear difficult to quantify for the GNR dimerization case, also due to the unknow impact of CTAB. It is thus unclear how they might lead to ~0.8 nm GNS gaps. What might be excluded however, is that gaps are determined by van der Waals forces alone. These would be expected to further shrink gaps significantly. Therefore, here, an additional factor is explored, namely optical forces between the plasmonically hybridized particles, driven by the NIR laser during the printing process. According to Tong et al. [91], it can contribute significantly to potential landscapes according to DLVO theory, between citrate capped gold nanospheres.

A number of studies have looked into optical forces for arranging metallic nanoparticles in a patterned manner by optical binding [244-246]. Here, both attractive gradient forces pulling plasmonic particles into the laser beam as well as forces between particles, resulting in periodic potentials, have been exploited. In general, these led to interparticle distances in the region of the excitation wavelength. However, an additional regime, where particles were spaced significantly closer together, was also achieved by Yan et al. [244]. For this, silver spheroids had to approach one another, with a dimer axis aligned somewhat in parallel to the excitation laser polarization. Similar conditions might be expected for the spheroidized halves of optically split GNRs examined in this thesis. In the 2014 study ([244]), a deep attractive binding potential was observed. Spacing between the particles was found to then be determined by electrostatic

repulsion of a polymer coating. For such close proximities plasmonic dipole-dipole coupling is thus significant.

Other studies have focused further on attractive dipole-dipole coupling forces, between plasmonic nanoparticles in proximity to one another [90, 91, 247, 248]. In particular, Svedberg et al. [248] have managed to exploit this for SERS of thiophenol from silver nanospheres in solution coupling with nanoparticles on a substrate. To do so the nanoparticles were coated with analyte molecules and optically bound to one another with an 830 nm laser. A separate 514.5 nm laser was then used simultaneously for measuring SERS in the 2006 study ([248]). Such forces therefore appear highly relevant for optically assembled dimers here.

Attractive dipole-dipole force does however become ever stronger for shrinking gaps. For nanospheres stripped of surfactants, during the GNR splitting process, gaps would then be closed. This was however not observed. Merging of spheres was also avoided under optimal experimental conditions. Therefore, an additional effect might have come into play. Here, a prime candidate is GNS collision (which will be revisited later). It in turn goes hand in hand with electrical contact between the two particles. The effect is illustrated in **Figure 5.4.1 A**, with conductivity established by overlapping of the dimer halves.

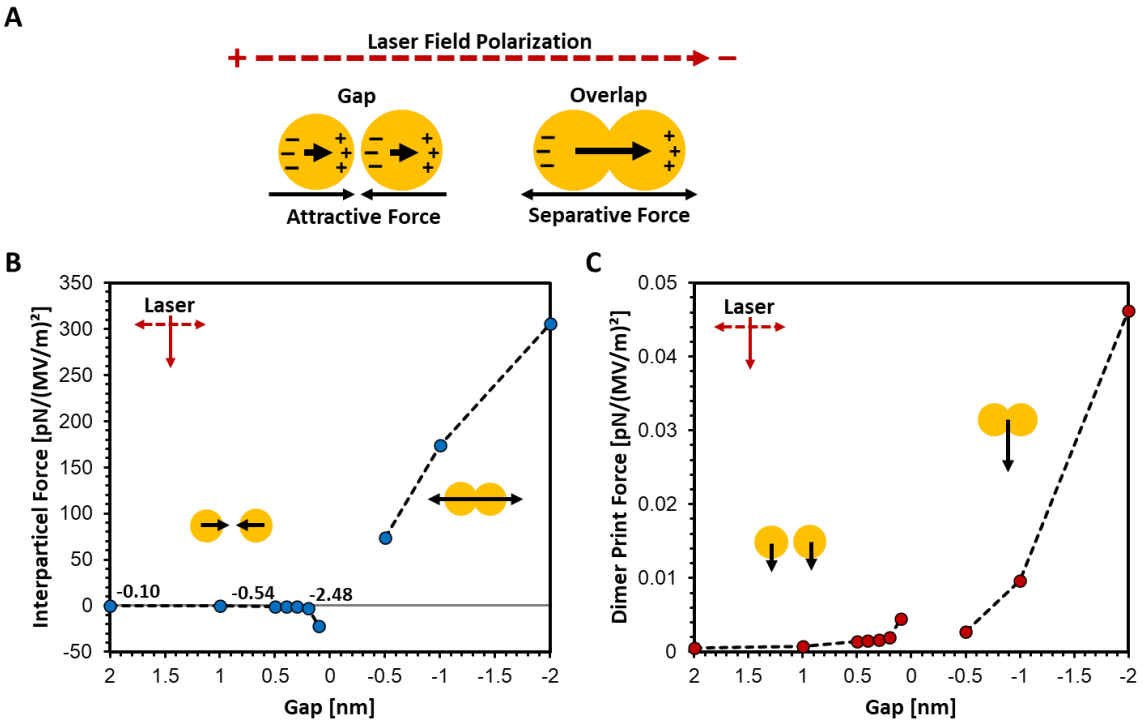

Figure 5.4.1: Classical Intradimer Forces. A Sketch of charge distributions and forces involved for GNS dimers in the NIR laser field. Thick black arrows represent dipole orientation. **B** Classically calculated intradimer force during laser printing process, with gap/overlap dependence. **C** Classically calculated dimer printing force. Calculations were performed with homogenous excitation. Overlaps could not be shrunken infinitesimally, to more accurately model 40 nm GNS touching, due to lack of simulation convergence, possibly due to the sharp geometrical cross sections involved. Actual laser fields involved in the printing process were on the order of ~10 MV/m (or ~100 $(MV/m)^2$).

For particles in electrical contact opposite charging at the intradimer junction is suppressed. The dimer thus becomes a single dipole, were charge displacement is most pronounced at the ends. As a driven oscillator, the precontact dimer dipole is blue-shifted in resonance from the 1064 nm laser via the BDP mode. Averaged over time, it is thus polarized more parallelly than anti-parallelly to the light field, meaning a positive polarizability. For the electrical contact dimer in a laser spot, this might also be the case. The dimer GNSs could then be pulled apart, via their opposing net charges. The optical forces involved between separate and merging/overlapping gold nanospheres in water can be calculated classically using FDTD, with results shown in **Figure 5.4.1 B**. Calculations confirm the hypothesis. Here, attractive forces are particularly large for small gaps, whilst separative forces increase for larger overlaps. Proximity between dimer GNSs can be expected to increase attraction between the two. Additionally, for printing forces depicted in **Figure 5.4.1 C**, a similar pattern is observed, with higher printing forces for smaller gaps and larger overlaps. A higher force indicates an increased interaction cross section of the antennas, potentially also from plasmon resonances more closely matching the laser wavelength. This force has proven sufficient for printing dimers below the lasers focus in experiments, whilst being significantly lower than calculated interparticle forces. Interparticle force therefore appears to be of importance in the optical dimer patterning process.

Here it should be noted that nonlocal effects were not considered. Rescaling corrections for gap lengths, as have been performed in vacuum [78, 79], could increase the accuracy of such classical results. Nevertheless, these calculations support that classical electrical contact will induce separating forces. However, at least on their own, they cannot explain how ~0.8 nm intradimer gaps were formed. Classically calculated intradimer forces would turn attractive for any GNS separation. A theory towards how optical forces might contribute to GNS separation is presented in the following.

Due to an onset of electron tunneling for shrinking single angstrom gap dimers, a geometrical overlap is not necessary for electrical contact. This in turn results in separation forces potentially contributing to the measured gap spans. To test this hypothesis, further calculations were conducted for 40 nm gold sphere dimers in water. They are based on a quantum-corrected model (QCM) approach by Esteban et al. (2012) [76]. Here the intradimer gap is modelled with media where $\varepsilon^*(d,\omega)$ describe an effective permittivity, from electron tunneling. This is based on local gap length $d \geq D$, with d measured in parallel to the longitudinal dimer axis and D as the minimum span of the gap. $\varepsilon^*(d,\omega)$ was then implemented in a cylindrical layer system.

For this work, modelling parameters were chosen analogously to later work by Zhu et al. (2014) [215], albeit for an aqueous environment instead of vacuum. Hereby, approximating $\varepsilon^*(d,\omega)$ begins with gold according to the Drude model, but with a modified damping constant γ^*, similarly to **Equation 2.18** via:

$$\varepsilon^*(d,\omega) = \varepsilon_\infty - \frac{\omega_p^2}{\omega^2 + i\gamma^*\omega}. \quad (5.1)$$

With:

$$\gamma^* = \gamma_{gold} \cdot exp(2qd). \quad (5.2)$$

In the vacuum case, ε_∞ = 1 is the background screening contribution of vacuum/air, ω_g = $2\pi \cdot 1.94 \cdot 10^{15}$ s^{-1}, γ_{gold} = $2\pi \cdot 2.14 \cdot 10^{13}$ s^{-1}, and q_{vac} = $1.12 \cdot 10^{10}$ m^{-1}; the latter being an effective decay rate from Zhu et al. ([215]), obtained by a linear fit from full quantum mechanically simulated data from Esteban et al. ([76]). Translating this model to the aqueous dimer case, discussed in this thesis, requires a gap permittivity ε^* to meet two requirements. For one, it has to match that of the surrounding dielectric medium for large d [228]. For this, ε_∞ = ε_{Water}= 1.769 (with a refractive index of ~1.33 for water), is significantly larger than vacuum permittivity. Additionally, the water gold interface is expected to impact the tunneling coefficient, now q_{Aqua}. From the time independent Schrödinger equation, tunnelling suppression and thus q scales with the square root of barrier height [249]. Here, this is the work function of gold in the given dielectric medium and thus:

$$q_2 = \sqrt{W_2/W_1} \cdot q_1. \quad (5.3)$$

From Musumeci and Pollack [250], gold exhibits a significantly lower work function in water than in vacuum, which is implemented here with W_{AuAqua} = 2.26 eV and W_{AuVac} = 5.285 eV. Therefore, from **Equation 5.3** q_{Aqua}= $0.732 \cdot 10^{10}$ m^{-1}. Permittivities $\varepsilon^*(d)$ were calculated for 1064 nm excitation (laser wavelength) with 0.05 nm local gap length d discretization. This is depicted in **Figure 5.4.2 A**, which shows negative d-dependent effective permittivities below ~0.3 nm. This indicates electrical conductivity between the dimer spheres via quantum tunnelling.

These approximations allow for modelling laser driven interparticle forces with electron tunneling effects, which are shown in **Figure 5.4.2 B**. Here an $\varepsilon^*(d)$ was implemented for $d \leq$ 0.55 nm (for a 0.5 nm gap a 1.4% deviation between classical and tunnelling corrected interparticle forces was observed). In a similar way to their classical counterparts (**Figure 5.4.1**), they start of positive, become negative and go towards zero for increasing gaps. A force equilibrium is found at ~0.24 nm separation.

In isolation, such a force curve strongly suggests a bond between the dimer spheroids with an equilibrium gap span. Notably, forces turn positive (repulsive) with the implementation of the first negative $Re(\varepsilon^*)$, at a separation of 0.2 nm. This is significantly smaller than the ~0.3 nm as of which negative permittivities would be expected to play a role in the gap. Modelling with smaller increments in d and more accurately matched effective permittivity layers might therefore influence results quantitatively. Qualitatively, calculated optical intradimer forces do however

imply a binding potential with a stable minimum, coinciding with dimer gap formation in the printing process.

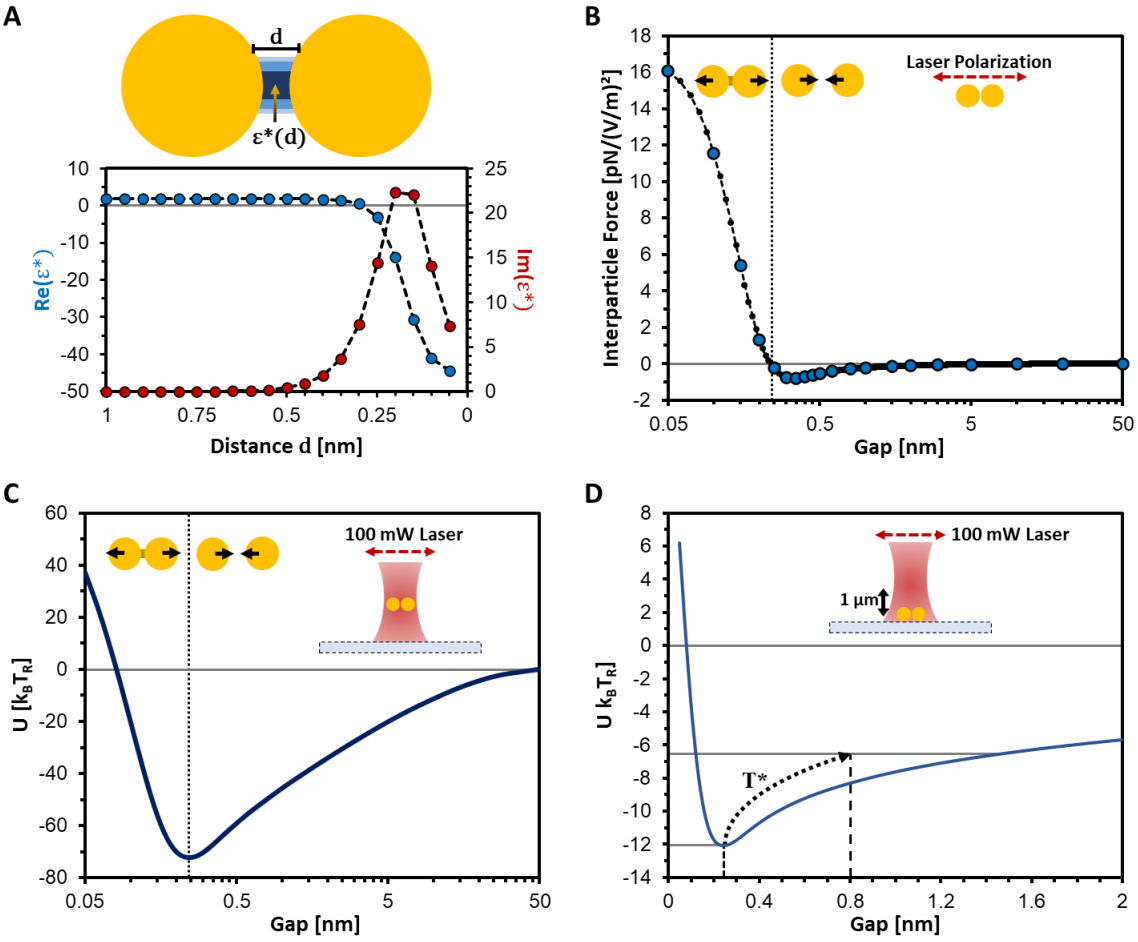

Figure 5.4.2: QCM Approximated Calculations of Optical Force between Dimer GNSs in Water. **A** Illustration of QCM modelling with an $\varepsilon^*(d)$ layer system (not to scale), and calculated distance dependent permittivities. **B** Quantum mechanically corrected combined with classical intradimer forces (blue dots). An additional interpolation (black dots) was carried out with 0.01 nm resolution (assuming 0N at 500 nm as an additional datapoint for the approximation). Modelling was done with a 1 V/m homogenous (TFSF) source with polarization (dashed double arrow) along the long dimer axis, as illustrated by the inset. Gap permittivities were modelled with up to five $\varepsilon^*(d)$ layers for $d_n = D + (n \cdot 0.1 - 0.05)$ [nm]. Starting with index n = 1 for the inner layer and moved outwards with layer radii; 1.4, 2.0, 2.4, 2.8, 3.2 [nm] respectively, to approximate effects of a rising d on permittivities within the dimer gap. **C** Integrated interparticle forces from B with a homogenous laser field amplitude of $1.78 \cdot 10^7$ V/m (100 mW power, at focus). Integration was conducted via summation, with subsequent interpolation. It started at 50 nm of separation. Here, for growing gaps, the isotropic excitation field strengths would increasingly misapproximate the Gaussian focus. Note the logarithmic x-axis might obscure asymptotic behavior. **D** potential energy 1 µm below focus ($7.27 \cdot 10^6$ V/m). The dotted arrow illustrates the effects of anharmonicity. Combining room temperature (T) with loosening of the potential due to position and orientation of the dimer in the laser (*), it can be drawn to extend (by T*) to experimentally observed ~0.8 nm gaps.

To approximate an optically driven intradimer bonding potential energy landscape, corresponding forces were integrated for a 100 mW power in an experimental laser focus. The result is depicted in **Figure 5.4.2 C**. One thing which stands out according to calculations, is that the potential appears positive at gaps smaller than ~0.08 nm. Whilst the model is idealized, does not include non-optical influences, and only reaches 50 nm of separation, this possibility should

still be considered. A positive potential energy would lead to GNS separation. In this case they could however be recaptured by gradient forces of the printing NIR laser, and rehybridize plasmonically. They would then also be optically bound to one another by the laser. Here, in the context of room temperature energies, the interparticle bond strength appears deep at over ~72 k_BT_R. It is also rigid with a fitable spring constant of ~1700 k_BT_R/nm^2 at its minimum. From a laser driven electromagnetic perspective, the dimer spheres would thus be held at a fixed distance at the potential minimum (~0.24 nm) roughly half a gold lattice constant from one another. This is significantly less than the ~0.8 nm finally observed for printed dimers. It is however important to remember, that successful dimer printing was only possible with a laser focus set ~1 µm above the substrate. Even under highest intensity conditions, with dimer location within the radial centre of the beam, the binding potential becomes significantly more shallow. This is shown in **Figure 5.4.2 D**, with a trap stiffness of ~290 k_BT_R/nm^2. At this point, anharmonicity of the potential can begin to play a role, and ~5.6 k_BT_R match the interparticle distance of the experimentally observed gaps. This is significantly above ambient (~T_R) conditions as well as the bulk melting point of gold. On the one hand, this might stabilize the bond between the dimer GNSs against Brownian motion. On the other hand, it also means that the anharmonicity alone cannot suffice to explain the raised gaps according to the optical force model at room temperature. These findings therefore bring up the question to what extent plasmonic heating might be involved.

To estimate the impact of plasmonic heating (for a laser power of 100 mW), the total absorption cross section of a dimer with a 0.8 nm gap in water was calculated to be 40.6 nm^2. 1 µm under the laser focus, at an intensity I = 5.55 MW/cm^2, this corresponds to a heating power of Q = 1.13 µW per sphere. For a thermal conductivity κ ~ 0.6 W/(m·K) of water, and assuming a simplified single sphere heating model in water, $\Delta T = Q/(4\pi kr)$ equals 7.5 K. Whilst not accounting for sphere-sphere-environment thermal interactions, this result is so far below 1 T_R, that heating does not appear significant for explaining a ~0.8 nm gap. Instead, thermal effects appear negligible. Therefore, deviations of the dimer to the laser alignment, numerical aperture, and focal position appear as the most likely contributors to loosening the optical bonding potential.

The following examines examples for aforementioned deviations, in the context of optical forces. Here either an actual focal distance of ~2.5 µm from the substrate, or a beam with an effective numerical aperture of ~0.42 could account for a 0.8 nm gap. Laser beam and focal position especially were however too well controlled for experimentally to explain this. Other types of contributions, namely axial and angular deviation from laser focus and polarization axis, are illustrated in **Figure 5.4.3 A**. They present a suitable explanations for 0.8 nm gaps according to calculations displayed in **Figure 5.4.3 B**. At 100 mW, axial printing deviation of ~770 nm, or

an angular printing deviation of ~65° alone could cause a 0.8nm gap. Particularly combined deviations in printing position and alignment angle appear well within the experimentally observed range. As an example, for an angular printing deviation from the laser polarization, by the observed 45° standard deviation in printing, ~590 nm of axial printing deviation would be sufficient. For larger laser powers, such as 200 mW, a more significant printing deviation of ~910 nm spatially, or 73° angularly would be required for a 0.8 nm gap. Here a combination of the aforementioned factors appears necessary from an optical force perspective.

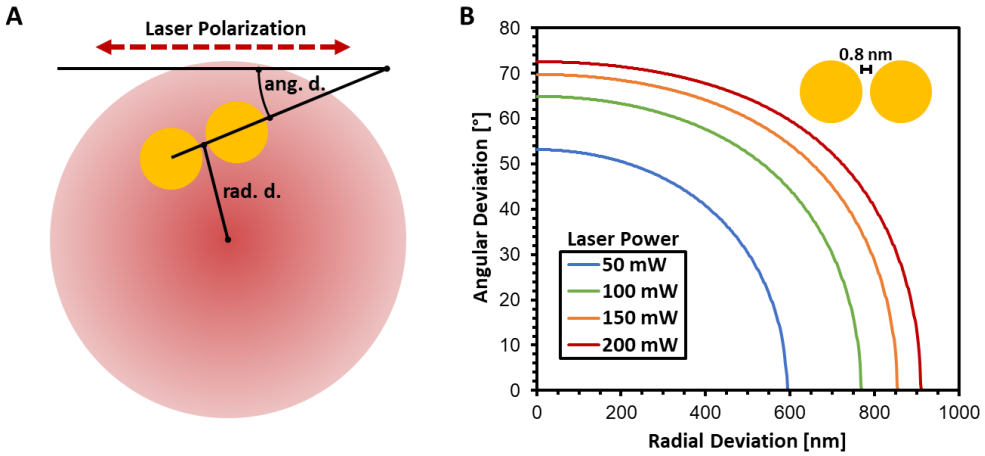

Figure 5.4.3: 0.8 nm Gaps via Alignment of Dimer in Laser. A Illustration of angular deviation (ang. d.) from laser polarization and radial deviation (rad. d.) from laser focus. **B** Angular deviation from laser polarization necessary for 0.8 nm gaps, for a given radial deviation from laser focus, from an optical force perspective. Calculation results are given for different laser powers, 1 µm below the focus.

A printing and alignment deviation induced gap increase alone might explain the observed gap range ~0.6-1.4 nm via the optical potential. Further, the rapid shallowing of the potential for smaller binding energies necessary for larger gaps in **Figure 5.4.2 C** and **D** can help explain why larger gaps were not achievable in a controlled manner via defocusing and lower laser powers in experiments. Instead printing yield was greatly reduced. The dimer might be separated here, and printing forces (**Figure 5.4.1 C**) could be insufficient for printing. Thus, whilst the approximations made might not model dimer printing exactly or completely, the k_BT_R binding energy scale calculated for optical forces appears consistent with experimental results.

Here, it should be noted, that these calculations rely heavily on approximations. For one, spatially more exact values for modelling permittivities in the dimer gaps might be implemented. Also, the model used for fitting permittivities is a simplification, which does not explicitly account for nonlocal effects [77] besides electron tunnelling. Tunnelling is however the dominant effect, whilst others could potentially be implemented [76]. Considering these aspects, would translate to more accurate optically induced potential landscapes.

At this stage, it should also be considered, that collisions of the two gold nanospheres could correspond to a similarly steep potential wall as repulsive optically driven forces, and thus also an anharmonic intradimer bonding energy. However, the optically driven intersphere potential

would deepen significantly, as can be seen from classical calculations of bonding forces for 0.1-0.3 nm gaps in **Figure 5.4.1 B**. Here forces from dipole-dipole attraction unsuppressed by tunneling are ~1 order of magnitude larger than for distances above ~0.35 nm, where the observed maximum bonding force lies. They could then contribute to the potential energy landscape, deepening it significantly. Then, however, positional and angular deviational effects could not exploit thermal anharmonicity significantly, even 1 µm bellow the laser focus. Observed gaps would be significantly smaller, contradicting TEM imaging results. Also, tunneling and electrical contact could again suppress the BDP and SERS mode, which were however both observed. This speaks for quantum tunneling current contributing to a gap. It therefore appears to aid in assembling the dimers with SERS hotspots along with attractive optical forces.

The laser driven anharmonic interparticle potential model is not limited to contributing to an explanation of the observed printing results. It might also offer an outlook on how to tune intersphere gaps of optically assembled dimers. From **Figure 5.4.2 A** and **B**, as well as a conductivity requirement, a negative permittivity appears crucial for establishing repulsive laser driven forces. Larger freely accessible gaps might be desirable for detecting Raman scattering of bigger molecules than NTP, such as diffusive proteins in water. From an optical force perspective, this requires a negative Re[ε^*] for larger distances. **Equation 5.1** gives clear indications as to how to achieve this, along three paths described in the following.

The first way for lowering Re[ε^*] is solvent related. Both a lower work function (thus lowering γ^*, according to **Equation 5.2** and **Equation 5.3)**, and a smaller ε_∞ could lower real permittivities at larger distances. The second is via the nanoparticle metal involved, where less damping and higher plasma frequencies and (again) lower work functions could help. Both options can be expected to influence the metal nanorods plasmonic properties, which would have to be accounted for, especially regarding optical excitation for splitting and printing.

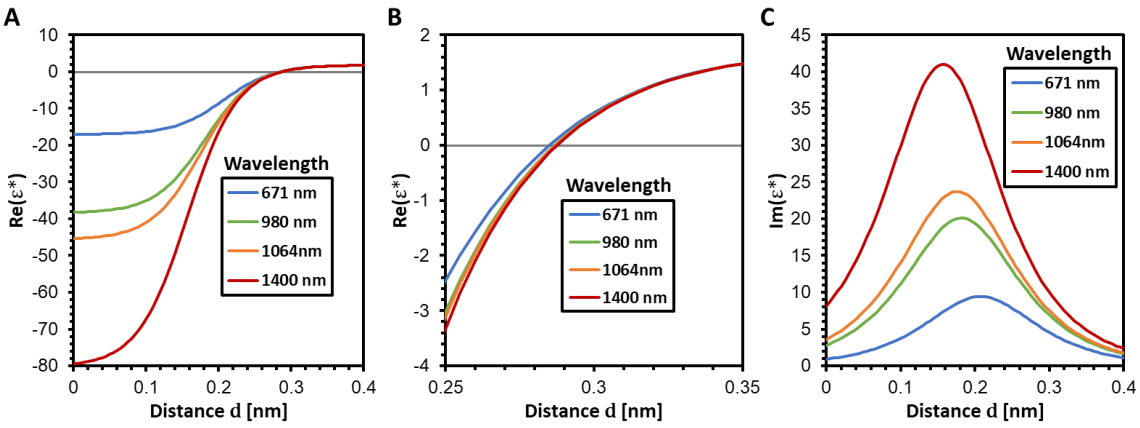

Figure 5.4.4: Wavelength Dependence of Effective Permittivity. A Real part of distance dependent effective permittivities $\varepsilon^*(d,\omega)$ for different wavelengths. **B** Zoom in on real part of distance dependent effective permittivities in A, for values around 0. **C** Imaginary part of distance dependent effective permittivities for different wavelengths.

The third pathway might be the most promising: an increase in the driving lasers wavelength. This can be expected to necessitate higher aspect ratio GNRs to maintain resonance in the splitting process. Such aspect ratios should also further Rayleigh instability in the printing process, increasing the dimer creation probability. However, calculations depicted in **Figure 5.4.4 A** and **B** reveal, that gains in terms of the distance threshold for negative real permittivity are marginal. For example, 1400 nm instead of 1064 nm as an excitation wavelength will raise the maximum distance d corresponding to negative Re(ε^*) by less than 0.01 nm for gold in water. The value would thus remain around 0.29 nm. Larger wavelengths do however cause more negative values of permittivity, especially below 0.2 nm of separation. They could therefore lead to stronger conductivity and more steep repulsive forces, skewing the potential towards larger gaps.

Imaginary parts of $\varepsilon^*(d, \omega)$ depicted in in **Figure 5.4.4 C** increase with rising wavelengths. This might however not be that relevant here, due to the sub-nm distances within which conductivity is required for electrically connecting the dimer halves. Thus, conversely, shorter wavelengths might in fact be useful for generating dimers with smaller gaps, potentially featuring increased tunneling effects. Overall, these effective optical constants do however suggest a limited potential for tuning gap size, on the one hand. On the other hand, calculated gap permittivities for 671 nm and longer wavelengths match that the ~0.6-1.4 nm dimer hotspots (**Subchapter 5.2**) do not appear to feature suppressed Raman enhancement (**Subchapter 5.3**).

At this point it is however important to remember that optical forces are not the only contributors to dimer gaps. The actual dimer GNS potential landscape might look very different, and DLVO theory related forces might in fact dominate. Nevertheless, the optical potential agrees with experimental results. Particularly laser driven attractive dipole-dipole coupling could assist in binding GNSs to one another over longer ranges than van der Waals forces and coulomb repulsion from ligands. Further, they could stabilize dimer printing against Brownian motion of GNSs from split GNRs. Repulsive optically induced forces might at the very least counteract excessive attraction between the nanospheres, preventing the assembly of dimers featuring significant plasmon tunneling.

Thus, hotspots generated by splitting GNRs from aqueous solution appear stable in terms of assembly as functional SERS nanoagents. This does however go hand in hand with them potentially being difficult to tune in size with a single splitting and printing laser from an optical force perspective. Further, positioning and alignment accuracy were limited in experiments. Here, a way for tuning the dimer printing process particularly in terms of antenna location and orientation might exist. Analogously to work on aligning and printing gold nanorods by Do et al. [81], a second laser might be used. More specifically, a green (532 nm) transversally polarized and resonant laser could be aligned coaxially with the NIR illumination source. It could aid both antenna alignment [86], as well as positioning via a tighter focal spot, during the printing process.

This second laser might also offer more controlled interaction of nanoparticles with the NIR laser and its larger focal spot during dimer assembly. Lastly, it might even be useful for tuning gaps, via repulsive forces between gold nanospheres from an excited antibonding transversal plasmon mode [90].

6 Concluding on GNR-Based Plasmonic Dimer Nanoagents for SERS Applications

To conclude, this PhD thesis presents two types of plasmonic dimer nanoantennas, derived from gold nanorods in two distinct ways. Both antenna types were expected to feature strong plasmonic coupling between their two metallic nanoparticle constituents. Resulting hotspots were investigated towards their potential for SERS, with a view towards measuring diffusive analyte.

Firstly, with **Chapter 4**, dimers based on tip-to-tip aligned GNRs via DNA origami, have been found effective for SERS detection of diffusive biomolecules from solution, the main goal of this thesis. For protein measurements, the streptavidin and thrombin molecules identified after entering the ~8 nm dimer hotspots were relatively large with ~5 nm. Here subsecond SERS detection was possible. Potential carbonization of nanoagent DNA origami and analyte was also not found pronounced enough to hinder measurements. The antenna design also proved successful for SM-SERS of dye. Effects of the laser on antennas were found to be angling, as well as potentially shrinking of gaps. The latter might have aided Raman measurements by increasing plasmonic coupling and E-field enhancement.

To further improve the antennas, particularly with a view towards SERS detection of larger analyte, modifications to the plasmonic multimer design were explored. Here, whilst the use of sharper tipped rodlike structures was not found conducive, flatter tips were. Further, the use of silver-based nanorods, as well as tetrameric tip-to-tip nanorod arrangements appear promising for future studies. These might also be combined with higher excitation powers via stabilizing DNA origami scaffolds through silicification and more thermally conductive substrates. Here, investigating the impact of optical forces on GNR dimers, and using this mechanism for positioning the nanoagents, might also prove fruitful.

Secondly, with **Chapter 5**, gold nanospheres generated in a single GNR splitting and printing step process, were examined for their plasmonic hotspots. Whilst high-resolution HAADF-STEM could confirm the presence of gaps, their average span had to be quantified via the resonance of their plasmon bonding mode. It was found to be ~0.8 nm in size. Resulting hotspots enabled strong resonance Raman enhancement of NTP, added post dimer creation, in solution.

Additionally, mechanisms behind the angstrom intradimer gaps were looked into, and a laser induced anharmonic intersphere potential was identified as a component. It results from classical excited dipole-dipole attraction in combination with quantum tunneling mediated single dipole separation. Tuning the parameters involved could allow for assembling dimers with more specific gap sizes. Here, larger hotspots might be suitable for studying larger diffusive analyte, in

particular proteins in aqueous solution. SERS sensing might also benefit from especially freely accessible hotspots due to a reduced presence of ligands for this type of antenna. Printing dimers with smaller gaps might in turn allow for studying of plasmon tunneling effects. Moreover, the optical excitation electromagnetic model suggests the possibility of printing dimers directly, consisting of different metallic nanoantennas including chemically synthesized metallic spheres, triangles, and rods. Whilst there might be a significant presence of ligands, leading to further DLVO interaction, such printed dimers could be suitable towards detecting larger diffusive analyte including proteins.

Beyond scientific interest, these findings present a significant step towards using SERS in further applications. Both resonators function at the NIR, making them interesting for applications in the bio-optical window. Due to the more tunable nature of the DNA origami GNR dimers, their resonance is however more optimizable than for optically split GNR dimers. Additionally, their freer deployability, as a single unit, might make them a better nanoagent candidate. In future, GNR dimers, or further optimized derivatives of them, might thus be optically trapped and positioned, potentially for in vivo and intracellular sensing. On the other hand, optically printed GNS dimers might prove effective in flow cells, and lab-on-a-chip applications. In principle, plasmonic dimers can also be employed in CARS measurements [251]. Analyzing arrays of GNR-based nanoagents with stimulated Raman scattering microscopy could thus be of further use for parallelized single protein detection, with even higher sensitivity.

Bibliography

1. C.V. Raman, *A change of wave-length in light scattering.* Nature, 1928. 121: p. 619-619. DOI: 10.1038/121619b0

2. C.V. Raman and K.S. Krishnan, *The optical analogue of the Compton effect.* Nature, 1928. 121: p. 711-711. DOI: 10.1038/121711a0

3. E.C. Le Ru, et al., *Surface enhanced Raman scattering enhancement factors: a comprehensive study.* Journal of Physical Chemistry C, 2007. 111(37): p. 13794-13803. DOI: 10.1021/jp0687908

4. P.G. Etchegoin and E.C. Le Ru, *A perspective on single molecule SERS: current status and future challenges.* Physical Chemistry Chemical Physics, 2008. 10(40): p. 6079-6089. DOI: 10.1039/b809196j

5. E.C. Le Ru and P.G. Etchegoin, *Principles of surface-enhanced Raman spectroscopy: and related plasmonic effects*. 1st ed. 2009, Amsterdam: Elsevier

6. G. Eckhardt, et al., *Stimulated Raman Scattering From Organic Liquids.* Physical Review Letters, 1962. 9(11): p. 455-457. DOI: 10.1103/PhysRevLett.9.455

7. R.C. Prince, R.R. Frontiera, and E.O. Potma, *Stimulated Raman Scattering: From Bulk to Nano.* Chemical Reviews, 2017. 117(7): p. 5070-5094. DOI: 10.1021/acs.chemrev.6b00545

8. P.D. Maker and R.W. Terhune, *Study of Optical Effects Due to an Induced Polarization Third Order in the Electric Field Strength.* Physical Review, 1965. 137(3A): p. A801-A818. DOI: 10.1103/PhysRev.137.A801

9. R.F. Begley, A.B. Harvey, and R.L. Byer, *Coherent anti-Stokes Raman spectroscopy.* Applied Physics Letters, 1974. 25(7): p. 387-390. DOI: 10.1063/1.1655519

10. S. Oh, et al., *Protein and lipid mass concentration measurement in tissues by stimulated Raman scattering microscopy.* Proceedings of the National Academy of Sciences of the United States of America, 2022. 119(17): p. e2117938119. DOI: 10.1073/pnas.2117938119

11. J.-X. Cheng and X.S. Xie, *Coherent Anti-Stokes Raman Scattering Microscopy: Instrumentation, Theory, and Applications.* The Journal of Physical Chemistry B, 2004. 108(3): p. 827-840. DOI: 10.1021/jp035693v

12. S. Heuke and H. Rigneault, *Coherent Stokes Raman scattering microscopy (CSRS).* Nature Communications, 2023. 14. DOI: 10.1038/s41467-023-38941-4

13. M. Fleischmann, P.J. Hendra, and A.J. Mcquillan, *Raman-Spectra of Pyridine Adsorbed at a Silver Electrode.* Chemical Physics Letters, 1974. 26(2): p. 163-166. DOI: 10.1016/0009-2614(74)85388-1

14. D.L. Jeanmaire and R.P. Van Duyne, *Surface Raman Spectroelectrochemistry Part 1. Heterocyclic, Aromatic, and Aliphatic-Amines Adsorbed on Anodized Silver Electrode.* Journal of Electroanalytical Chemistry, 1977. 84(1): p. 1-20. DOI: 10.1016/S0022-0728(77)80224-6

15. M.R. Philpott, *Effect of Surface Plasmons on Transitions in Molecules.* Journal of Chemical Physics, 1975. 62(5): p. 1812-1817. DOI: 10.1063/1.430708

16. M.G. Albrecht and J.A. Creighton, *Anomalously Intense Raman-Spectra of Pyridine at a Silver Electrode.* Journal of the American Chemical Society, 1977. 99(15): p. 5215-5217. DOI: 10.1021/ja00457a071

17. L.M. Almehmadi, et al., *Surface Enhanced Raman Spectroscopy for Single Molecule Protein Detection.* Scientific Reports, 2019. 9. DOI: 10.1038/s41598-019-48650-y

18. A. Weiss and G. Haran, *Time-dependent single-molecule Raman scattering as a probe of surface dynamics.* Journal of Physical Chemistry B, 2001. 105(49): p. 12348-12354. DOI: 10.1021/jp0126863

19. B.S. Yeo, et al., *Tip-enhanced Raman spectroscopy can see more:: The case of cytochrome C.* Journal of Physical Chemistry C, 2008. 112(13): p. 4867-4873. DOI: 10.1021/jp709799m

20. H.S. Davies, et al., *Secondary Structure and Glycosylation of Mucus Glycoproteins by Raman Spectroscopies.* Analytical Chemistry, 2016. 88(23): p. 11609-11615. DOI: 10.1021/acs.analchem.6b03095

21. M.A. Huergo, et al., *Plasmonic Nanoagents in Biophysics and Biomedicine.* Advanced Optical Materials, 2022. 10(14). DOI: 10.1002/adom.202200572

22. I. Freestone, et al., *The Lycurgus Cup - A Roman nanotechnology.* Gold Bulletin, 2007. 40(4): p. 270-277. DOI: 10.1007/Bf03215599

23. M. Faraday, *The bakerian lecture: Experimental relations of gold (and other metals) to light.* 1857: Philosophical Transactions of the Royal Society of London

24. R. Zsigmondy, *Zur Erkenntnis der Kolloide: Über irreversile Hydrosole und Ultramikroskopie*. 1905, Jena: Verlag von Gustav Fischer

25. G. Mie, *Articles on the optical characteristics of turbid tubes, especially colloidal metal solutions.* Annalen Der Physik, 1908. 25(3): p. 377-445

26. R. Gans, *Über die Form ultramikroskopischer Goldteilchen.* Annalen der Physik, 1912. 342(5): p. 881-900. DOI: 10.1002/andp.19123420503

27. M. Pelton and G.W. Bryant, *Introduction to metal-nanoparticle plasmonics*. 2013, Hoboken, New Jersey: John Wiley & Sons

28. A. Gole and C.J. Murphy, *Seed-mediated synthesis of gold nanorods: Role of the size and nature of the seed.* Chemistry of Materials, 2004. 16(19): p. 3633-3640. DOI: 10.1021/cm0492336

29. T. Ming, et al., *Growth of Tetrahexahedral Gold Nanocrystals with High-index Facets.* Journal of the American Chemical Society, 2009. 131(45): p. 16350-16351. DOI: 10.1021/ja907549n

30. L. Scarabelli, et al., *A "Tips and Tricks" Practical Guide to the Synthesis of Gold Nanorods.* Journal of Physical Chemistry Letters, 2015. 6(21): p. 4270-4279. DOI: 10.1021/acs.jpclett.5b02123

31. N.R. Jana, L. Gearheart, and C.J. Murphy, *Wet chemical synthesis of high aspect ratio cylindrical gold nanorods.* Journal of Physical Chemistry B, 2001. 105(19): p. 4065-4067. DOI: 10.1021/jp0107964

32. J. Turkevich, P.C. Stevenson, and J. Hillier, *A Study of the Nucleation and Growth Processes in the Synthesis of Colloidal Gold.* Discussions of the Faraday Society, 1951(11): p. 55-75. DOI: 10.1039/df9511100055

33. A.R. Tao, S. Habas, and P.D. Yang, *Shape control of colloidal metal nanocrystals.* Small, 2008. 4(3): p. 310-325. DOI: 10.1002/smll.200701295

34. L.J.E. Anderson, et al., *Quantitative Measurements of Individual Gold Nanoparticle Scattering Cross Sections.* Journal of Physical Chemistry C, 2010. 114(25): p. 11127-11132. DOI: 10.1021/jp1040663

35. O.P. Varnavski, et al., *Relative enhancement of ultrafast emission in gold nanorods.* Journal of Physical Chemistry B, 2003. 107(14): p. 3101-3104. DOI: 10.1021/jp0341265

36. P.W.K. Rothemund, *Folding DNA to create nanoscale shapes and patterns.* Nature, 2006. 440(7082): p. 297-302. DOI: 10.1038/nature04586

37. S.M. Douglas, et al., *Self-assembly of DNA into nanoscale three-dimensional shapes.* Nature, 2009. 459(7245): p. 414-418. DOI: 10.1038/nature08016

38. S. Simoncelli, et al., *Quantitative Single-Molecule Surface Enhanced Raman Scattering by Optothermal Tuning of DNA Origami-Assembled Plasmonic Nanoantennas.* ACS Nano, 2016. 10(11): p. 9809-9815. DOI: 10.1021/acsnano.6b05276

39. J. Prinz, et al., *DNA origami based Au-Ag-core-shell nanoparticle dimers with single-molecule SERS sensitivity.* Nanoscale, 2016. 8(10): p. 5612-5620. DOI: 10.1039/c5nr08674d

40. K. Tapio, et al., *A Versatile DNA Origami-Based Plasmonic Nanoantenna for Label-Free Single-Molecule Surface-Enhanced Raman Spectroscopy.* ACS Nano, 2021. 15(4): p. 7065-7077. DOI: 10.1021/acsnano.1c00188

41. S. Tanwar, et al., *Broadband SERS Enhancement by DNA Origami Assembled Bimetallic Nanoantennas with Label-Free Single Protein Sensing.* Journal of Physical Chemistry Letters, 2021. 12(33): p. 8141-8150. DOI: 10.1021/acs.jpclett.1c02272

42. P.F. Zhan, et al., *DNA Origami Directed Assembly of Gold Bowtie Nanoantennas for Single-Molecule Surface-Enhanced Raman Scattering.* Angewandte Chemie-International Edition, 2018. 57(11): p. 2846-2850. DOI: 10.1002/anie.201712749

43. S.A. Maier, et al., *Plasmonics - A route to nanoscale optical devices.* Advanced Materials, 2001. 13(19): p. 1501-1505. DOI: 10.1002/1521-4095(200110)13:19<1501::Aid-Adma1501>3.0.Co;2-Z

44. P.K. Jain and M.A. El-Sayed, *Surface plasmon coupling and its universal size scaling in metal nanostructures of complex geometry: Elongated particle pairs and nanosphere trimers.* Journal of Physical Chemistry C, 2008. 112(13): p. 4954-4960. DOI: 10.1021/jp7120356

45. E.C. Le Ru and P.G. Etchegoin, *Rigorous justification of the |E|4 enhancement factor in Surface Enhanced Raman Spectroscopy.* Chemical Physics Letters, 2006. 423(1): p. 63-66. DOI: 10.1016/j.cplett.2006.03.042

46. L.M. Ng and R. Simmons, *Infrared spectroscopy.* Analytical Chemistry, 1999. 71(12): p. 343-350. DOI: 10.1021/a1999908r

47. P.J. Larkin, *Infrared and Raman Spectroscopy: Principles and Spectral Interpretation.* Infrared and Raman Spectroscopy: Principles and Spectral Interpretation, 2011: p. 1-228

48. J.A. Stratton, *Electromagnetic theory*. 1st ed. International series in physics. 1941, New York: McGraw-Hill book company, inc.

49. J.D. Jackson, *Classical electrodynamics*. 3rd ed. 1999, Chichester; New York: Wiley

50. A. Anderson, *The Raman effect*. 1971, New York: M. Dekker

51. L.D. Landau, E.M. Lifshitz, and L.P. Pitaevskiĭ, *Electrodynamics of continuous media*. 2nd ed. Course of theoretical physics / L D Landau & E M Lifshitz. 1984, Oxford Oxfordshire ; New York: Pergamon

52. S. Mahajan, et al., *Understanding the Surface-Enhanced Raman Spectroscopy "Background".* Journal of Physical Chemistry C, 2010. 114(16): p. 7242-7250. DOI: 10.1021/jp907197b

53. S.A. Maier, *Plasmonics: Fundamentals and Applications*. 2007, USA: Springer Science+Buisness Media

54. M. Pelton, *Introduction to Metal-Nanoparticle Plasmonics*. 2013, USA: Wiley

55. R.L. Olmon, et al., *Optical dielectric function of gold.* Physical Review B, 2012. 86(23). DOI: 10.1103/PhysRevB.86.235147

56. C.M. Maier, *PhD Thesis: Optically Induced Forces on Anisotropic Plasmonic Nanoparticles*, in *Physics Department*. 2020, Ludwig-Maximilians-Universität München

57. P.B. Johnson and R.W. Christy, *Optical Constants of Noble Metals.* Physical Review B, 1972. 6(12): p. 4370-4379. DOI: 10.1103/PhysRevB.6.4370

58. H. Fröhlich, *Theory of dielectrics: dielectric constant and dielectric loss*. 1958, GB: Oxford: Clarendon Press

59. C. Sonnichsen, et al., *Drastic reduction of plasmon damping in gold nanorods.* Physical Review Letters, 2002. 88(7). DOI: 10.1103/PhysRevLett.88.077402

60. V. Myroshnychenko, et al., *Modelling the optical response of gold nanoparticles.* Chemical Society Reviews, 2008. 37(9): p. 1792-1805. DOI: 10.1039/b711486a

61. H.K. Yuan, et al., *Gold nanostars: surfactant-free synthesis, 3D modelling, and two-photon photoluminescence imaging.* Nanotechnology, 2012. 23(7). DOI: 10.1088/0957-4484/23/7/075102

62. S. Chatterjee, et al., *A high-yield, one-step synthesis of surfactant-free gold nanostars and numerical study for single-molecule SERS application.* Journal of Nanoparticle Research, 2016. 18(8). DOI: 10.1007/s11051-016-3557-0

63. L. Chen, et al., *High-Yield Seedless Synthesis of Triangular Gold Nanoplates through Oxidative Etching.* Nano Letters, 2014. 14(12): p. 7201-7206. DOI: 10.1021/nl504126u

64. G. Zhang, et al., *Tunability and stability of gold nanoparticles obtained from chloroauric Acid and sodium thiosulfate reaction.* Nanoscale Res Lett, 2012. 7(1): p. 337. DOI: 10.1186/1556-276X-7-337

65. C.M. Otero, et al., *Optimized Biocompatible Gold Nanotriangles with NIR Absorption for Photothermal Applications.* ACS Applied Nano Materials, 2022. 5(1): p. 341-350. DOI: 10.1021/acsanm.1c03148

66. J.H. Lee, et al., *Bipyramid-templated synthesis of monodisperse anisotropic gold nanocrystals.* Nature Communications, 2015. 6. DOI: 10.1038/ncomms8571

67. J.L. Lv, et al., *Rapid synthesizing of gold nanobipyramids.* Materials Research Express, 2020. 7(2). DOI: 10.1088/2053-1591/ab726b

68. J.R. Krenn, et al., *Squeezing the optical near-field zone by plasmon coupling of metallic nanoparticles.* Physical Review Letters, 1999. 82(12): p. 2590-2593. DOI: 10.1103/PhysRevLett.82.2590

69. P. Nordlander, et al., *Plasmon Hybridization in Nanoparticle Dimers.* Nano Letters, 2004. 4(5): p. 899-903. DOI: 10.1021/nl049681c

70. T.S. Deng, et al., *Dark Plasmon Modes in Symmetric Gold Nanoparticle Dimers Illuminated by Focused Cylindrical Vector Beams.* Journal of Physical Chemistry C, 2018. 122(48): p. 27662-27672. DOI: 10.1021/acs.jpcc.8b10415

71. P.K. Jain, W.Y. Huang, and M.A. El-Sayed, *On the universal scaling behavior of the distance decay of plasmon coupling in metal nanoparticle pairs: A plasmon ruler equation.* Nano Letters, 2007. 7(7): p. 2080-2088. DOI: 10.1021/nl071008a

72. C. Sonnichsen, et al., *A molecular ruler based on plasmon coupling of single gold and silver nanoparticles.* Nature Biotechnology, 2005. 23(6): p. 741-745. DOI: 10.1038/nbt1100

73. N. Liu, et al., *Three-Dimensional Plasmon Rulers.* Science, 2011. 332(6036): p. 1407-1410. DOI: 10.1126/science.1199958

74. W.T. Simpson and D.L. Peterson, *Coupling Strength for Resonance Force Transfer of Electronic Energy in Vanderwaals Solids.* Journal of Chemical Physics, 1957. 26(3): p. 588-593. DOI: 10.1063/1.1743351

75. H.X. Xu, et al., *Spectroscopy of single hemoglobin molecules by surface enhanced Raman scattering.* Physical Review Letters, 1999. 83(21): p. 4357-4360. DOI: 10.1103/PhysRevLett.83.4357

76. R. Esteban, et al., *Bridging quantum and classical plasmonics with a quantum-corrected model.* Nature Communications, 2012. 3. DOI: 10.1038/ncomms1806

77. F.J. Garcia de Abajo, *Nonlocal Effects in the Plasmons of Strongly Interacting Nanoparticles, Dimers, and Waveguides.* Journal of Physical Chemistry C, 2008. 112(46): p. 17983-17987. DOI: 10.1021/jp807345h

78. T.V. Teperik, et al., *Robust Subnanometric Plasmon Ruler by Rescaling of the Nonlocal Optical Response.* Physical Review Letters, 2013. 110(26). DOI: 10.1103/PhysRevLett.110.263901

79. R. Esteban, et al., *A classical treatment of optical tunneling in plasmonic gaps: extending the quantum corrected model to practical situations.* Faraday Discussions, 2015. 178: p. 151-183. DOI: 10.1039/c4fd00196f

80. L. Tong, V.D. Miljkovic, and M. Kall, *Alignment, rotation, and spinning of single plasmonic nanoparticles and nanowires using polarization dependent optical forces.* Nano Lett, 2010. 10(1): p. 268-73. DOI: 10.1021/nl9034434

81. J. Do, et al., *Two-Color Laser Printing of Individual Gold Nanorods.* Nano Letters, 2013. 13(9): p. 4164-4168. DOI: 10.1021/nl401788w

82. A.S. Urban, et al., *Optical trapping and manipulation of plasmonic nanoparticles: fundamentals, applications, and perspectives.* Nanoscale, 2014. 6(9): p. 4458-74. DOI: 10.1039/c3nr06617g

83. C. Zhan, et al., *Single-Molecule Plasmonic Optical Trapping.* Matter, 2020. 3(4): p. 1350-1360. DOI: 10.1016/j.matt.2020.07.019

84. A.S. Urban, et al., *Laser Printing Single Gold Nanoparticles.* Nano Letters, 2010. 10(12): p. 4794-4798. DOI: 10.1021/nl1030425

85. C. Zensen, et al., *Pushing nanoparticles with light - A femtonewton resolved measurement of optical scattering forces.* Apl Photonics, 2016. 1(2). DOI: 10.1063/1.4945351

86. J.W. Liaw, W.J. Lo, and M.K. Kuo, *Wavelength-dependent longitudinal polarizability of gold nanorod on optical torques.* Optics Express, 2014. 22(9): p. 10858-10867. DOI: 10.1364/Oe.22.010858

87. J.W. Liaw, Y.S. Chen, and M.K. Kuo, *Maxwell stress induced optical torque upon gold prolate nanospheroid.* Applied Physics a-Materials Science & Processing, 2016. 122(3). DOI: 10.1007/s00339-016-9732-4

88. O.M. Marago, et al., *Optical trapping and manipulation of nanostructures.* Nature Nanotechnology, 2013. 8(11): p. 807-19. DOI: 10.1038/nnano.2013.208

89. J.W. Liaw, et al., *Plasmon-enhanced optical bending and heating on V-shaped deformation of gold nanorod.* Applied Physics a-Materials Science & Processing, 2018. 124(1). DOI: 10.1007/s00339-017-1433-0

90. V.D. Miljkovic, et al., *Optical Forces in Plasmonic Nanoparticle Dimers.* Journal of Physical Chemistry C, 2010. 114(16): p. 7472-7479. DOI: 10.1021/jp911371r

91. L.M. Tong, et al., *Plasmon Hybridization Reveals the Interaction between Individual Colloidal Gold Nanoparticles Confined in an Optical Potential Well.* Nano Letters, 2011. 11(11): p. 4505-4508. DOI: 10.1021/nl1036116

92. D.J. Griffiths, *Introduction to electrodynamics*. Fourth edition. ed. 2013, Boston: Pearson

93. S.A. Maier and H.A. Atwater, *Plasmonics: Localization and guiding of electromagnetic energy in metal/dielectric structures.* Journal of Applied Physics, 2005. 98(1). DOI: 10.1063/1.1951057

94. U. Kreibig, et al., *Optical properties of free and embedded metal clusters: Recent results.* Large Clusters of Atoms and Molecules, 1996. 313: p. 475-493

95. J.H. Weaver, et al., *Optical Properties of Metals.* Applied Optics, 1981. 20(7): p. 1124-1125. DOI: 10.1364/AO.20.1124_1

96. B. Bernert and P. Zacharias, *Optical Constants of Silver-Gallium Alloys near Plasma Frequency - Quantitative Comparison with Electron Energy Loss Spectra.* Zeitschrift Fur Physik, 1971. 241(3): p. 205-216. DOI: 10.1007/Bf01395329

97. H. Hovel, et al., *Width of Cluster Plasmon Resonances - Bulk Dielectric Functions and Chemical Interface Damping.* Physical Review B, 1993. 48(24): p. 18178-18188. DOI: 10.1103/PhysRevB.48.18178

98. A. Babynina, et al., *Bending Gold Nanorods with Light.* Nano Letters, 2016. 16(10): p. 6485-6490. DOI: 10.1021/acs.nanolett.6b03029

99. S. Berciaud, et al., *Observation of intrinsic size effects in the optical response of individual gold nanoparticles.* Nano Letters, 2005. 5(3): p. 515-518. DOI: 10.1021/nl050062t

100. W.S. Fann, et al., *Electron Thermalization in Gold.* Physical Review B, 1992. 46(20): p. 13592-13595. DOI: 10.1103/PhysRevB.46.13592

101. A. Hoggard, et al., *Using the Plasmon Linewidth To Calculate the Time and Efficiency of Electron Transfer between Gold Nanorods and Graphene.* ACS Nano, 2013. 7(12): p. 11209-11217. DOI: 10.1021/nn404985h

102. K. Wu, et al., *Efficient hot-electron transfer by a plasmon-induced interfacial charge-transfer transition.* Science, 2015. 349(6248): p. 632-635. DOI: 10.1126/science.aac5443

103. B. Foerster, et al., *Chemical Interface Damping Depends on Electrons Reaching the Surface.* ACS Nano, 2017. 11(3): p. 2886-2893. DOI: 10.1021/acsnano.6b08010

104. G. Baffou and R. Quidant, *Nanoplasmonics for chemistry.* Chemical Society Reviews, 2014. 43(11): p. 3898-3907. DOI: 10.1039/c3cs60364d

105. R.G. Hobbs, et al., *Mapping Photoemission and Hot-Electron Emission from Plasmonic Nanoantennas.* Nano Letters, 2017. 17(10): p. 6069-6076. DOI: 10.1021/acs.nanolett.7b02495

106. E. Cortés, et al., *Plasmonic hot electron transport drives nano-localized chemistry.* Nature Communications, 2017. 8. DOI: 10.1038/ncomms14880

107. B.N.J. Persson, *Polarizability of Small Spherical Metal Particles - Influence of the Matrix Environment.* Surface Science, 1993. 281(1-2): p. 153-162. DOI: 10.1016/0039-6028(93)90865-H

108. K. Puech, et al., *Investigation of the Ultrafast Dephasing Time of Gold Nanoparticles Using Incoherent-Light.* Chemical Physics Letters, 1995. 247(1-2): p. 13-17. DOI: 10.1016/0009-2614(95)01196-1

109. S.L. Logunov, et al., *Electron dynamics of passivated gold nanocrystals probed by subpicosecond transient absorption spectroscopy.* Journal of Physical Chemistry B, 1997. 101(19): p. 3713-3719. DOI: 10.1021/jp962923f

110. T.S. Ahmadi, S.L. Logunov, and M.A. ElSayed, *Picosecond dynamics of colloidal gold nanoparticles.* Journal of Physical Chemistry, 1996. 100(20): p. 8053-8056. DOI: 10.1021/jp960484e

111. S. Link, et al., *Electron dynamics in gold and gold-silver alloy nanoparticles: The influence of a nonequilibrium electron distribution and the size dependence of the electron-phonon relaxation.* Journal of Chemical Physics, 1999. 111(3): p. 1255-1264. DOI: 10.1063/1.479310

112. M. Hu and G.V. Hartland, *Heat dissipation for Au particles in aqueous solution: Relaxation time versus size.* Journal of Physical Chemistry B, 2002. 106(28): p. 7029-7033. DOI: 10.1021/jp020581+

113. G. Mannino, et al., *Raman amplification for trapped radiation in crystalline single Si nanoparticle.* Scientific Reports, 2023. 13(1). DOI: 10.1038/s41598-023-27839-2

114. R.F. Egerton, *Physical principles of electron microscopy : an introduction to TEM, SEM, and AEM*. 2005, New York, NY: Springer

115. T. Klein, E. Buhr, and C.G. Frase, *TSEM: A Review of Scanning Electron Microscopy in Transmission Mode and Its Applications.* Advances in Imaging and Electron Physics, Vol 171, 2012. 171: p. 297-356. DOI: 10.1016/B978-0-12-394297-5.00006-4

116. M.T. Otten, *High-Angle Annular Dark-Field Imaging on a Tem/Stem System.* Journal of Electron Microscopy Technique, 1991. 17(2): p. 221-230. DOI: 10.1002/jemt.1060170209

117. K.S. Yee, *Numerical Solution of Initial Boundary Value Problems Involving Maxwells Equations in Isotropic Media.* Ieee Transactions on Antennas and Propagation, 1966. Ap14(3): p. 302-&

118. G. Baffou, R. Quidant, and C. Girard, *Heat generation in plasmonic nanostructures: Influence of morphology.* Applied Physics Letters, 2009. 94(15). DOI: 10.1063/1.3116645

119. E.D. Palik, *Handbook of optical constants of solids II*. 1991, Boston: Academic Press

120. W.K. Liu, S.F. Li, and H.S. Park, *Eighty Years of the Finite Element Method: Birth, Evolution, and Future.* Archives of Computational Methods in Engineering, 2022. 29(6): p. 4431-4453. DOI: 10.1007/s11831-022-09740-9

121. M.J. Turner, et al., *Stiffness and Deflection Analysis of Complex Structures.* Journal of the Aeronautical Sciences, 1956. 23(9): p. 805-&. DOI: 10.2514/8.3664

122. J.N. Reddy and D.K. Gartling, *The finite element method in heat transfer and fluid dynamics*. 3rd ed. CRC series in computational mechanics and applied analysis. 2010, Boca Raton, FL: CRC Press

123. M. Piliarik and V. Sandoghdar, *Direct optical sensing of single unlabelled proteins and super-resolution imaging of their binding sites.* Nature Communications, 2014. 5. DOI: 10.1038/ncomms5495

124. P.F. Zhang, et al., *Plasmonic scattering imaging of single proteins and binding kinetics.* Nature Methods, 2020. 17(10): p. 1010-1017. DOI: 10.1038/s41592-020-0947-0

125. P.F. Zhang, et al., *Quantification of Single-Molecule Protein Binding Kinetics in Complex Media with Prism-Coupled Plasmonic Scattering Imaging.* ACS Sensors, 2021. 6(3): p. 1357-1366. DOI: 10.1021/acssensors.0c02729

126. L.Q. Gu and J.W. Shim, *Single molecule sensing by nanopores and nanopore devices.* Analyst, 2010. 135(3): p. 441-451. DOI: 10.1039/b907735a

127. A. Barth, *Infrared spectroscopy of proteins.* Biochimica Et Biophysica Acta-Bioenergetics, 2007. 1767(9): p. 1073-1101. DOI: 10.1016/j.bbabio.2007.06.004

128. V.V. Thacker, et al., *DNA origami based assembly of gold nanoparticle dimers for surface-enhanced Raman scattering.* Nature Communications, 2014. 5. DOI: 10.1038/ncomms4448

129. P. Kühler, et al., *Plasmonic DNA-Origami Nanoantennas for Surface-Enhanced Raman Spectroscopy.* Nano Letters, 2014. 14(5): p. 2914-2919. DOI: 10.1021/nl5009635

130. S. Tanwar, K.K. Haldar, and T. Sen, *DNA Origami Directed Au Nanostar Dimers for Single-Molecule Surface-Enhanced Raman Scattering.* Journal of the American Chemical Society, 2017. 139(48): p. 17639-17648. DOI: 10.1021/jacs.7b10410

131. V. Kaur, et al., *DNA-Origami-Based Assembly of Au@Ag Nanostar Dimer Nanoantennas for Label-Free Sensing of Pyocyanin.* Chemphyschem, 2020. 22(2): p. 160-167. DOI: 10.1002/cphc.202000805

132. V. Kaur, M. Sharma, and T. Sen, *DNA Origami-Templated Bimetallic Nanostar Assemblies for Ultra-Sensitive Detection of Dopamine.* Frontiers in Chemistry, 2021. 9. DOI: 10.3389/fchem.2021.772267

133. T.S. Zhang, et al., *Single-Particle Spectroscopic Study on Fluorescence Enhancement by Plasmon Coupled Gold Nanorod Dimers Assembled on DNA Origami.* Journal of Physical Chemistry Letters, 2015. 6(11): p. 2043-2049. DOI: 10.1021/acs.jpclett.5b00747

134. K. Trofymchuk, et al., *Gold Nanorod DNA Origami Antennas for 3 Orders of Magnitude Fluorescence Enhancement in NIR.* ACS Nano, 2023. 17(2): p. 1327-1334. DOI: 10.1021/acsnano.2c09577

135. L. Tie, et al., *Controlling the end-to-end assembly of gold nanorods to enhance the plasmonic response in near infrared.* Materials Research Express, 2019. 6(9). DOI: 10.1088/2053-1591/ab2eb0

136. F. Schuknecht, et al., *Accessible hotspots for single-protein SERS in DNA-origami assembled gold nanorod dimers with tip-to-tip alignment.* Nature Communications, 2023. 14. DOI: 10.1038/s41467-023-42943-7

137. C.J. van Oss, et al., *Macroscopic-scale surface properties of streptavidin and their influence on aspecific interactions between streptavidin and dissolved biopolymers.* Colloids and Surfaces B-Biointerfaces, 2003. 30(1-2): p. 25-36. DOI: 10.1016/S0927-7765(03)00025-0

138. L.P. Kozlowski, *Proteome-pI: proteome isoelectric point database.* Nucleic Acids Research, 2017. 45(D1): p. D1112-D1116. DOI: 10.1093/nar/gkw978

139. Z. Movasaghi, S. Rehman, and I.U. Rehman, *Raman spectroscopy of biological tissues.* Applied Spectroscopy Reviews, 2007. 42(5): p. 493-541. DOI: 10.1080/05704920701551530

140. J. Sharma, et al., *Toward reliable gold nanoparticle patterning on self-assembled DNA nanoscaffold.* Journal of the American Chemical Society, 2008. 130(25): p. 7820-7821. DOI: 10.1021/ja802853r

141. L.A. Stearns, et al., *Template-Directed Nucleation and Growth of Inorganic Nanoparticles on DNA Scaffolds.* Angewandte Chemie-International Edition, 2009. 48(45): p. 8494-8496. DOI: 10.1002/anie.200903319

142. M. Pilo-Pais, et al., *Surface-Enhanced Raman Scattering Plasmonic Enhancement Using DNA Origami-Based Complex Metallic Nanostructures.* Nano Letters, 2014. 14(4): p. 2099-2104. DOI: 10.1021/nl5003069

143. C. Heck, et al., *Placement of Single Proteins within the SERS Hot Spots of Self-Assembled Silver Nanolenses.* Angewandte Chemie-International Edition, 2018. 57(25): p. 7444-7447. DOI: 10.1002/anie.201801748

144. W.N. Fang, et al., *Quantizing single-molecule surface-enhanced Raman scattering with DNA origami metamolecules.* Science Advances, 2019. 5(9). DOI: 10.1126/sciadv.aau4506

145. C. Heck, et al., *Amorphous Carbon Generation as a Photocatalytic Reaction on DNA-Assembled Gold and Silver Nanostructures.* Molecules, 2019. 24(12). DOI: 10.3390/molecules24122324

146. C. Kaur, et al., *Selective recognition of the amyloid marker single thioflavin T using DNA origami-based gold nanobipyramid nanoantennas.* Nanoscale, 2023. 15(13): p. 6170-6718. DOI: 10.1039/d2nr06389a

147. Y. Kanehira, et al., *The Effect of Nanoparticle Composition on the Surface-Enhanced Raman Scattering Performance of Plasmonic DNA Origami Nanoantennas.* ACS Nano, 2023. DOI: 10.1021/acsnano.3c05464

148. S.M. Douglas, et al., *Rapid prototyping of 3D DNA-origami shapes with caDNAno.* Nucleic Acids Research, 2009. 37(15): p. 5001-5006. DOI: 10.1093/nar/gkp436

149. F. Hong, et al., *DNA Origami: Scaffolds for Creating Higher Order Structures.* Chemical Reviews, 2017. 117(20): p. 12584-12640. DOI: 10.1021/acs.chemrev.6b00825

150. S. Link, Z.L. Wang, and M.A. El-Sayed, *How does a gold nanorod melt?* Journal of Physical Chemistry B, 2000. 104(33): p. 7867-7870. DOI: 10.1021/jp0011701

151. L.J. Lewis, P. Jensen, and J.L. Barrat, *Melting, freezing, and coalescence of gold nanoclusters.* Physical Review B, 1997. 56(4): p. 2248-2257. DOI: 10.1103/PhysRevB.56.2248

152. S. Karim, et al., *Morphological evolution of Au nanowires controlled by Rayleigh instability.* Nanotechnology, 2006. 17(24): p. 5954-5959. DOI: 10.1088/0957-4484/17/24/009

153. H. Kim, et al., *Stability of DNA Origami Nanostructure under Diverse Chemical Environments.* Chemistry of Materials, 2014. 26(18): p. 5265-5273. DOI: 10.1021/cm5019663

154. H. Mustroph, et al., *Relationship between the Molecular Structure of Cyanine Dyes and the Vibrational Fine Structure of their Electronic Absorption Spectra.* Chemphyschem, 2009. 10(5): p. 835-840. DOI: 10.1002/cphc.200800755

155. H. Sato, et al., *Raman-Spectra of Some Indo-Carbocyanine, Thia-Carbocyanine and Selena-Carbocyanine Dyes.* Journal of Raman Spectroscopy, 1988. 19(2): p. 129-132. DOI: 10.1002/jrs.1250190210

156. Y.W.C. Cao, R.C. Jin, and C.A. Mirkin, *Nanoparticles with Raman spectroscopic fingerprints for DNA and RNA detection.* Science, 2002. 297(5586): p. 1536-1540. DOI: 10.1126/science.297.5586.1536

157. J.P. Yang and R.H. Callender, *The Resonance Raman-Spectra of Some Cyanine Dyes.* Journal of Raman Spectroscopy, 1985. 16(5): p. 319-321. DOI: 10.1002/jrs.1250160507

158. I.K. Lednev, et al., *A Raman-Spectroscopic Study of Indolinium Steryl Dyes.* Spectrochimica Acta Part a-Molecular and Biomolecular Spectroscopy, 1992. 48(7): p. 931-937. DOI: 10.1016/0584-8539(92)80169-W

159. P.G. Etchegoin and E.C. Le Ru, *Resolving Single Molecules in Surface-Enhanced Raman Scattering within the Inhomogeneous Broadening of Raman Peaks.* Analytical Chemistry, 2010. 82(7): p. 2888-2892. DOI: 10.1021/ac9028888

160. K. Trofymchuk, et al., *Gold Nanorod DNA Origami Antennas for 3 Orders of Magnitude Fluorescence Enhancement in NIR.* ACS Nano, 2023. DOI: 10.1021/acsnano.2c09577

161. E. Dulkeith, et al., *Fluorescence quenching of dye molecules near gold nanoparticles:: Radiative and nonradiative effects.* Physical Review Letters, 2002. 89(20). DOI: 10.1103/PhysRevLett.89.203002

162. E. Dulkeith, et al., *Gold nanoparticles quench fluorescence by phase induced radiative rate suppression.* Nano Letters, 2005. 5(4): p. 585-589. DOI: 10.1021/nl0480969

163. A. Otto, *What is observed in single molecule SERS, and why?* Journal of Raman Spectroscopy, 2002. 33(8): p. 593-598. DOI: 10.1002/jrs.879

164. J. Szczerbinski, et al., *Plasmon-Driven Photocatalysis Leads to Products Known from E-beam and X-ray-Induced Surface Chemistry.* Nano Letters, 2018. 18(11): p. 6740-6749. DOI: 10.1021/acs.nanolett.8b02426

165. A. Kudelski, *Role of O2 in inducing intensive fluctuations of surface-enhanced Raman scattering spectra.* Journal of Physical Chemistry B, 2006. 110(25): p. 12610-12615. DOI: 10.1021/jp061295r

166. A. Kudelski, *Some aspects of SERS temporal fluctuations: analysis of the most intense spectra of hydrogenated amorphous carbon deposited on silver.* Journal of Raman Spectroscopy, 2007. 38(11): p. 1494-1499. DOI: 10.1002/jrs.1799

167. H. Sellers, et al., *Structure and Binding of Alkanethiolates on Gold and Silver Surfaces: Implications for Self-Assembled Monolayers.* Journal of the American Chemical Society, 1993. 115: p. 9389-9401. DOI: 10.1021/ja00074a004

168. E.J. Bjerneld, et al., *Direct observation of heterogeneous photochemistry on aggregated Ag nanocrystals using Raman spectroscopy: The case of photoinduced degradation of aromatic amino acids.* Journal of Physical Chemistry A, 2004. 108(19): p. 4187-4193. DOI: 10.1021/jp037004l

169. R. Jungmann, et al., *Single-Molecule Kinetics and Super-Resolution Microscopy by Fluorescence Imaging of Transient Binding on DNA Origami.* Nano Letters, 2010. 10(11): p. 4756-4761. DOI: 10.1021/nl103427w

170. D. Burnat, et al., *Functional fluorine-doped tin oxide coating for opto-electrochemical label-free biosensors.* Sensors and Actuators B-Chemical, 2022. 367. DOI: 10.1016/j.snb.2022.132145

171. E.C. Yusko, et al., *Real-time shape approximation and fingerprinting of single proteins using a nanopore.* Nature Nanotechnology, 2017. 12(4): p. 360-367. DOI: 10.1038/Nnano.2016.267

172. N.M. Green, *Avidin and Streptavidin.* Methods in Enzymology, 1990. 184: p. 51-67

173. T.C. Wu, et al., *Raman and Surface-Enhanced Raman Scattering (SERS) Studies of the Thrombin-Binding Aptamer.* IEEE Transactions on Nanobioscience, 2013. 12(2): p. 93-97. DOI: 10.1109/Tnb.2013.2242484

174. B.C. Galarreta, P.R. Norton, and F. Lagugne-Labarthet, *SERS Detection of Streptavidin/Biotin Monolayer Assemblies.* Langmuir, 2011. 27(4): p. 1494-1498. DOI: 10.1021/la1047497

175. G. Rutherford, et al., *Photochemical Growth of Highly Densely Packed Gold Nanoparticle Films for Biomedical Diagnostics.* Ecs Journal of Solid State Science and Technology, 2015. 4(10): p. S3071-S3076. DOI: 10.1149/2.0081510jss

176. H. Wang and Z.D. Schultz, *The chemical origin of enhanced signals from tip-enhanced Raman detection of functionalized nanoparticles.* Analyst, 2013. 138(11): p. 3150-3157. DOI: 10.1039/c3an36898j

177. C. Fagnano, A. Torreggiani, and G. Fini, *Raman spectroscopic studies of the anhydrous complexes of avidin and streptavidin with biotin.* Biospectroscopy, 1996. 2(4): p. 225-232. DOI: 10.1002/(Sici)1520-6343(1996)2:4<225::Aid-Bspy3>3.0.Co;2-5

178. X. Fan, et al., *Single particle cryo-EM reconstruction of 52 kDa streptavidin at 3.2 Angstrom resolution.* Nature Communications, 2019. 10. DOI: 10.1038/s41467-019-10368-w

179. R.K. Dukor, *Vibrational Spectroscopy in the Detection of Cancer*, in *Handbook of Vibrational Spectroscopy*. 2006, Hoboken, New Jersey: John Wiley & Sons. DOI: 10.1002/0470027320.s8107

180. J.W. Chan, et al., *Micro-Raman spectroscopy detects individual neoplastic and normal hematopoietic cells.* Biophysical Journal, 2006. 90(2): p. 648-56. DOI: 10.1529/biophysj.105.066761

181. A.J. Ruiz-Chica, et al., *Characterization by Raman spectroscopy of conformational changes on guanine–cytosine and adenine–thymine oligonucleotides induced by aminooxy analogues of spermidine.* Journal of Raman Spectroscopy, 2004. 35(2): p. 93-100. DOI: 10.1002/jrs.1107

182. A. Rygula, et al., *Raman spectroscopy of proteins: a review.* Journal of Raman Spectroscopy, 2013. 44(8): p. 1061-1076. DOI: 10.1002/jrs.4335

183. Z. Huang, et al., *Near-infrared Raman spectroscopy for optical diagnosis of lung cancer.* International Journal of Cancer, 2003. 107(6): p. 1047-1052. DOI: 10.1002/ijc.11500

184. C.V. Pagba, et al., *Direct detection of aptamer-thrombin binding via surface-enhanced Raman spectroscopy.* Journal of Biomedical Optics, 2010. 15(4). DOI: 10.1117/1.3465594

185. O.V. Kim, et al., *Fibrin Networks Regulate Protein Transport during Thrombus Development.* Plos Computational Biology, 2013. 9(6). DOI: 10.1371/journal.pcbi.1003095

186. J.W. Weisel, et al., *The shape of thrombomodulin and interactions with thrombin as determined by electron microscopy.* J Biol Chem, 1996. 271(49): p. 31485-90. DOI: 10.1074/jbc.271.49.31485

187. R.A. Engh, et al., *Enzyme flexibility, solvent and 'weak' interactions characterize thrombin-ligand interactions: implications for drug design.* Structure, 1996. 4(11): p. 1353-62. DOI: 10.1016/s0969-2126(96)00142-6

188. S. Papadopoulos, K.D. Jurgens, and G. Gros, *Protein diffusion in living skeletal muscle fibers: Dependence on protein size, fiber type, and contraction.* Biophysical Journal, 2000. 79(4): p. 2084-2094. DOI: 10.1016/S0006-3495(00)76456-3

189. E.C. Le Ru and P.G. Etchegoin, *Single-Molecule Surface-Enhanced Raman Spectroscopy.* Annual Review of Physical Chemistry, Vol 63, 2012. 63: p. 65-87. DOI: 10.1146/annurev-physchem-032511-143757

190. P.C. Weber, et al., *Structural Origins of High-Affinity Biotin Binding to Streptavidin.* Science, 1989. 243(4887): p. 85-88. DOI: 10.1126/science.2911722

191. E. Benson, et al., *Effects of Design Choices on the Stiffness of Wireframe DNA Origami Structures.* ACS Nano, 2018. 12(9): p. 9291-9299. DOI: 10.1021/acsnano.8b04148

192. C.J. Bustamante, et al., *Optical tweezers in single-molecule biophysics.* Nature Reviews Methods Primers, 2021. 1(1). DOI: 10.1038/s43586-021-00021-6

193. Y.J. Pang and R. Gordon, *Optical Trapping of a Single Protein.* Nano Letters, 2012. 12(1): p. 402-406. DOI: 10.1021/nl203719v

194. A.S. Wolberg and R.A. Campbell, *Thrombin generation, fibrin clot formation and hemostasis.* Transfusion and Apheresis Science, 2008. 38(1): p. 15-23. DOI: 10.1016/j.transci.2007.12.005

195. T.L. Mcmeekin, M.L. Groves, and N.J. Hipp, *Refractive Indices of Amino Acids, Proteins, and Related Substances.* Advances in Chemistry, 1964. 44: p. 54-66. DOI: 10.1021/ba-1964-0044.ch004

196. Y.H. Tan, et al., *A Nanoengineering Approach for Investigation and Regulation of Protein Immobilization.* ACS Nano, 2008. 2(11): p. 2374-2384. DOI: 10.1021/nn800508f

197. G. Vidarsson, G. Dekkers, and T. Rispens, *IgG subclasses and allotypes: from structure to effector functions.* Frontiers in Immunology, 2014. 5. DOI: 10.3389/fimmu.2014.00520

198. L. Nguyen, et al., *DNA-Origami-Templated Silica Growth by Sol-Gel Chemistry.* Angewandte Chemie-International Edition, 2019. 58(3): p. 912-916. DOI: 10.1002/anie.201811323

199. Y.X. Shang, et al., *Site-Specific Synthesis of Silica Nanostructures on DNA Origami Templates.* Advanced Materials, 2020. 32(21). DOI: 10.1002/adma.202000294

200. L.M. Wassermann, et al., *Full Site-specific Addressability in DNA Origami-templated Silica Nanostructures.* Advanced Materials, 2023. 35(23). DOI: 10.1002/adma.202212024

201. M. Tortello, et al., *Chemical-Vapor-Deposited Graphene as a Thermally Conducting Coating.* ACS Applied Nano Materials, 2019. 2(5): p. 2621-2633. DOI: 10.1021/acsanm.8b02243

202. J. Gargiulo, et al., *Understanding and Reducing Photothermal Forces for the Fabrication of Au Nanoparticle Dimers by Optical Printing.* Nano Letters, 2017. 17(9): p. 5747-5755. DOI: 10.1021/acs.nanolett.7b02713

203. A. Jakab, et al., *Highly Sensitive Plasmonic Silver Nanorods.* ACS Nano, 2011. 5(9): p. 6880-6885. DOI: 10.1021/nn200877b

204. H.Y. Xu, et al., *Synthesis of high-purity silver nanorods with tunable plasmonic properties and sensor behavior.* Photonics Research, 2017. 5(1): p. 27-32. DOI: 10.1364/Prj.5.000027

205. C.R. Rekha, V.U. Nayar, and K.G. Gopchandran, *Synthesis of highly stable silver nanorods and their application as SERS substrates.* Journal of Science-Advanced Materials and Devices, 2018. 3(2): p. 196-205. DOI: 10.1016/j.jsamd.2018.03.003

206. E.D. Palik, *Handbook of optical constants of solids*. Academic Press handbook series. 1985, Orlando: Academic Press

207. B. Molleman and T. Hiemstra, *Surface Structure of Silver Nanoparticles as a Model for Understanding the Oxidative Dissolution of Silver Ions.* Langmuir, 2015. 31(49): p. 13361-13372. DOI: 10.1021/acs.langmuir.5b03686

208. S.N. Luoma, Y.B. Ho, and G.W. Bryan, *Fate, Bioavailability and Toxicity of Silver in Estuarine Environments.* Marine Pollution Bulletin, 1995. 31(1-3): p. 44-54. DOI: 10.1016/0025-326x(95)00081-W

209. P.P. Dong, et al., *Ultrathin Gold-Shell Coated Silver Nanoparticles onto a Glass Platform for Improvement of Plasmonic Sensors.* ACS Applied Materials & Interfaces, 2013. 5(7): p. 2392-2399. DOI: 10.1021/am4004254

210. Y.J. Jiang, S. Pillai, and M.A. Green, *Realistic Silver Optical Constants for Plasmonics.* Scientific Reports, 2016. 6. DOI: 10.1038/srep30605

211. M. Liu and P. Guyot-Sionnest, *Preparation and optical properties of silver chalcogenide coated gold nanorods.* Journal of Materials Chemistry, 2006. 16(40): p. 3942-3945. DOI: 10.1039/B607106F

212. M. Morshed, L. Xu, and H.T. Hattori, *Dual-polarization star-gap nano-antenna.* Journal of the optical Society of America B, 2019. 36(10): p. 2913-2919. DOI: 10.1364/JOSAB.36.002913

213. D.L. Mack, et al., *Decoupling absorption and emission processes in super-resolution localization of emitters in a plasmonic hotspot.* Nature Communications, 2017. 8. DOI: 10.1038/ncomms14513

214. F. Schuknecht, et al., *Single-Step Plasmonic Dimer Printing by Gold Nanorod Splitting with Light.* Nano Letters, 2023. DOI: 10.1021/acs.nanolett.2c04954

215. W.Q. Zhu and K.B. Crozier, *Quantum mechanical limit to plasmonic enhancement as observed by surface-enhanced Raman scattering.* Nature Communications, 2014. 5. DOI: 10.1038/ncomms6228

216. J. Gargiulo, et al., *Connecting Metallic Nanoparticles by Optical Printing.* Nano Letters, 2016. 16(2): p. 1224-1229. DOI: 10.1021/acs.nanolett.5b04542

217. J.S. Donner, et al., *Plasmon-Assisted Optofluidics.* ACS Nano, 2011. 5(7): p. 5457-5462. DOI: 10.1021/nn200590u

218. A.S. Urban, et al., *Shrink-to-Fit Plasmonic Nanostructures.* Advanced Optical Materials, 2013. 1(2): p. 123-127. DOI: 10.1002/adom.201200031

219. J. Gargiulo, et al., *Accuracy and Mechanistic Details of Optical Printing of Single Au and Ag Nanoparticles (vol 11, pg 9678, 2017).* ACS Nano, 2018. 12(2): p. 2080-2080. DOI: 10.1021/acsnano.8b00573

220. G. Baffou, C. Girard, and R. Quidant, *Mapping Heat Origin in Plasmonic Structures.* Physical Review Letters, 2010. 104(13). DOI: 10.1103/PhysRevLett.104.136805

221. H. Petrova, et al., *On the temperature stability of gold nanorods: comparison between thermal and ultrafast laser-induced heating.* Physical Chemistry Chemical Physics, 2006. 8(7): p. 814-821. DOI: 10.1039/b514644e

222. J.A.F. Plateau, *Experimental and Theoretical Statics of Liqiuds Subject to Molecular Forces only.* Paris: Gauthuer-Villars, 1873

223. L. Rayleigh, *On The Instability Of Jets.* Proceedings of the London Mathematical Society, 1878. s1-10(1): p. 4-13. DOI: 10.1112/plms/s1-10.1.4

224. F.A. Nichols, *On the spheroidization of rod-shaped particles of finite length.* Journal of Materials Science, 1976. 11(6): p. 1077-1082. DOI: 10.1007/bf02396641

225. J. Schust, et al., *Spatially Resolved Nonlinear Plasmonics.* Nano Letters, 2023. 23(11): p. 5141-5147. DOI: 10.1021/acs.nanolett.3c01070

226. S.H. Behrens and D.G. Grier, *The charge of glass and silica surfaces.* Journal of Chemical Physics, 2001. 115(14): p. 6716-6721. DOI: 10.1063/1.1404988

227. J. Sonnefeld, *Determination of surface charge density parameters of silicon nitride.* Colloids and Surfaces a-Physicochemical and Engineering Aspects, 1996. 108(1): p. 27-31. DOI: 10.1016/0927-7757(95)03356-4

228. R. Esteban, et al., *A classical treatment of optical tunneling in plasmonic gaps: extending the quantum corrected model to practical situations.* Faraday Discussions, 2015. 178(0): p. 151-183. DOI: 10.1039/C4FD00196F

229. K.J. Savage, et al., *Revealing the quantum regime in tunnelling plasmonics.* Nature, 2012. 491(7425): p. 574-577. DOI: 10.1038/nature11653

230. J.A. Scholl, et al., *Observation of Quantum Tunneling between Two Plasmonic Nanoparticles.* Nano Letters, 2013. 13(2): p. 564-569. DOI: 10.1021/nl304078v

231. F. Liebig, et al., *Undulated Gold Nanoplatelet Superstructures: In Situ Growth of Hemispherical Gold Nanoparticles onto the Surface of Gold Nanotriangles.* Langmuir, 2018. 34(15): p. 4584-4594. DOI: 10.1021/acs.langmuir.7b02898

232. S. Juergensen, P. Kusch, and S. Reich, *Resonant Raman Scattering of 4-Nitrothiophenol.* Physica Status Solidi B-Basic Solid State Physics, 2020. 257(12). DOI: 10.1002/pssb.202000295

233. C.-H. Lai, et al., *Near infrared surface-enhanced Raman scattering based on star-shaped gold/silver nanoparticles and hyperbolic metamaterial.* Scientific Reports, 2017. 7(1): p. 5446. DOI: 10.1038/s41598-017-05939-0

234. T. You, et al., *Direct observation of p,p'-dimercaptoazobenzene produced from p-aminothiophenol and p-nitrothiophenol on Cu2O nanoparticles by surface-enhanced Raman spectroscopy.* Journal of Raman Spectroscopy, 2014. 45(1): p. 7-14. DOI: 10.1002/jrs.4411

235. L. Qiu, et al., *Kinetic and Mechanistic Investigation of the Photocatalyzed Surface Reduction of 4-Nitrothiophenol Observed on a Silver Plasmonic Film via Surface-Enhanced Raman Scattering.* ACS Applied Materials & Interfaces, 2020. 12(18): p. 21133-21142. DOI: 10.1021/acsami.0c05977

236. A.L. Dendramis, E.W. Schwinn, and R.P. Sperline, *A Surface-Enhanced Raman-Scattering Study of CTAB Adsorption on Copper.* Surface Science, 1983. 134(3): p. 675-688. DOI: 10.1016/0039-6028(83)90065-1

237. J. Goworek, et al., *Thermal Degradation of CTAB in as-Synthesized Mcm-41.* Journal of Thermal Analysis and Calorimetry, 2009. 96(2): p. 375-382. DOI: 10.1007/s10973-008-9055-6

238. M.J.A. Hore, et al., *Probing the Structure, Composition, and Spatial Distribution of Ligands on Gold Nanorods.* Nano Letters, 2015. 15(9): p. 5730-5738. DOI: 10.1021/acs.nanolett.5b03088

239. V. Agmo Hernández, *An overview of surface forces and the DLVO theory.* ChemTexts, 2023. 9(4): p. 10. DOI: 10.1007/s40828-023-00182-9

240. V.V. Klimov and A. Lambrecht, *Van der Waals Forces Between Plasmonic Nanoparticles.* Plasmonics, 2009. 4(1): p. 31-36. DOI: 10.1007/s11468-008-9074-y

241. R. Zhao, et al., *Description of van der Waals Interactions Using Transformation Optics.* Physical Review Letters, 2013. 111(3): p. 033602. DOI: 10.1103/PhysRevLett.111.033602

242. Y. Luo, R. Zhao, and J.B. Pendry, *van der Waals interactions at the nanoscale: the effects of nonlocality.* Proceedings of the National Academy of Sciences of the United States of America, 2014. 111(52): p. 18422-7. DOI: 10.1073/pnas.1420551111

243. S.S. Batsanov, *Van der Waals Radii of Elements.* Inorganic Materials, 2001. 37(9): p. 871-885. DOI: 10.1023/A:1011625728803

244. Z. Yan, S.K. Gray, and N.F. Scherer, *Potential energy surfaces and reaction pathways for light-mediated self-organization of metal nanoparticle clusters.* Nature Communications, 2014. 5(1): p. 3751. DOI: 10.1038/ncomms4751

245. K.A. Forbes, D.S. Bradshaw, and D.L. Andrews, *Optical binding of nanoparticles.* Nanophotonics, 2020. 9(1): p. 1-17. DOI: 10.1515/nanoph-2019-0361

246. C.-H. Huang, et al., *The primeval optical evolving matter by optical binding inside and outside the photon beam.* Nature Communications, 2022. 13(1): p. 5325. DOI: 10.1038/s41467-022-33070-w

247. H. Xu and M. Käll, *Surface-plasmon-enhanced optical forces in silver nanoaggregates.* Physical Review Letters, 2002. 89(24): p. 246802. DOI: 10.1103/PhysRevLett.89.246802

248. F. Svedberg, et al., *Creating hot nanoparticle pairs for surface-enhanced Raman spectroscopy through optical manipulation.* Nano Letters, 2006. 6(12): p. 2639-2641. DOI: 10.1021/nl062101m

249. S.J. Ling, J. Sanny, and W. Moebs, *University Physics Volume 3*. 2016, Houston, Texas: OpenStax

250. F. Musumeci and G.H. Pollack, *Influence of water on the work function of certain metals.* Chemical Physics Letters, 2012. 536: p. 65-67. DOI: 10.1016/j.cplett.2012.03.094

251. Y. Zhang, et al., *Coherent anti-Stokes Raman scattering with single-molecule sensitivity using a plasmonic Fano resonance.* Nature Communications, 2014. 5. DOI: 10.1038/ncomms5424

Acknowledgments

My first thanks go to PD Dr. Theo Lohmüller, for great ideas and supervision, as well as guidance and advice, not limited to science. You have always believed in our work and the ability to make it count. Vast parts of my PhD were characterised by a great collaborative spirit in your bio-photonics group. I will greatly miss our discussions, academic and otherwise!

Next, I must thank Prof. Jochen Feldmann, for funding, challenging scientific discussions, interesting feedback, and access to the facilities of PHOG. Without you, the chair could not exist in its formidable form.

I would also like to thank further research collaborators in the order of appearance: Dr. Christoph Maier (for help during my master's Thesis, and beyond), Dr. Veronika Hintermayr, Dr. Ana Huergo, Dr. Markus Döblinger (for great HR-TEM images), Dr. Karol Kolataj, Prof. Tim Liedl, Jonathan Lang, Jinhua Zhang, Michael Steinberger, Ludwig Habermann, Camila Otero, Alexander Pattis, Paul Vosshage, and Jonathan Heine. You were more than only fruitful to work with, and I wish you all the very best of luck in future.

Thanks also goes Gerlinde Adam, as well as Stefan Niedermeier and Talee Barghouti for administrative and technical support, as well as good conversation. Here I should also mention organizers and members the SFB 1032 as well as CENS in general, for facilitating meetings, discussions, and collaborations.

Additionally, there are other (former) members of the chair, with whom I've had fun and interesting times, including, but not limited to Dr. Jacek Stolarczyk (knower of literature), Dr. Aurora Manzi (my favorite tutor), Dr. Enping Yao, Dr. Sebastian Rieger, Dr. Stefanie Pritzl, Dr. Nicola Kerschbaumer, Mariam Kurashvili, Philipp Bootz, Theresa Kehler, Tim Fürmann, Isabella Tepfenhart, Lucas Prins (many technical discussions), Gerard Faustino, and many more. Further, there is Dr. Ludwig Hüttenhofer, also for help with the WITec microscope.

Then I have to thank other friends of mine also in the order of appearance, but most definitely not limited to: Fabian Gieseck and Max Luckmann (for friendship since childhood, and different insights), as well as (Johann) Moritz Weck (for a lot since we met on the stairs to our first lecture), as well as Peter Kulosik, Dr. Max Rinnagel and Mathias Lipka (study, cycling and beyond).

Additionally, I would like to express my gratitude to my school physics teachers Dr. Angelika Küber and Dr. Gesa Köhl.

Finally, I thank all members of my family, Schuknecht, Patel and otherwise. In particular, my parents Jyoti Patel and Dr. Ludger Schuknecht. You have always been there for me.